MIMICAD TECHNICAL REPORT NO. 10

Modeling and Sensitivity Analysis of Parasitic Coupling in Microstrip Circuits

by

Alan Prothe and K.C. Gupta

Department of Electrical and Computer Engineering
University of Colorado
Boulder, Colorado 80309-0425

Work described in this report is based on a Master of Science thesis submitted by A. Prothe and has been supported by the Darpa MMIC Phase III Program and the MIMICAD Center.

August 1991

Abstract

This report presents a method for modeling couplings between microstrip components and evaluating sensitivities of MMIC performance to various layout dependent parasitic couplings. Planar analysis of microstrip circuits is used to obtain a network characterization of each component without coupling. This is then modified by means of the multiport network method to account for parasitic couplings between various microstrip components. The adjoint network method is used as a means of evaluating circuit sensitivities. Methodology for implementing the proposed methods has been introduced, and the techniques are illustrated by considering examples of practical MMIC layouts.

ACKNOWLEDGEMENTS-

Work reported here has been supported by the DARPA MMIC Phase 3 Program under Contract N00019-89-C-0151, as a part of the MIMICAD Center project on Modeling and CAD Methodology for MMIC Layout Optimization.

The MMIC layouts used for implementation of the methods developed in this work have been made available by Dr. Inder Bahl and *ITT GaAs Tech. Center*, Roanoke, VA. Their cooperation in this matter was essential to our research. Interaction with M.E. Goldfarb of Raytheon Company is also gratefully acknowledged.

CONTENTS

TABLES

TABLE

FIGURES

FIGURE

CHAPTER 1

INTRODUCTION

The prevailing trends in modern communications have led to further development of devices designed to operate at microwave and millimeter wave frequencies. Advances in the fabrication of monolithic microwave integrated circuits (MMIC's) have accompanied this progression to higher operating frequencies. And MMIC technology has placed greater demands on the computer aided design (CAD) tools used in the development of these devices. At these higher operating frequencies simple models may fail to adequately describe device behavior, thus more detailed analysis is often needed to provide accurate modeling of microwave components. Moreover, fabrication costs and time constraints associated with monolithic circuit design have placed a premium on highly accurate CAD analysis tools. Whereas CAD has traditionally been performed using circuit-theory based analysis, the push in recent years is toward the use of electromagnetic models in microwave circuit CAD. Since treating a structure in terms of voltages and currents is less difficult and computationally faster than field analysis it is not likely that electromagnetic models will replace circuit-theory based CAD. Instead, electromagnetic analysis should stand next to traditional analysis stepping in only as needed. The most complete electromagnetic models have been classified as 'full-wave', or 'three-dimensional'. These methods perform the field analysis for an arbitrary three-dimensional structure. Moment method solutions are an example from this class. In this

report a less rigorous model which may be called 'two-dimensional' is applied to the analysis of microstrip planar components. Planar analysis is based on a parallel-plate waveguide model, and analysis of this model assumes no field variation along the height of the substrate, hence planar analysis cannot yield results which are as accurate as full-wave methods. Yet the two-dimensional field solutions outrank quasi-static analysis techniques because higher-order modes in two transverse dimensions and dispersion effects are included. Planar analysis may therefore be considered an intermediate level analysis.

Because microstrip is an open structure, energy may be carried away from microstrip components through radiation. It is also possible for external fields to couple to other components in a MMIC layout. Most often such coupling is undesireable and is therefore appropriately called 'parasitic' coupling. If devices are tightly spaced to conserve MMIC real estate, these couplings may potentially become very significant, and one of the primary limitations of present microwave CAD is the inability to model spurious radiation and parasitic coupling in a MMIC layout.

Different methods may be proposed to address these needs. Radiation loss in microstrip discontinuities has been calculated by finding the Poynting vector produced by currents on the microstrip [1] , [2], [3]. It is also possible to include radiation loss and account for parasitic couplings by using full-wave analysis techniques [4]. But full-wave analysis methods are computationally intensive so their use is accompanied by this associated cost. The Multiport Network Model was developed to account for junction and edge effects [5] in microstrip patch antennas and, soon after, for mutual coupling between patches [6]. The Multiport Network Model has recently been extended by

means of the Planar Lumped Model to account for spurious couplings among coupled-microstrip line discontinuities [7]. So we find that methods exist for obtaining a quantitative measure of the parasitic coupling between microstrip elements. Yet these methods are inappropriate for analyzing large circuits, so it is necessary for the designer to know what portions of a MMIC require a more accurate analysis which includes the effects of coupling. Thus it is important to also have a quantitative estimate of how important couplings are to the overall circuit performance. Sensitivity analysis can be a help to the designer in making this determination, and, in this way sensitivity analysis provides information other analysis techniques do not. Rather than seeking to answer, ' How much? ', sensitivity analysis for parasitic coupling helps answer the question, ' How significant is this coupling? '. Yet, to date, there has been little work reported which provides a measure of circuit sensitivity to parasitic couplings.

In this report the Multiport Network Model is discussed as a means for incorporating parasitic couplings in microstrip circuit analysis. The methods described are then extended to yield circuit sensitivity analysis for changes in parasitic coupling. The Multiport Network Model is well suited to sensitivity analysis, and although the models used are approximate and cannot compete with full-wave analysis techniques in terms of accuracy, planar analysis methods play their own role as one of the tools a designer may choose. Indeed, for the purpose of identifying 'hot spots' in a MMIC layout for which parasitic couplings are most significant, planar analysis and the Multiport Network Model may be ideal.

The format of this report is as follows. Planar analysis of microstrip

components is outlined first, and a planar model for viahole grounds introduced. Chapter 3 includes a discussion of the Multiport Network Model and how it is used to incorporate parasitic coupling effects into circuit analysis. The following chapter derives the sensitivity equation and reports sensitivities for selected sub-circuits. Chapter 5 is an extension of the sub-circuit sensitivity to determine sensitivities of the external-port parameters of a complete MMIC layout, a task illustrated by examples. The final chapter includes the closing remarks.

CHAPTER 2

PLANAR ANALYSIS OF MICROSTRIP CIRCUITS

Planar modeling of microstrip structures relies on the premise that the height of the substrate is electrically thin and consequently underneath the strip, there is no variation of the fields along the substrate height. In this approach, the physical microstrip structure is replaced by a planar waveguide model. This chapter begins with a discussion of the planar waveguide model for a uniform microstrip line. Next, methods are described for applying the planar waveguide model to various discontinuities, and, in turn, to a more complete microstrip circuit structure. Finally, planar analysis is applied to the modeling of microstrip viahole grounds.

2.1 Planar Waveguide Model for Microstrip Lines

The planar waveguide model for microstrip line is shown in Figure 2.1. The structure consists of two parallel conductors bounded on either side by magnetic walls. The width of the waveguide, called the effective width, w_{eff}, is larger than the physical width of the microstrip line in order to account for the fringing fields of the microstrip. This equivalent waveguide is filled with an effective dielectric constant, ϵ_{reff}, which is smaller than ϵ_r of the substrate since the fields extend outside the dielectric layer. The height is not changed in this model, but w_{eff} and ϵ_{reff} are selected to account for the fringing fields such that $Z_{TEM}^{WAVEGUIDE} = Z_0^{MICROSTRIP}$ and $\lambda_o^{WAVEGUIDE} = \lambda_g^{MICROSTRIP}$. Here, Z_{TEM} is given by the parallel plate

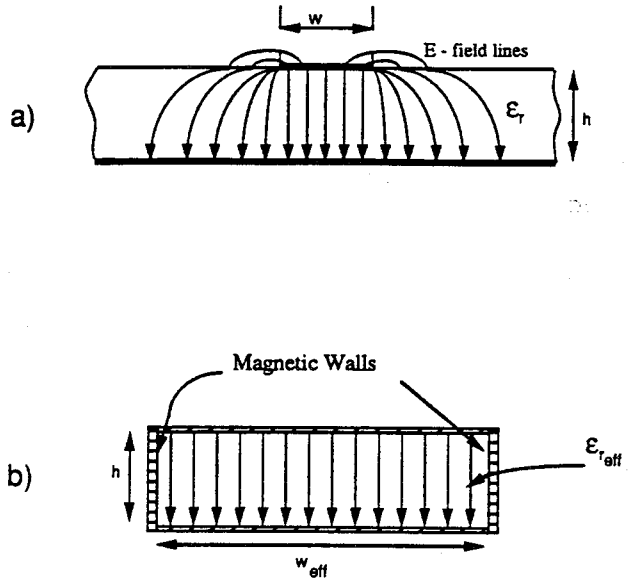

Figure 2.1: Planar Wavguide Model for Microstrip Line
(a) Microstrip Line (b) Equivalent Planar Waveguide

waveguide formula $Z_{TEM} = \eta_o h/\sqrt{\epsilon_{reff}}\,\omega_{eff}$, and $\lambda_g = c/f\sqrt{\epsilon_{reff}}$. Values of w_{eff} and ϵ_{reff} can be obtained from a quasi-static analysis of the microstrip line [9], however, because the fields are more closely confined to the microstrip at higher frequencies, the frequency dependent values $Z_o(f)$ and $\epsilon_{re}(f)$ are needed to accurately model the line. Beginning with analytical equations for $Z_o(f)$ and $\epsilon_{re}(f)$ in the special case of homogeneous media and an infinitely thin conducting strip, Hammerstad and Jensen [10] have extended their work and that of others to account for inhomogeneous media ($\epsilon_r > 1$) [11], finite conductor thickness ($t \neq 0$), and frequency dispersion [12] to develop accurate expressions for the dynamic characteristic impedance and effective dielectric constant for microstrip lines. Their equations are well-suited to computer

aided design and remain accurate for nearly all practical line widths and for any substrate commonly in use. From such expressions for $Z_o(f)$ and $\epsilon_{re}(f)$ the frequency dependent effective width is obtained directly as

$$w_e(f) = \frac{\eta_o h}{Z_o \sqrt{\epsilon_{re}(f)}} \tag{2.1}$$

where η_o is the impedance of free space and h is the substrate height. To account for losses, the planar waveguide model uses an effective loss tangent which may be expressed as [14]

$$tan\delta_e = tan\delta + \frac{1}{h\sqrt{\mu\pi f\sigma}} \tag{2.2}$$

By including the conductor loss in the effective loss tangent the planar waveguide can be modeled by perfectly conducting upper and lower plates filled with a complex dielectric constant given by

$$\epsilon_c = \epsilon_o \epsilon_{re}(1 - jtan\delta_e) \tag{2.3}$$

2.2 Planar Waveguide Model for Circuit Structures

The previous section outlined the development of the planar waveguide model for a uniform microstrip line. But the usefulness of the planar model is not to be found in predicting the transmission properties of a line — indeed it was developed from knowing these apriori. Rather it is because the planar waveguide seeks to model not only the transmission properties, but the field configuration that makes it applicable to other planar components. Kompa and Mehran [15] have shown that the planar model characterizes the transmission properties of the fundamental mode, but also accurately predicts the cutoff frequencies of the next two higher order modes on the microstrip line. From this basis, a natural extension of the model is the analysis of microstrip line discontinuities, and it has been widely used for this application

([16] [17] [18]). Several discontinuities for which the planar model has been used are shown in Figure 2.2. The planar model may be further extended to other microstrip components provided the substrate is thin and that a method exists for determining the effective dimensions needed to account for fringing and the effective dielectric constant.

This section discusses a method for analyzing various shapes of planar circuits using a Green's function approach and a procedure, known as segmentation, for extending the analysis to configurations with any number of these components.

2.2.1 Analysis Using the Green's Function Approach. The approach taken for planar analysis is to describe the planar component in terms of voltages and currents at desired external ports. Thus the objective is to obtain a network model for the component which may be described by an impedance matrix. Consider the planar circuit of Figure 2.3. The field within the waveguide is the solution of the Helmholtz equation, $(\nabla^2 + k^2)\mathbf{E} = 0$. Taking the substrate height to be much less than a wavelength, we have $\frac{\partial}{\partial z} = 0$. This, together with the boundary condition at the upper and lower plates gives $E_x = E_y = H_z = 0$. Thus the field component E_z satisfies, for the source-free case,

$$(\nabla_t^2 + k^2)E_z = 0 \tag{2.4}$$

where $k = \omega\sqrt{\mu\epsilon}$ and $\nabla_t^2 = \frac{\partial^2}{\partial x^2} + \frac{\partial^2}{\partial y^2}$. Since $\frac{\partial}{\partial z} = 0$, we may express the voltage on the upper plate (the lower plate acting as reference) as

$$v(x, y) = -hE_z(x, y) \tag{2.5}$$

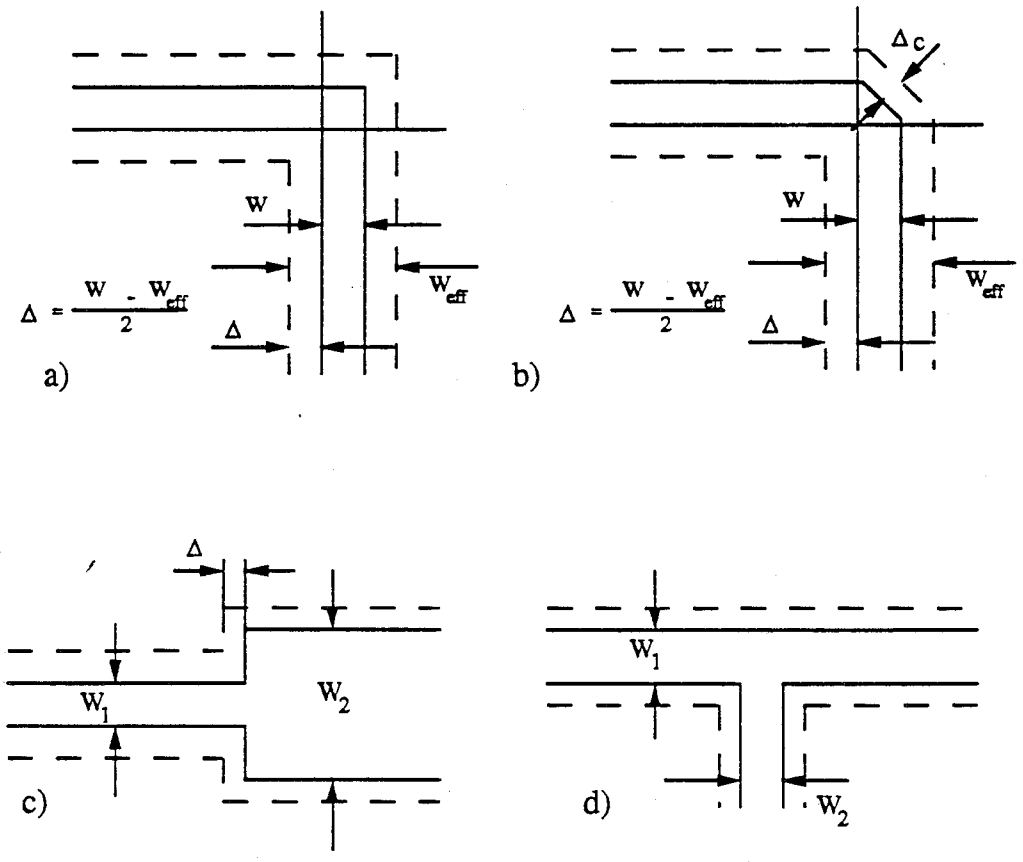

Figure 2.2: Planar Analysis of Microstrip Line Discontinuities; (a) right angled-bend; (b) chamfered right-angled bend; (c) step in width; (d) tee-junction

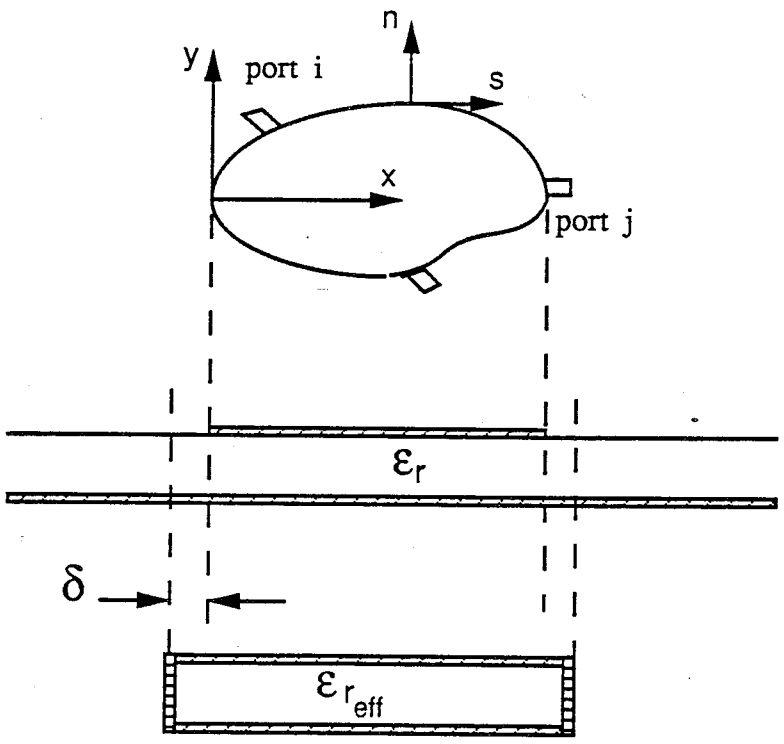

Figure 2.3: Planar Component of Arbitrary Shape

where h is the substrate height. For an impressed source, J_z , the wave equation becomes

$$(\nabla_t^2 + k^2)v(x,y) = -j\omega\mu h J_z. \tag{2.6}$$

Thus if we define an impedance Green's function to give the voltage at a point (x,y) due to a point-source current at (x_o,y_o), the voltage can be obtained by taking into account all such currents, or

$$v(x,y) = \int\int G(x,y \mid x_o,y_o)J_z(x_o,y_o)dx_o dy_o \tag{2.7}$$

where $G(x,y \mid x_o,y_o)$ is the solution to

$$(\nabla_t^2 + k^2)G(x,y \mid x_o,y_o) = -j\omega\mu h\delta(x-x_o)\delta(y-y_o). \tag{2.8}$$

In practice, the source current will often come from an adjacent planar feed (one of the ports), where the current density is not directed along the z direction,

but flows on the upper and lower plates of the feed. Also, there is a gap in the magnetic wall boundary at such ports. To carry out the analysis, these currents are replaced by an equivalent z-directed current source located at the gap in the magnetic wall which is thus closed. This must be done in such a way so as to preserve the field configuration inside the guide. Figure 2.4 illustrates this

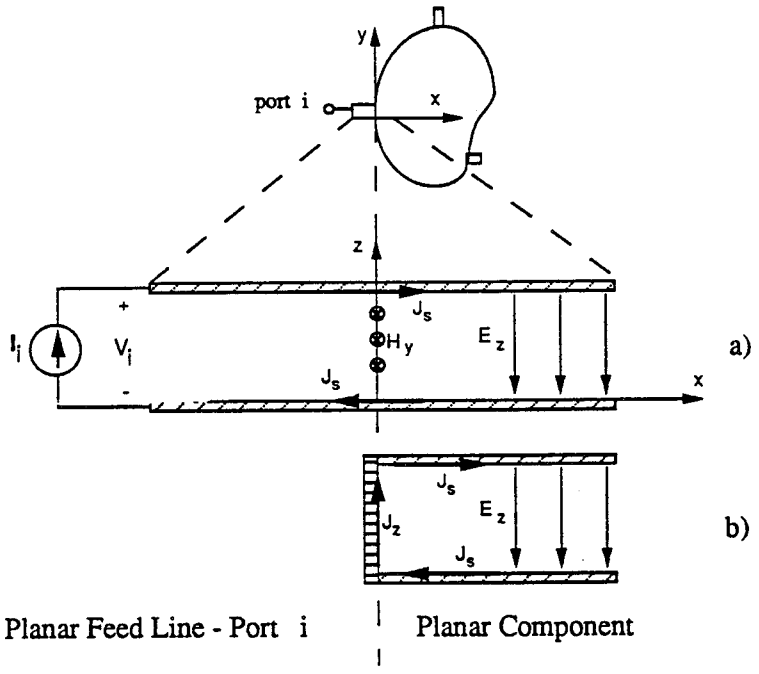

Figure 2.4: Equivalent Source Current for Planar Feed
(a) Planar Feed Currents (b) Equivalent $\hat{z}$-directed Currents

procedure, and for simplicity the port is oriented along the y-axis. Refering first to Figure 2.4(a), we have from Maxwell's Equations

$$\mathbf{H} = \frac{-1}{j\omega\mu}(\nabla \times \mathbf{E}) = (\frac{\partial E_z}{\partial y}\hat{a}_x - \frac{\partial E_z}{\partial x}\hat{a}_y) \tag{2.9}$$

so,

$$H_y = \frac{1}{j\omega\mu}(\frac{\partial E_z}{\partial x}). \tag{2.10}$$

The surface currents crossing the port on the upper and lower surfaces are found to be

$$\mathbf{J_S}^{upper} = -\hat{a}_z \times (\hat{a}_y H_y) = \hat{a}_x H_y \tag{2.11}$$

and

$$\mathbf{J_S}^{lower} = \hat{a}_z \times (\hat{a}_y H_y) = \hat{a}_x H_y \tag{2.12}$$

Looking next to Figure 2.4(b), we require H_y to remain unchanged inside the planar component. This requires an equivalent surface current $\mathbf{J_z}$ located at the magnetic wall boundary, given by

$$\mathbf{J_z} = \hat{a}_x \times (\hat{a}_y H_y) = \hat{a}_z H_y \tag{2.13}$$

Thus we find that the equivalent source, $\mathbf{J_z}$, is equal in magnitude to the current $\mathbf{J_s}$ and is directed such that it completes the current loop of the upper and lower plates. Taking the voltage of a port i to be the average voltage across the width of the port we have

$$v_i = \frac{1}{w_i}\int_{wi} v(s)ds. \tag{2.14}$$

If we further assume that the current in the port j flows uniformly across it's width, we can express the impedance coefficient between the two ports i and j as

$$Z_{ij} = \frac{1}{w_i w_j}\int_{wi}\int_{wj} G(x_i, y_i \mid x_j, y_j)d\bar{r}_i d\bar{r}_j \tag{2.15}$$

where $d\bar{r}_i$ and $d\bar{r}_j$ are the incremental distances over the port widths w_i and w_j respectively. Determining such impedance terms for each port yields the

impedance matrix characterization of the planar component. Evaluation of the Green's function for a given component can be carried out either by the method of images or by expanding a set of orthogonal eigenfunctions. The Green's functions for a number of regular shapes such as rectangles, several triangles, circular disks, and circular rings have been determined [19]. Still, the Green's function approach remains limited to a few basic component shapes.

2.2.2 The Segmentation Method. Although the Green's function approach for characterization of planar components is limited to regular segments for which the Green's functions are known, a method known as segmentation has been developed which extends the class of circuits which may be analyzed to include circuits which are composed of two or more regular segments. The first step is to determine the effective dimensions and dielectric constants for the planar model. Next, the planar model must be divisible into regular segments which are analyzed individually and characterized by their impedance matrix. The segmentation method involves placing a number of ports along the interface between adjacent segments and matching the voltage and currents at these ports. By this procedure it is possible to characterize the two-segment combination. For a multiple-segment circuit, this process can be repeated one segment at a time until the entire circuit has been characterized. This is known as the subnetwork growth method [19]. As an example, consider the chamfered bend of Figure 2.5. The planar circuit is first modeled by the effective configuration of Figure 2.5(b) and then divided as shown in 2.5(c). Let Z_A represent segment A, Z_B segment B, and Z_C segment C. Using the segmentation method to combine Z_A and Z_B will result in another matrix,

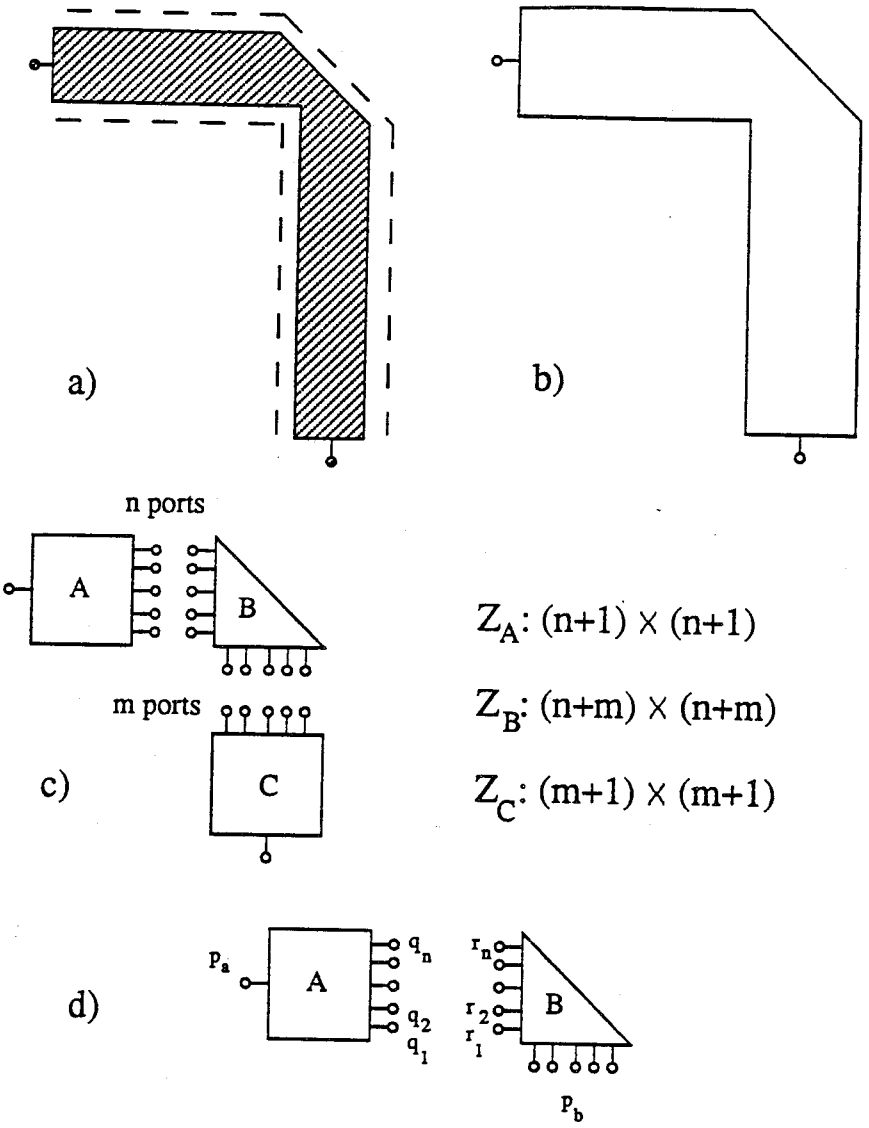

Figure 2.5: Segmentation for Chamfered Bend;
(a) physical structure; (b) planar model; (c) segmented circuit with interconnection ports; (d) numbering for segmentation procedure

Z_{AB} , which has $m+1$ ports characterizing the AB combination. Segmentation is applied again to combine Z_{AB} with Z_C to obtain the desired two-port impedance matrix characterization of the overall network. To make sure the interconnected ports are joined properly each time the segmentation procedure is employed, a consistent book-keeping system is needed. As a starting point, the external ports (which do not appear on the interface of the two segments being combined) are numbered first. These external ports appear in the top portion of their respective matrices. The remaining ports known as interconnection ports are numbered as shown in Figure 2.5(d) with q_1 connected to r_1, and q_2 to r_2, ... etc. This system results in the following matrix relations for the individual segments

$$\begin{bmatrix} V_{p_a} \\ V_q \end{bmatrix} = \begin{bmatrix} Z_{p_a} & Z_{p_aq} \\ Z_{qp_a} & Z_{qq} \end{bmatrix} \begin{bmatrix} I_{p_a} \\ I_q \end{bmatrix} \tag{2.16}$$

and,

$$\begin{bmatrix} V_{p_b} \\ V_r \end{bmatrix} = \begin{bmatrix} Z_{p_b} & Z_{p_br} \\ Z_{rp_b} & Z_{rr} \end{bmatrix} \begin{bmatrix} I_{p_b} \\ I_r \end{bmatrix} \tag{2.17}$$

If these are written together in a single matrix as,

$$\begin{bmatrix} V_p \\ V_q \\ V_r \end{bmatrix} = \begin{bmatrix} Z_{pp} & Z_{pq} & Z_{pr} \\ Z_{qp} & Z_{qq} & 0 \\ Z_{rp} & 0 & Z_{rr} \end{bmatrix} \begin{bmatrix} I_p \\ I_q \\ I_r \end{bmatrix} \tag{2.18}$$

then the resulting expressions can be written more compactly. The conditions imposed by connecting each of the ports q_i to r_i are

$$V_q = V_r \tag{2.19}$$

and,

$$I_q = -I_r \tag{2.20}$$

Matching the currents and voltages in this way corresponds to matching the tangential E and H fields at a discrete number of points along the common boundary of the two segments. If these conditions are substituted back into the matrix equation 2.18 and V_q and I_r eliminated, then we obtain the desired result

$$Z_{AB} = Z_{pp} + (Z_{pq} - Z_{pr})(Z_{qq} + Z_{rr})^{-1}(Z_{rp} - Z_{qp}) \tag{2.21}$$

The segmentation method may also be formulated in terms of admittance matrices or scattering matrices as described in Appendix A. Another method which is complementary to the segmentation procedure is the desegmentation method. Rather than taking the network characterization of two known components and combining them to yield a third network which characterizes the composite shape, desegmentation begins with the network of the composite shape and removes (or de-embeds) another regular component which has been characterized separately. This yields the characterization of the remaining portion of the original component. Some examples of desegmentation are shown in Figure 2.6 [20].

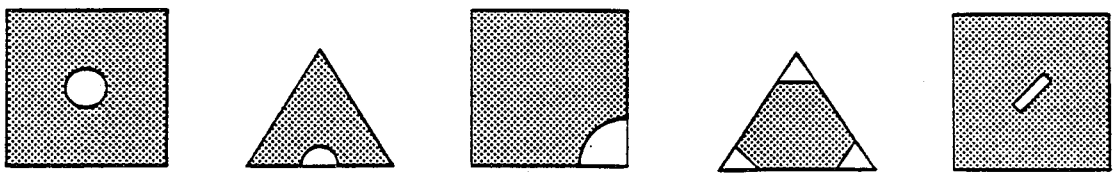

Figure 2.6: Examples of Desegmentation

2.3 Planar Modeling of Microstrip Viahole Grounds

Viaholes are used in Microwave Integrated Circuits to form a connection between different layers in a circuit layout and most commonly from the top surface of a microstrip circuit to the ground plane. The conductor of the upper and lower layers needs to be properly aligned so that a vertical post will connect the two. Most often, a viahole pad is used to ensure that a sound connection will be obtained even if the alignment is imperfect (see Figure 2.7). The viahole may be simply modelled by an inductance whose value is a function of the viahole diameter, the substrate height, and the width of the viahole pad. This section describes an analysis procedure for modeling viaholes by using a planar model for the pad and shorting ports to ground to model the viahole post itself.

2.3.1 Analysis. The structure of Figure 2.8 is described in terms of three planar segments. Two of these represent the microstrip line feeds, and the third segment is the viahole pad. Each is a rectangular planar segment which may be analyzed by the Green's function approach. The viahole post, typically treated as a circular cylinder, is approximated by a polygon. This is done in order to minimize the computational effort. The post could be analyzed as a cylinder by using the desegmentation method, but this procedure requires the characterization of the circular disk in addition to the computations needed for applying desegmentation. The difference in computational efficiency is compounded because the impedance matrix for the rectangular segment is computed using a single-series (SS) form of the Green's function, whereas only a double-series (DS) form is available for the circular disk in the software used in this project. For a rectangular segment the SS form is obtained from the DS

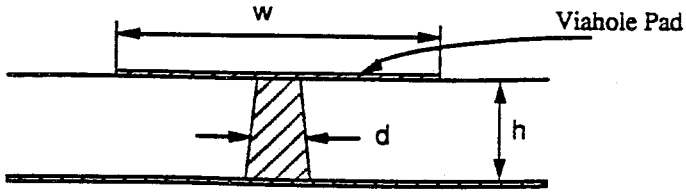

Figure 2.7: Viahole Cross-Section

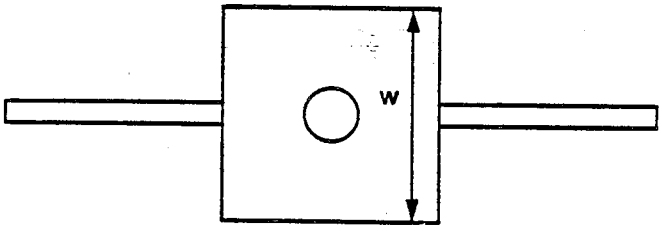

a) physical structure

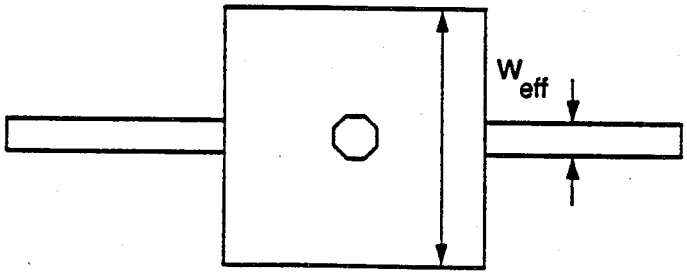

b) planar model

Figure 2.8: Planar Model for Viahole

equation by carrying out one of the summations analytically. The procedure for obtaining the SS expression for the impedance coefficients between two ports has been available only for vertical and horizontal port orientations [21]. Because the polygon has edges which are oriented at various angles an extension of the SS formulation was needed. This derivation has been carried out and SS expressions for the impedance coefficient for two ports with any arbitrary orientation are reported in Appendix B. From these expressions it is possible to obtain an impedance matrix characterization for the viahole structure with ports positioned along the periphery of the viahole. At this point, the interior ports representing the post are shorted to ground, and the resulting network is combined with the feed lines using segmentation thus giving a two-port z-matrix representation for the complete structure. The length of the feed lines was chosen long enough to ensure that the wave propagation along the lines near the external ports could be described by the dominant mode. This impedance matrix is then converted to scattering parameters, the reference planes shifted to the junctions of the viahole pad, and then converted back to an impedance matrix. This impedance matrix characterization is then used to derive the equivalent T-network of Figure 2.9. In this network the series elements $(Z_{11} - Z_{12})$ and $(Z_{22} - Z_{12})$ represent the effects of the pad, while the shunt impedance, Z_{12}, characterizes the viahole post.

2.3.2 Results and Conclusion Analyzing the viahole for different frequencies gives positive reactances for Z_{11} and Z_{12} which vary linearly with frequency as shown in Figure 2.10. Thus the viahole inductance may be obtained directly as

$$L_{via} = \frac{\Im m\{Z_{12}\}}{2\pi f} \tag{2.22}$$

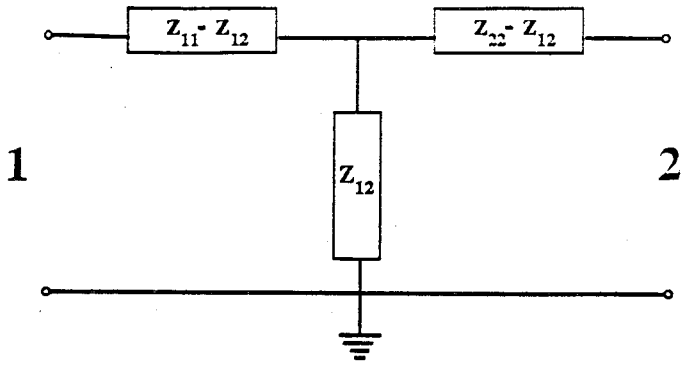

Figure 2.9: Equivalent T-Network Model for Viahole

In a recent publication, Goldfarb and Pucel [22] present a simple equation for calculating viahole inductance as a function of substrate height and post diameter. This expression was shown to give good agreement both with experimental results and numerical simulations. The equation is reproduced here [22],

$$L_{via} = \frac{\mu_0}{2\pi}\left[h \cdot \ln\left(\frac{h+\sqrt{r^2+h^2}}{r}\right) + \frac{3}{2}(r - \sqrt{r^2+h^2})\right] \qquad (2.23)$$

where h is the substrate height and $2r$ is the post diameter. Table 2.1 gives the results of the planar analysis for a fixed substrate height, but different viahole diameters and pad widths. Values for L_{via} as obtained from equation 2.23 are also included for comparison. What is immediately clear is that the viahole inductance obtained by planar analysis is quite dependent upon the effective width of the via pad. By contrast, Goldfarb and Pucel report that the dependence of L_{via} on the physical width of the pad is small, giving less than four percent variation in L_{via} for a wide variation in the width to height ratio. This discrepancy can be attributed to difficulties in finding the effective width of the pad. The effective width was chosen by treating the pad as a microstrip line, but the presence of the post disturbs the fields beneath the pad so that

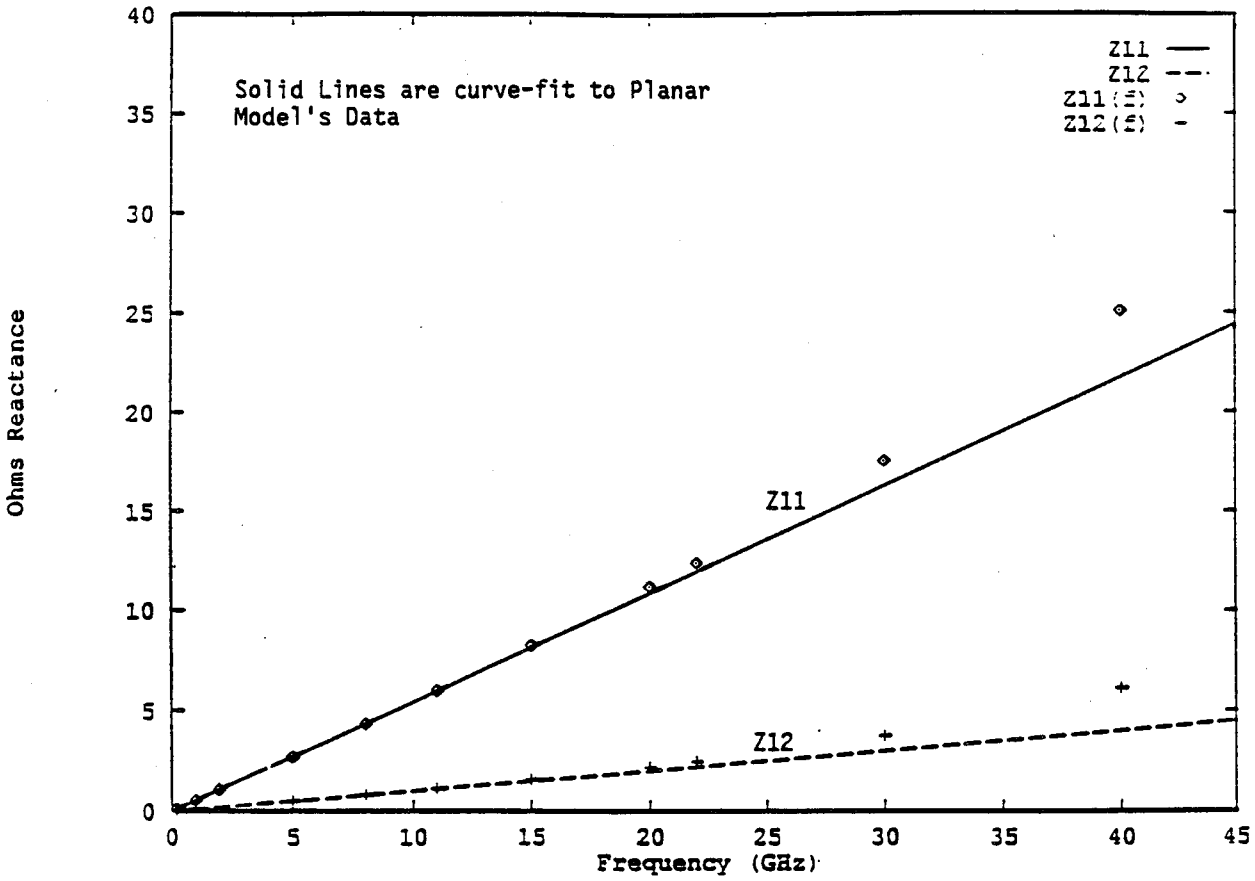

Figure 2.10: Frequency Dependence of Z_{11} and Z_{12}

the effective width, as chosen, may not accurately model the field configuration. In particular, for large post diameters, the fringing fields may extend further beyond the edge of the pad than predicted when treating the pad as a uniform line. This places limitations on the use of the planar model for analyzing this type of structure unless a method for obtaining the proper effective dimensions and dielectric constant is found. In certain cases, however, the planar waveguide model as implemented may yield acceptable results. Finch and Alexopoulos [23] have used the planar waveguide model to analyze shunt posts in microstrip lines, and so doing, they have been able to design a bandpass filter consisting of four shunt posts in a microstrip line and predict it's measured characteristic with reasonable accuracy. From the limited data of Table 2.1, it appears that the planar model as implemented gives realistic inductance values when the viahole post diameter is close to one third of the pad width, which is not uncommon in practice.

Table 2.1: Viahole Inductance for Various d/h and d/w_{eff} Values

Diameter	W:	100	200	220	300	400	Goldfarb
in (micron)	Weff:	306.6	428.7	451.9	542.8	652.9	& Pucel
	Ereff:	8.34	9.06	9.17	9.55	9.92	Lvia
20		32.986	42.919	45.093	55.337	74.122	32.815
40		18.695	26.278	27.831	34.693	46.085	21.655
60		11.209	17.419	18.656	23.980	32.264	16.057
80		6.671	11.785	12.805	17.138	23.649	12.634
100			7.949	8.795	12.381	17.664	10.332
120			5.271	5.962	8.930	13.298	8.690
140			3.399	3.951	6.382	10.011	7.470

Inductance Values (pH) for $\varepsilon_r = 12.9$, and substrate height equal to 100 micron (the data for Planar Model was obtained at a frequency of 20 GHz.)

CHAPTER 3

PARASITIC COUPLING EFFECTS IN MICROSTRIP CIRCUITS

The planar model summarized in Chapter 2 has been used to describe the fields beneath a planar component and account for fringing field effects by an extension of the side walls. Because the equivalent waveguide in this model is enclosed by the magnetic walls, spurious external fields which extend outside the model are not accounted for. To incorporate effects such as radiation loss and couplings between planar components modeling of these external fields is needed. In this chapter a method for incorporating external effects into the planar model is summarized, and a network model for external fields based on equivalent magnetic current elements at the edges of the planar model is discussed. Some examples applying this technique are included, and finally a procedure for implementation for the case of large circuits is introduced.

3.1 Multiport Network Model

For the planar model discussed thus far, the ports which have been specified for each planar segment have been positioned to act either as external ports, where the terminal characteristics are desired, or interconnection ports serving to connect adjacent segments. A technique known as the Multiport Network Model (MNM), first developed to model edge fields and radiation loss in microstrip antennas [5], introduces additional ports along the periphery of the planar circuit. The external fields are accounted for by attaching a

multiport network to these added ports. If we consider the case of the right-angle bend of Figure 3.1, radiation loss may be represented by a radiation conductance network attached to each of these ports, as shown. To handle the task of representing coupling between two discontinuities as in Figure 3.2, a similar approach is taken. Ports are again added along the edges of each

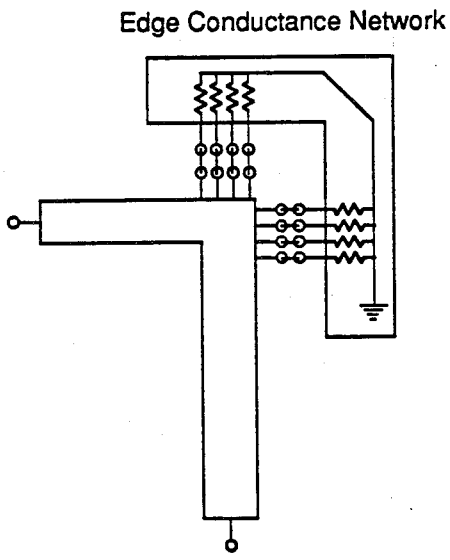

Figure 3.1: Edge Conductance Network for Radiation Loss

structure, and a multiport network attached to these ports to account for the interaction between the two structures. If the first network is used to characterize the radiation loss, the edge conductances, G_{r_n}, chosen must satisfy

$$P_{rad} = \frac{1}{2}\sum_n |V_n|^2 G_{r_n} \tag{3.1}$$

where P_{rad} is the total radiated power, and V_n the voltage at each port. For the second example, the elements in the network become complex admittances which represent the current induced at one port per unit voltage appearing at another port location. Thus we note that the Multiport Network Method

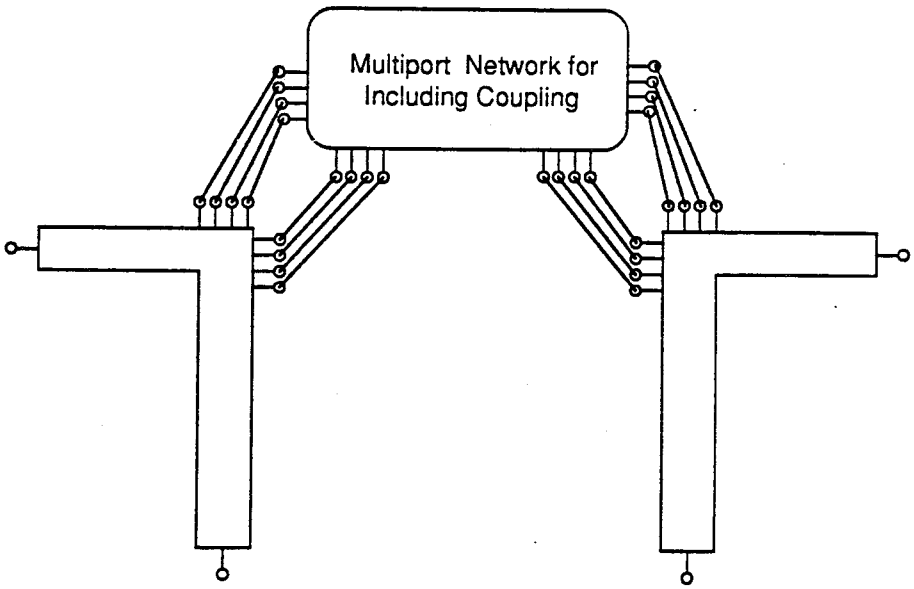

Figure 3.2: Multiport Network for Coupling Effects

is a possible way to mod. external field effects. For implementation of this concept, we need to determine the appropriate multiport network, for it must correctly model the external fields. This is the topic of the next section.

3.2 Modeling Field Effects Exterior to Planar Model

In the MNM approach, external fields are evaluated by means of equivalent magnetic current sources placed along the edges of the planar component. From such sources the fields in the upper half space may be evaluated and the elements of the desired multiport network determined.

3.2.1 External Fields Found From Equivalent Magnetic Current Sources. Magnetic current and charge density are fictitious quantities, whose introduction into Maxwell's equations results in completely dual properties with the electric current and electric charge density. In some sense their inclusion is nothing more than a mathematical convenience, yet in certain

applications magnetic sources have a practical advantage over their physical counterpart. Consider the microstrip line of Figure 3.3(a). Rather than approaching the task of determining the fields in the upper half space in terms

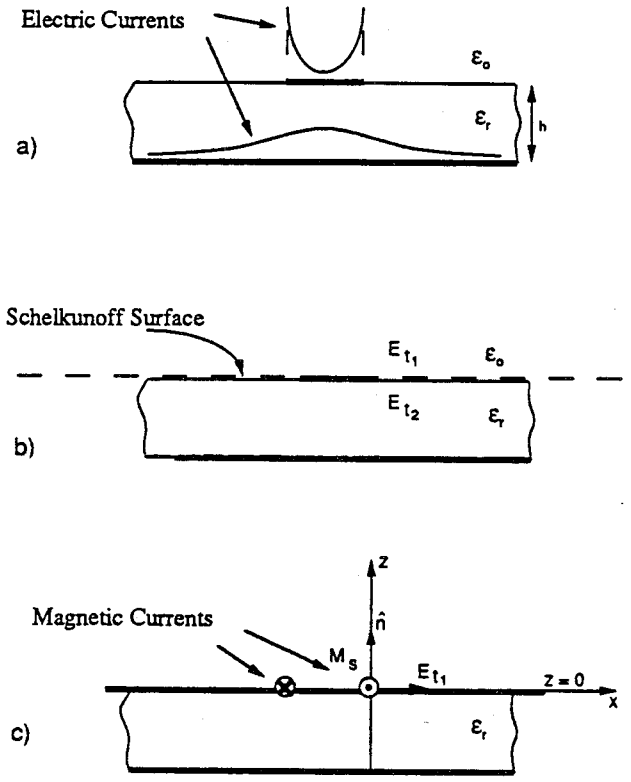

Figure 3.3: Modeling Fields by Equivalent Magnetic Current Sources; (a) Microstrip Line with Electric Current Shown; (b) Application of Equivalence Principle; (c) Microstrip Line with Equivalent Magnetic Current

of the electric currents existing on the microstrip line and ground plane, the problem will be posed in terms of equivalent magnetic currents. According to Schelkunoff's equivalence theorem, we imagine a surface existing along the air-dielectric interface which extends laterally outward to infinity (see Fig. 3.3(b)). The half space above this surface is both source-free and homogeneous, and the

fields in this region may be completely described by equivalent sources existing on this surface. By choosing a perfectly conducting surface, only magnetic current sources are needed. The magnetic surface current at an interface is obtained from,

$$\mathbf{M}_s = -\mathbf{n} \times (\mathbf{E}_{t_1} - \mathbf{E}_{t_2}) \tag{3.2}$$

which for $\mathbf{E}_{t_2} = 0$, is

$$\mathbf{M}_s = -\mathbf{n} \times \mathbf{E}_{t_1} \tag{3.3}$$

Therefore, to find the equivalent sources of Figure 3.3(c) we need to evaluate the tangential electric field at the air-dielectric interface, or $\mathbf{E}_t(x, y, z = 0)$. For small values of h, $\mathbf{E}_t$ decays rapidly moving out from the microstrip edge, thus the magnetic current will be confined to a region close to the microstrip edge. The simplest model for the magnetic currents is, then, just a line source located at the edge of the microstrip. The source must represent the total magnetic current,

$$M = \int_{x=0}^{\infty} \mathbf{E}_{t1} \cdot \mathbf{dx} \tag{3.4}$$

But this integral is nothing more than the voltage at the edge of the microstrip, a value more easily determined for thin substrates as,

$$M = V = \int_{z=0}^{h} -E_z dz = -E_z h \tag{3.5}$$

Thus we conclude that by placing magnetic current line sources along the edges of the planar components in accord with Schelkunoff's equivalence principle and by relating these sources to the edge voltages determined from the planar analysis, it becomes possible to evaluate the external fields of the upper half space. Such equivalent magnetic current sources for a bend are illustrated in Figure 3.4.

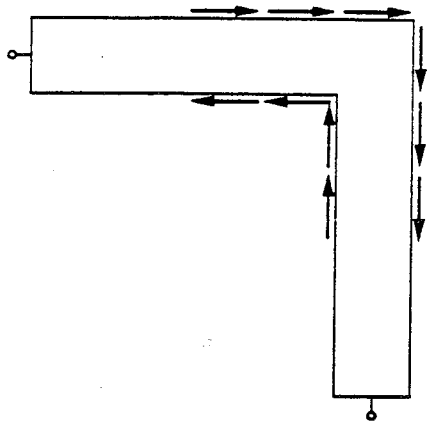

Figure 3.4: Magnetic Current Sources Along Edges of a Bend

3.2.2 The Mutual Admittance Matrix. As mentioned in Section 3.1, the elements of the multiport network shown in Figure 3.2 must account for the current induced at one port per unit voltage appearing at another port location. Consider two arbitrarily positioned ports. Without loss of generality, we may consider the first of these, port i, to be centered at the origin of the coordinate system as shown in Figure 3.5. Now, if port i is part of an

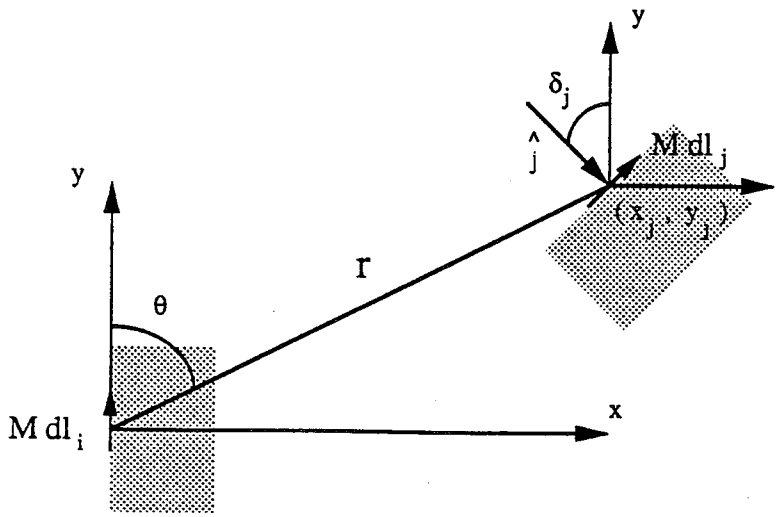

Figure 3.5. Coordinates for Calculating Coupling Between Two Magnetic Current Elements

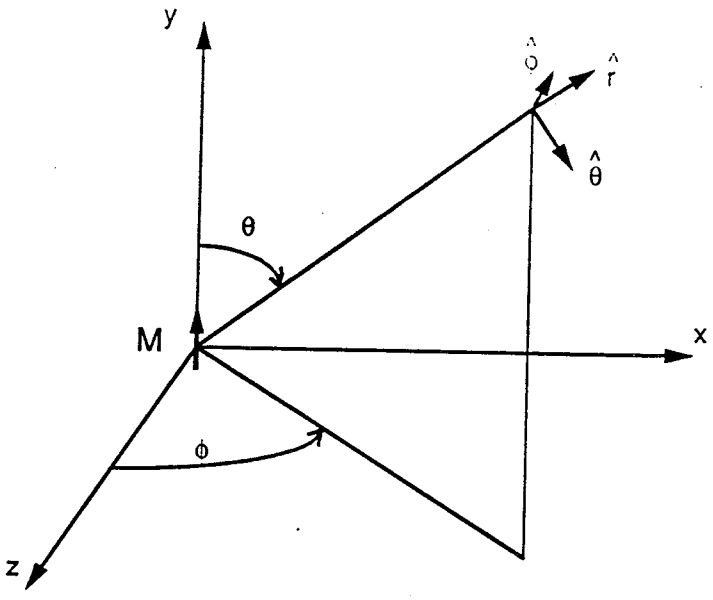

Figure 3.6. Coordinates for Finding Radiation Fields of a Magnetic Current Source M

excited circuit, a voltage, V_i , will appear at this location. From the voltage V_i we obtain an equivalent magnetic current which is placed at the edge of the port. From this source we must find the resulting current flowing into port j. To do so we first find the radiation fields of the magnetic current element at port i. This is done by using the electric vector potential , $\mathbf{F}$, which is given by,

$$\epsilon \mathbf{E} = -\nabla \times \mathbf{F} \tag{3.6}$$

and can be found from using the retarded potential, $\frac{e^{-jk_o r}}{r}$, to be

$$\mathbf{F} = \int_v \frac{\epsilon}{4\pi} \frac{\mathbf{M} e^{-jk_o r}}{r} dv \tag{3.7}$$

where k_o is the free-space wave number. Thus for the $\hat{y}$-directed magnetic current element of Figure 3.6, we have

$$dF_y = \left(\frac{\epsilon}{4\pi}\right) \frac{\mathbf{M} dl e^{-jk_o r}}{r} \tag{3.8}$$

In spherical coordinates this gives

$$F_r = F_y \cos\theta \tag{3.9}$$

$$F_\theta = -F_y \sin\theta \tag{3.10}$$

$$\text{and} \quad F_\phi = 0 \tag{3.11}$$

By symmetry, $\frac{\partial}{\partial\phi} = 0$, so

$$\nabla \times \mathbf{F} = \frac{\hat{a}_\phi}{r}\left(\frac{\partial(rF_\phi)}{\partial r} - \frac{\partial F_r}{\partial\phi}\right) \tag{3.12}$$

From comparison with equation 3.6 we get

$$E_\phi = \frac{-Mdl}{4\pi}\sin\theta\left(\frac{jk_o}{r} + \frac{1}{r^2}\right)e^{-jk_o r} \tag{3.13}$$

Applying Maxwell's equation,

$$\nabla \times \mathbf{E} = -j\omega\mu\mathbf{H} \tag{3.14}$$

we obtain for a magnetic current element in free space,

$$H_\theta = \frac{jk_o Mdl\sin\theta}{4\pi\eta_o r}\left(1 + \frac{1}{jk_o r} - \frac{1}{(k_o r)^2}\right)e^{-jk_o r} \tag{3.15}$$

and

$$H_r = \frac{Mdl\cos\theta}{2\pi\eta_o r^2}\left(1 + \frac{1}{jk_o r}\right)e^{-jk_o r} \tag{3.16}$$

where η_o is the intrinsic impedance of free space. For the purpose of finding the fields at port j, as in Figure 3.5 , however, we must account for the image effect produced by the conducting surface. The image source for a horizontal magnetic current element over a conducting sheet is directed with the same orientation, hence the fields due to the source M_i are given by equations 3.15 and 3.16 except that the field intensities of the upper half-space are twice those

given for the element of Figure 3.6. Thus the element of magnetic current, M_i of length dl_i, located at $(0,0)$ in the $z=0$ plane produces magnetic component H_θ and H_r at location (x_j, y_j) in the $z=0$ plane given by

$$H_\theta = 2 \times \frac{jk_o M_i dl_i \sin\theta}{4\pi\eta_o r}\left(1 + \frac{1}{jk_o r} - \frac{1}{(k_o r)^2}\right) e^{-jk_o r} \tag{3.17}$$

and

$$H_r = 2 \times \frac{M_i dl_i \cos\theta}{2\pi\eta_o r^2}\left(1 + \frac{1}{jk_o r}\right) e^{-jk_o r} \tag{3.18}$$

where $r = \sqrt{x_j^2 + y_j^2}$ and θ is as shown in Figure 3.5. The surface current density at (x_j, y_j) is

$$\mathbf{J} = \hat{a}_z \times \mathbf{H} \tag{3.19}$$

but we desire only the portion directed into the port j, or

$$J_j = (\hat{a}_z \times \mathbf{H}) \cdot \hat{j} \tag{3.20}$$

Taking this value to be uniform over the port width we have [6]

$$I_j = J_j dl_j \tag{3.21}$$

and

$$Y_{ji} = \frac{I_j}{V_i} = \frac{J_j dl_j}{V_i} \tag{3.22}$$

For coupling between circuit components, a mutual admittance matrix may be formed which includes the interactions between various ports of the planar components. Taking only interactions between different components we have [6]

$$[Y_m] = \begin{bmatrix} \mathbf{0} & [Y]_{IJ} & \cdots & [Y]_{IN} \\ [Y]_{JI} & \mathbf{0} & & \vdots \\ \vdots & & \ddots & \vdots \\ [Y]_{NI} & \cdots & \cdots & \mathbf{0} \end{bmatrix} \begin{matrix} \} \text{ Component I} \\ \} \text{ Component J} \\ \vdots \\ \} \text{ Component N} \end{matrix} \tag{3.23}$$

where **0** represents a null matrix and $[Y]_{IJ}$ represents a matrix filled with mutual admittances for the coupling ports of components I and J with each term calculated by equation 3.22.

3.2.3 Generalized Self-Conductance Network. While the mutual admittance matrix of equation 3.23 accounts for interactions between the ports of various planar components, the power lost to radiation needs to be evaluated as well. If the radiation fields for a collection of magnetic sources are deduced from superposition and integrated over a surface in the far-field, the radiated power, P_{rad}, is obtained. From P_{rad}, the edge conductances needed for the network of Figure 3.1 can be found using equation 3.1. To find P_{rad} and G_{r_n} by this method requires prior knowledge of the edge voltage distribution. Rather than obtaining the radiated power by this method, an approach based on interaction among various elementary sources is used which provides a conductance network without previous knowledge of the edge voltages. It relies on comparison of the radiation field for a collection of sources to the power dissipated in an equivalent network. Consider only two sources, $\mathbf{M}_1$ and $\mathbf{M}_2$, which give rise to the fields $\mathbf{E}_1$, $\mathbf{H}_1$, and $\mathbf{E}_2$ $\mathbf{H}_2$ as shown in Figure 3.7. From Poyntings theorem, we write [24]

$$P_{rad} = \frac{1}{2} Re \oint_S (\mathbf{E} \times \mathbf{H}^*) \cdot \mathbf{ds} \tag{3.24}$$

where S is an arbitrary surface enclosing the sources and P_{rad} represents the power flow out of the surface. Dissipation in the enclosed volume is assumed to be zero. For an equivalent two-port network as shown in Figure 3.8, the power dissipated within the network may be expressed as

$$P_{diss} = \frac{1}{2} Re\{V_1 I_1^* + V_2 I_2^*\} \tag{3.25}$$

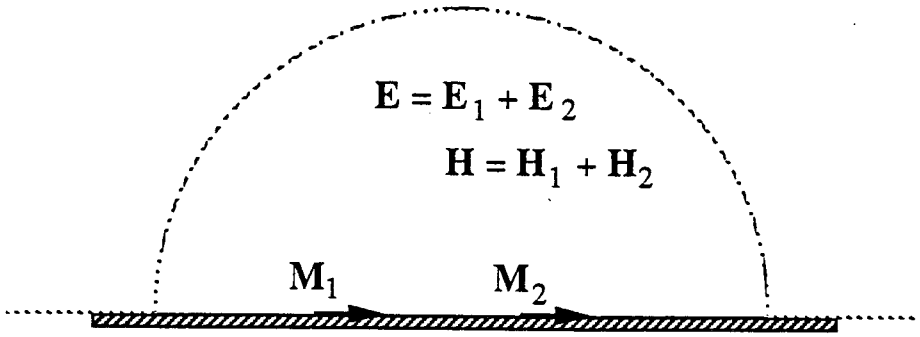

Figure 3.7: Two Magnetic Elements Producing Interacting Fields

Let the network be characterized by its admittance matrix $[Y]$. Then P_{diss} becomes

$$P_{diss} = Re\{V_1(Y_{11}\,V_1 + Y_{12}\,V_2)^* + V_2(Y_{21}\,V_1 + Y_{22}\,V_2)^*\}/2 \quad (3.26)$$

$$= Re\{V_1\,Y_{11}^*\,V_1^* + V_1\,Y_{12}^*\,V_2^* + V_2\,Y_{21}^*\,V_1^* + V_2\,Y_{22}^*\,V_2^*\}/2 \quad (3.27)$$

Now, the four terms of equation 3.27 will be related to four corresponding terms obtained by expanding equation 3.24 for $\mathbf{E} = \mathbf{E}_1 + \mathbf{E}_2$ and $\mathbf{H} = \mathbf{H}_1 + \mathbf{H}_2$. The details of expanding equation 3.24 for the sources of Figure 3.7 are given in Appendix C, with the result

$$P_{rad} = P_{rad_1} + P_{rad_2} - \frac{1}{2}Re\{\mathbf{H}_2^* \cdot \mathbf{M}_1\,dl_1\} - \frac{1}{2}Re\{\mathbf{H}_1^* \cdot \mathbf{M}_2\,dl_2\} \quad (3.28)$$

where P_{rad_1} is the radiated power of the source $\mathbf{M}_1$ acting independent of $\mathbf{M}_2$, P_{rad_2} is similarly the radiated power of $\mathbf{M}_2$, $\mathbf{H}_1$ is the H-field produced by the source $\mathbf{M}_1$ at the location of port 2, and $\mathbf{H}_2$ is the H-field produced by the

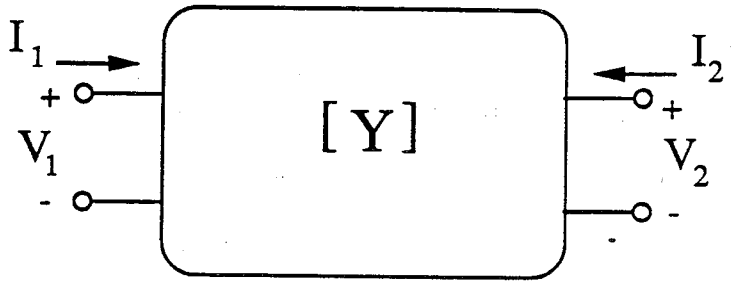

Figure 3.8. Two-Port Network Representing Radiation from Two Magnetic Current Sources $\mathbf{M}_1$ and $\mathbf{M}_2$

source $\mathbf{M}_2$ at the location of port 1. Relating like terms, we have

$$P_{rad_1} \longleftrightarrow Re\{V_1\, Y_{11}^*\, V_1^*\}/2 \tag{3.29}$$

$$P_{rad_2} \longleftrightarrow Re\{V_2\, Y_{22}^*\, V_2^*\}/2 \tag{3.30}$$

$$-Re\{\mathbf{H}_2^* \cdot \mathbf{M}_1\, dl_1\}/2 \longleftrightarrow Re\{V_1\, Y_{12}^*\, V_2^*\}/2 \tag{3.31}$$

$$-Re\{\mathbf{H}_1^* \cdot \mathbf{M}_2\, dl_2\}/2 \longleftrightarrow Re\{V_2\, Y_{21}^*\, V_1^*\}/2 \tag{3.32}$$

The task is now determining the Y-values in order to obtain the desired network model. Letting $Re(Y_{11}) = G_{11}$ in equation 3.29 we have

$$P_{rad_1} = \frac{1}{2} G_{11} |V_1|^2 \tag{3.33}$$

or

$$G_{11} = \frac{2\, P_{rad_1}}{|V_1|^2} \tag{3.34}$$

Similarly,

$$G_{22} = \frac{2\, P_{rad_2}}{|V_2|^2} \tag{3.35}$$

Since P_{rad_1} is proportional to $|V_1|^2$, the value of G_{11} is independent of the edge voltage. The power radiated by $\mathbf{M}_1$ can be found by the following expression,

$$P_{rad_1} = \frac{1}{2} Re \oint_S (\mathbf{E}_1 \times \mathbf{H}_1^*) \cdot \mathbf{ds} \tag{3.36}$$

and for S taken to be a large hemisphere we have

$$\mathbf{ds} = \hat{a_r}\, r^2 \sin\theta \, d\theta d\phi \tag{3.37}$$

and therefore,

$$P_{rad_1} = 4 \times \frac{1}{2} Re \int_{\phi=0}^{\pi} \int_{\theta=0}^{\pi} -E_\phi H_\theta^*\, r^2 \sin\theta \, d\theta d\phi \tag{3.38}$$

where E_ϕ and H_θ are the far-field expressions obtained by taking the dominant term in equations 3.15 and 3.16. The result is [25]

$$P_{rad_1} = \frac{1}{2} \left(\frac{|M_1|^2 \, dl_1^2}{90\lambda_o^2} \right) \tag{3.39}$$

So,

$$G_{11} = \left(\frac{dl_1^2}{90\lambda_o^2} \right) \tag{3.40}$$

and,

$$G_{22} = \left(\frac{dl_2^2}{90\lambda_o^2} \right) \tag{3.41}$$

since $M_1 = V_1$ and $M_2 = V_2$ from equation 3.5. To relate the expressions in equation 3.31, the voltages at the ports and mutual admittance on the right-hand side must be compared to the field quantities on the left side. But the relationship between the circuit-parameters and field quantities was already

established when the mutual admittance was derived in section 3.2.2. Recall that,

$$Y_{ji} = \frac{I_j}{V_i} = \frac{J_j\, dl_j}{V_i} \tag{3.42}$$

where

$$J_j = (\hat{a}_z \times \mathbf{H}) \cdot \hat{j} \tag{3.43}$$

Now, for comparison, $\mathbf{H}$ in this expression is the H-field present at the port j due to the magnetic current source M_i. Thus,

$$Y_{ji} = \frac{(\hat{a}_z \times \mathbf{H}) \cdot \hat{j}\, dl_j}{V_i} = \frac{-\mathbf{H}_i \cdot (\hat{a_z} \times \hat{j})\, dl_j}{V_i} \tag{3.44}$$

but, $\mathbf{M}_j = (\hat{a_z} \times \hat{j}) V_j$ so,

$$(\hat{a_z} \times \hat{j}) = \frac{\mathbf{M}_j}{V_j} = \frac{\mathbf{M}_j^*}{V_j^*} \tag{3.45}$$

and

$$Y_{ji} = \frac{-\mathbf{H}_i \cdot \mathbf{M}_j^*\, dl_j}{V_i\, V_j^*} \tag{3.46}$$

Therefore,

$$V_j\, Y_{ji}\, V_i^* = V_j \left(\frac{-\mathbf{H}_i \cdot \mathbf{M}_j^*\, dl_j}{V_i\, V_j^*} \right) V_i^* = -\mathbf{H}_i^* \cdot \mathbf{M}_j\, dl_j \tag{3.47}$$

so equations 3.31 and 3.32 may be satisfied by letting $Re(Y_{12}) = G_{12}$ and $Re(Y_{21}) = G_{21}$ where $G_{ij} = Re(Y_{ij})$ and Y_{ij} is determined from equation 3.22. These values, once again, are independent of the edge voltages. For the two-port just given, the network may be shown as in Figure 3.9. The procedure just outlined for the two-port network may be extended for N ports, in which

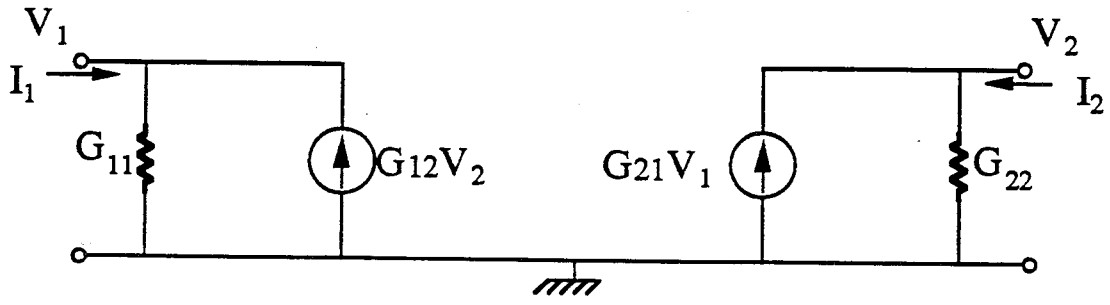

Figure 3.9: Circuit Representation for Generalized Self-Conductance Network

case the matrix, $[G]$, for a given component would appear as

$$[G] = \begin{bmatrix} G_{11} & Re\{Y_{12}\} & \cdots & Re\{Y_{1N}\} \\ Re\{Y_{21}\} & G_{22} & & \vdots \\ \vdots & & \ddots & \vdots \\ Re\{Y_{N1}\} & \cdots & \cdots & G_{NN} \end{bmatrix} \tag{3.48}$$

For more than one component, this may be combined with the mutual admittance matrix of equation 3.23 to give

$$[Y_m] = \begin{bmatrix} [G]_I & [Y]_{IJ} & \cdots & [Y]_{IN} \\ [Y]_{JI} & [G]_J & & \vdots \\ \vdots & & \ddots & \vdots \\ [Y]_{NI} & \cdots & \cdots & [G]_N \end{bmatrix} \begin{matrix} \} \text{ Component I} \\ \} \text{ Component J} \\ \vdots \\ \} \text{ Component N} \end{matrix} \tag{3.49}$$

From now on, the matrix $[Y_m]$ of equation 3.49 will be referred to as the mutual admittance matrix.

For comparison, consider the right-angle bend of Figure 3.10. This structure was analyzed previously using the Poynting Vector (PV) [1] method

and the (MNM) [8] approach with edge voltages obtained from planar analysis and edge conductances determined from the radiated power. Figure 3.11 shows these results with the results of the Generalized Conductance Network (GCN) overlaid for the fifty ohm line with $\epsilon_r = 2.2$. The radiation power plotted is normalized to one Watt of incident power at port 1 and plotted in dB. It can be seen that the different approaches yield nearly the same radiated power. This serves as a check for the dependability and implementation of the GCN.

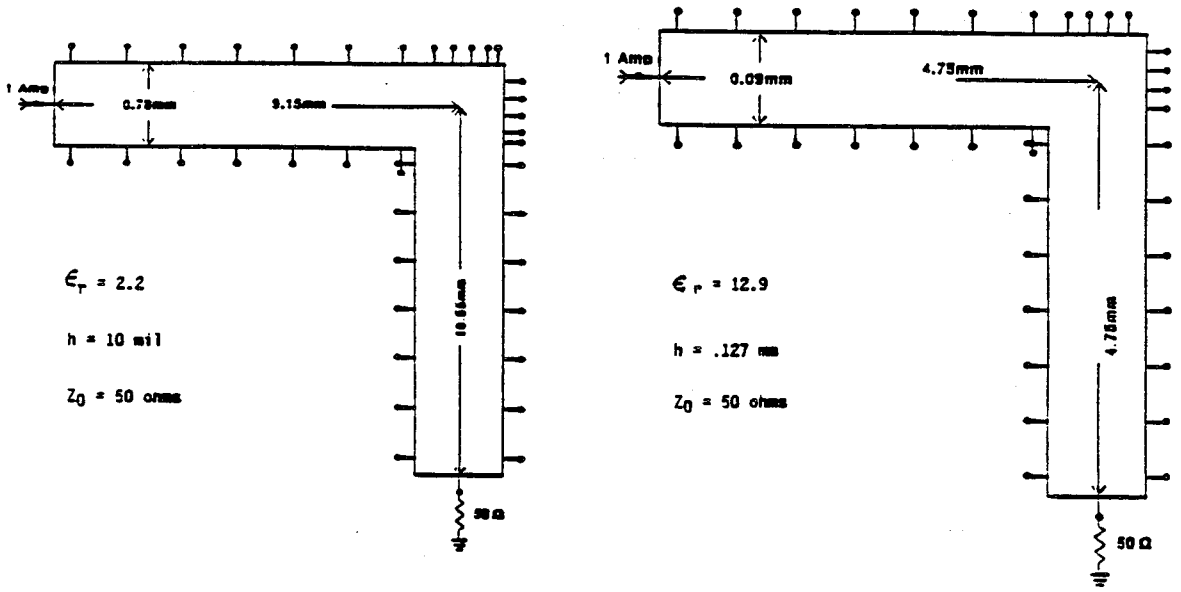

Figure 3.10: Right-Angled Bend for Radiation Loss Comparison

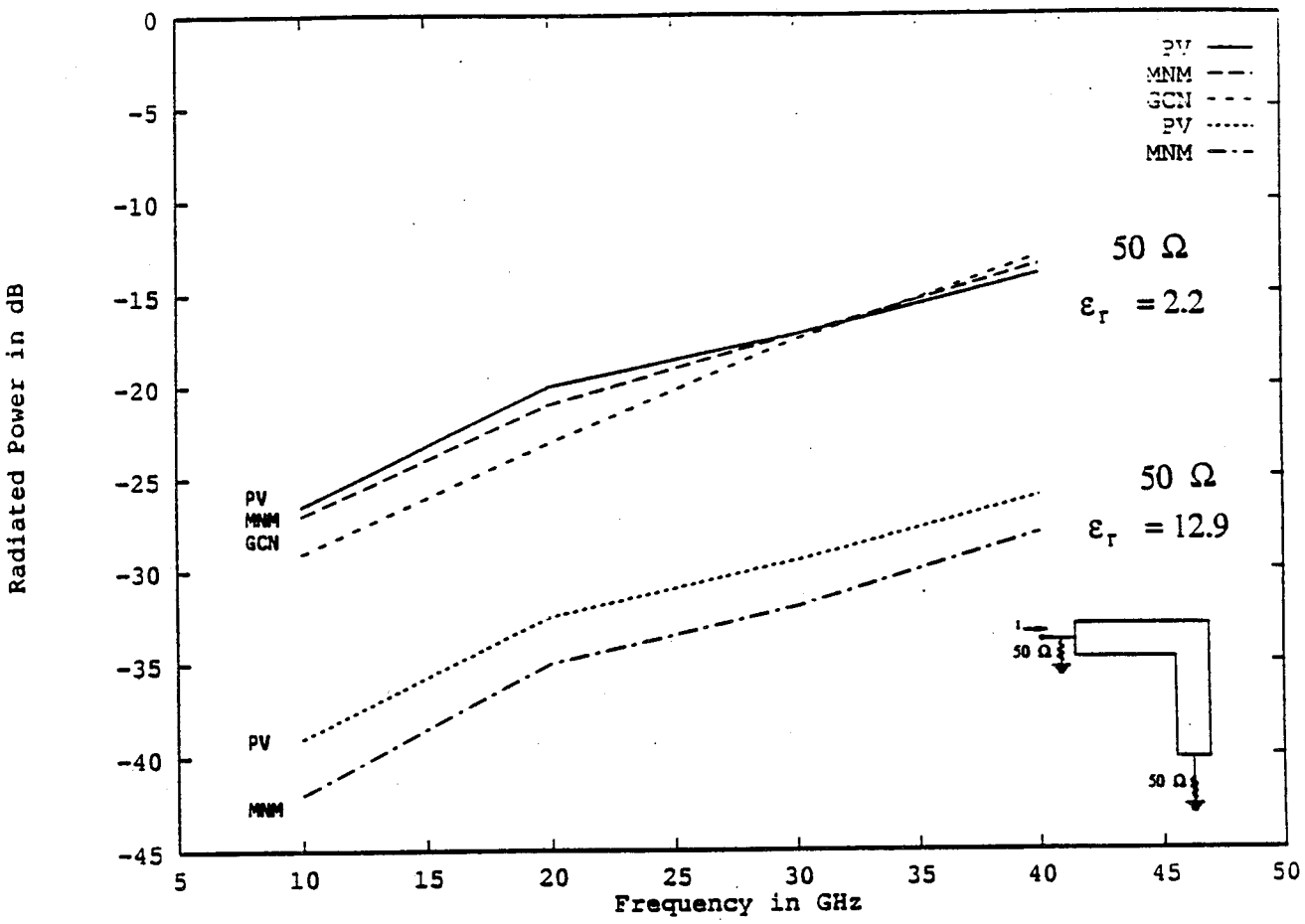

Figure 3.11: Radiated Power from a Right-Angled Bend

3.2.4 Modeling of Edge Fields by Distributed Magnetic Currents.

In section 3.2.1, representation of the fields external to a planar component was discussed. This was accomplished by using equivalent magnetic currents. It was mentioned that for small substrate heights the electric field decays rapidly away from the edge and therefore the current will be confined to a region close to the edge and may be approximated by a magnetic current line source as described. To obtain a more accurate model for the current distribution, an expression for the electric field at the air-dielectric interface is needed. A solution for the potential distribution has been reported, and asymptotic expressions for the fringing field obtained [26] as

$$E_{ox}(x \to 0^+) \approx V_o \left(\frac{1+\delta_e}{2\pi h}\right)^{\frac{1}{2}} \frac{1}{\sqrt{x}} \tag{3.50}$$

$$E_{ox}(x \to \infty) \approx V_o \frac{h}{\pi} \left(\frac{1-\delta_e}{1+\delta_e}\right) \frac{1}{x^2} \tag{3.51}$$

where $\delta_e = \frac{\epsilon_r - 1}{\epsilon_r + 1}$ and V_o is the voltage at the edge. From equation 3.50 we may write an expression for the magnetic current distribution near the edge as

$$M(x) = V_m \left(\frac{1+\delta_e}{2\pi\, h}\right)^{\frac{1}{2}} \frac{1}{\sqrt{x}} \tag{3.52}$$

Taking this current to be distributed over the region $x \in [0, L]$, we get the total current, which must equal the edge voltage, to be

$$V_o = \int_{x=0}^{L} M(x)\, dx = V_m \left(\frac{1+\delta_e}{2\pi h}\right)^{\frac{1}{2}} 2\sqrt{L} \tag{3.53}$$

The value, L, represents the limit of the region over which the current is confined, as shown in Figure 3.12. This gives a normalization for V_m which depends on the size of the region the current will be distributed over

$$V_m = \left(\frac{V_o}{\left(\frac{1+\delta_e}{2\pi\, h}\right)^{\frac{1}{2}} 2\sqrt{L}}\right) \tag{3.54}$$

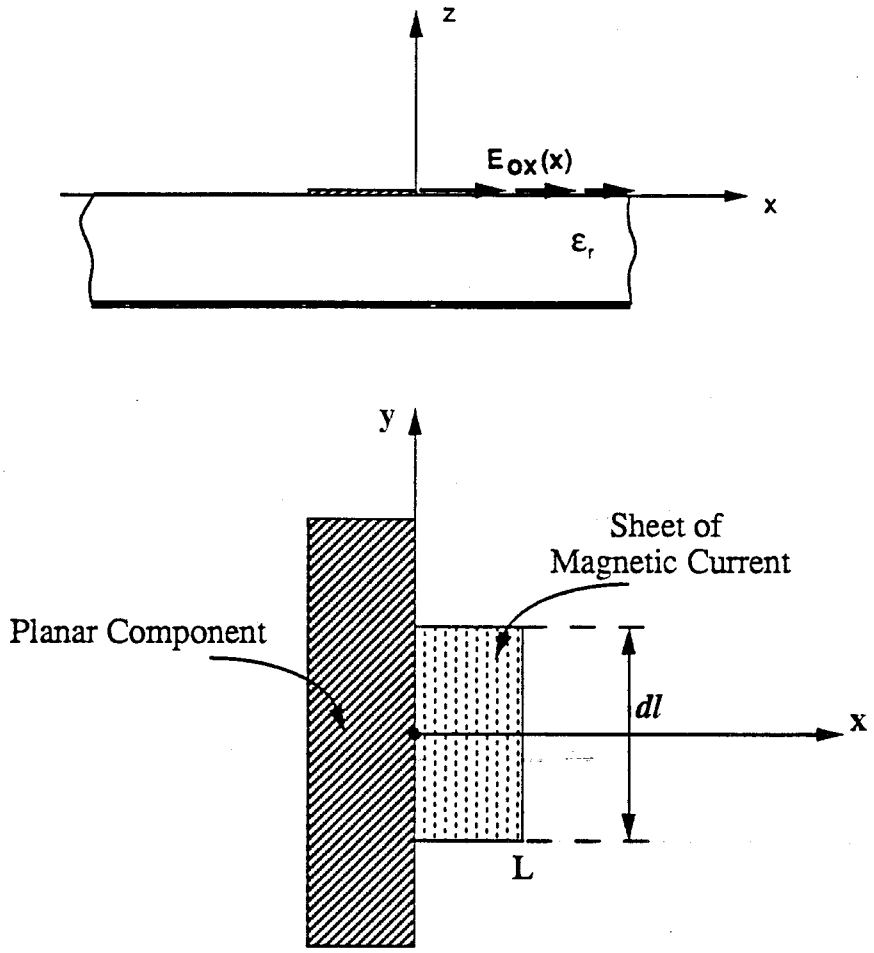

Figure 3.12: Magnetic Current Distribution Near the Edge

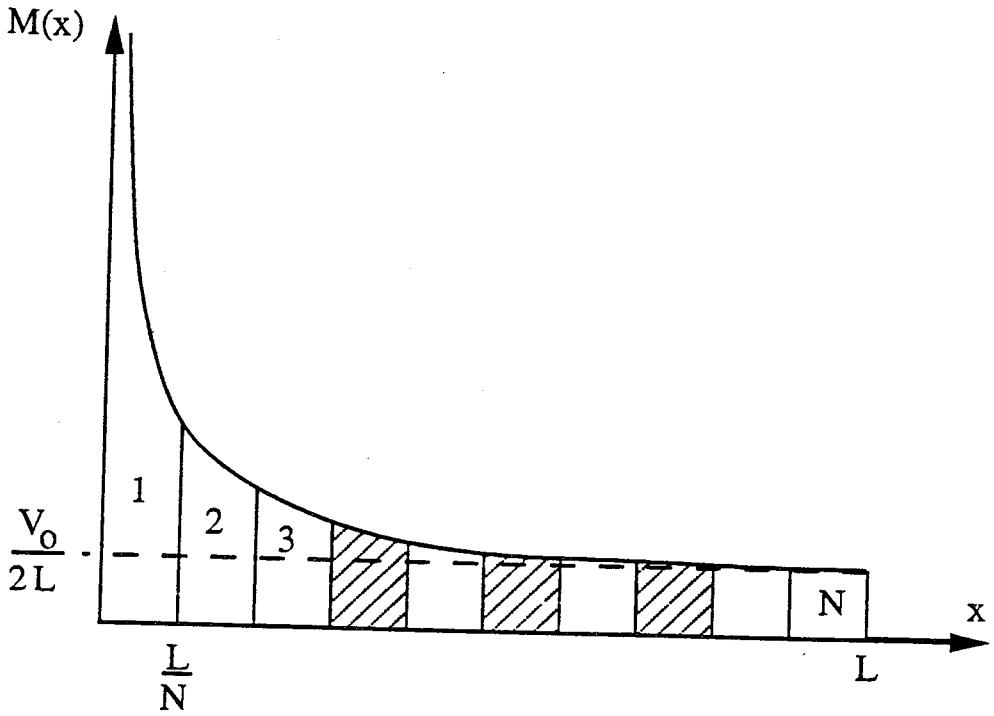

Figure 3.13: Regional Areas of Strips of Magnetic Current

and consequently M(x) reduces to

$$M(x) = \left(\frac{V_o}{2\sqrt{L}}\right)\frac{1}{\sqrt{x}} \tag{3.55}$$

From this expression for $M(x)$, we can derive a discrete line current representation for the current sheet. This is done by cutting the sheet into N strips and replacing the current of each strip by a line source. To obtain the amplitudes of the various current elements, the amount of current in each of the N strips is obtained by integrating M(x) for the regions 1, 2, 3, ...N, as shown in Figure 3.13. The current of region 1 may be found as

$$A_1 = \int_0^{\frac{L}{N}} M(x)\,dx = \left(\frac{V_o}{2\sqrt{L}}\right)\,2\sqrt{\frac{L}{N}} = \frac{V_o}{\sqrt{N}} \tag{3.56}$$

Similarly,

$$A_2 = \int_{\frac{L}{N}}^{\frac{2L}{N}} M(x)\,dx = \left(\frac{V_o}{2\sqrt{L}}\right) 2 \left(\sqrt{\frac{2L}{N}} - \sqrt{\frac{L}{N}}\right) = \left(\frac{V_o(\sqrt{2}-1)}{\sqrt{N}}\right) \quad (3.57)$$

By carrying out the integration for each strip, we find

$$A_m = \left(\frac{V_o}{\sqrt{N}}\right)(\sqrt{m} - \sqrt{m-1}) \quad (3.58)$$

and that

$$\sum_{m=1}^{N} A_m = \left(\frac{V_o}{\sqrt{N}}\right) \sum_{m=1}^{N} (\sqrt{m} - \sqrt{m-1}) = V_o \quad (3.59)$$

as it should. Thus it is possible to replace the current sheet of Figure 3.12 with discrete elements given by

$$M(x) = \sum_{m=1}^{N} A_m\,\delta(x - x_m) \quad (3.60)$$

where the amplitudes, A_m, are defined by equation 3.58 and the locations x_m are chosen to place each linear current element at the middle of its corresponding strip.

Now consider the task of evaluating the mutual admittance between two ports of a planar circuit as discussed in section 3.2.1. Extending the model to account for a continuous magnetic current distribution requires integration of the magnetic field over the regions of each magnetic sheet, or [7]

$$Y_{IJ} = -\frac{1}{V_I^* V_J} \int_{S_I}\int_{S_J} M_I^*(r_I) \cdot H(r_J - r_I) \cdot M_J(r_J)\,dS_J\,dS_I \quad (3.61)$$

Since the fields are assumed constant over the port widths dl_i and dl_j , this yields a double integral which maybe carried out numerically. For discrete sources, this translates to a double summation given by

$$Y_{IJ} = \sum_{i=1}^{N}\sum_{j=1}^{N} A_i\,A_j\,Y_{ij} \quad (3.62)$$

where Y_{ij} is calculated for each element as defined previously in equation 3.22. The values obtained for Y_{IJ} have been shown to converge very quickly with N, such that values obtained for N=6 or 10 agree very well with those obtained for N=100 or more. The accuracy of the approximation depends on how closely the N elements are spaced, a value clearly dependent upon the value chosen for L. Hence, for large values of L, a larger choice of N would be necessary for convergence. It must be pointed out, however, that M(x) was chosen from the asymptotic expression for x small. Since the function M(x) decays very slowly as x increases, (as evident from the A_m in eq. 3.58), large values of L must be avoided, and consequently a typical choice might be several times the substrate height. Clearly, other choices for determining the amplitudes may be investigated. For example, a trial might be to follow the $1/\sqrt{x}$ determination for only the first few elements and then select a function which decays more quickly thereafter. The primary constraint for any such choice is that the total current must sum to the edge voltage, or

$$\sum_{m=1}^{N} A_m = V_o \tag{3.63}$$

It is found when modeling two parallel coupled lines that the coupling given by the MNM approach (using a line-source magnetic current) decays more rapidly with separation distance than the coupling obtained from quasi-static computations. Thus it becomes necessary to use a magnetic current distribution transverse to the microstrip edge. A continuous magnetic current distribution was used previously in accordance with equation 3.49 for this problem [7]. For comparison, the discrete current distribution presented here was also applied to the case of two parallel coupled lines, and the results of both methods are shown in Table 3.1. The results from a quasi-static

analysis are shown in the table together with values obtained by the MNM approach for line-sources. Using a distributed current results in much greater coupling for larger separation distances, yet there is little difference between results obtained for the discrete and continuous source distributions.

Table 3.1: Comparison of Coupling: $|S_{14}|$ in dB

Comparison of Coupling: | S14 | in dB given for Quasi-static Computation and MNM
(Different MNM current models are shown)

Spacing d(mm)	Relative to height	Quasi-static Computations	Multiport Network Methods: Line Source	Continuous Distribution	Discrete Distribution	Dist. Limit	Number of Sources
1.2	4.72h	-33.2	-33.70	-33.45	-32.77	0.2h	5
2.1	8.27h	-40.18	-44.67	-39.50	-39.87	1.2h	5
3.0	11.81h	-45.14	-52.99	-44.15	-45.19	2.2h	8
5.0	19.69h	-52.66	-68.34	-51.48	-54.69	4.5h	12

3.3 Incorporation of Parasitic Coupling Effects in Circuits Analysis

Incorporation of parasitic coupling effects in MMIC circuit analysis starts with identifying sub-circuits (or regions) wherein the parasitic coupling effects are expected to be significant. Methodology discussed in this section makes use of conventional microwave circuit analysis for the rest of the circuit and magnetic current modeling of parasitic coupling in these selected sub-circuits. The procedure is illustrated by considering an example of an actual

MMIC layout.

Consider the single stage amplifier shown in Figure 3.14. This amplifier (designed and fabricated at *ITT GaAs Tech. Ctr.*) has been analyzed using the commercially available linear simulator named *Touchstone*[1]. The analysis makes use of coupled line models where appropriate, yet several regions can be identified for which couplings cannot be included by conventional microwave circuit analysis software. A procedure for implementing MNM approach for one of these regions follows. The discussion is based on the use of *Touchstone* software, but the procedure is applicable for other similar microwave CAD packages also. To begin, the dimensions of the sub-circuit (A, B, or C) are determined and its physical layout obtained. Next, the *Touchstone* file is modified so that it treats the selected sub-circuit as an individual component. This requires breaking the circuit along the boundary and introducing ports where they are needed. At this stage, essentially two networks are identified: the sub-circuit is one of the networks, and the remainder of the amplifier circuit is considered a second network. To analyze the complete amplifier, the analysis of both of these networks is needed. For sub-circuits of four ports or less, *Touchstone* can treat the sub-circuit as a single component and its S-parameters may be read from a data file. In this manner the planar analysis of the sub-circuit is re-introduced into the amplifier analysis. For sub-circuits having more ports, the recombination of the two networks is accomplished externally; the S-parameters of the remainder of the amplifier are output to a file (either as a complete circuit or in pieces) and then recombined with the selected sub-circuit analysis. Since *Touchstone* readily provides S-parameter data, the segmentation algorithm for S-parameters (see Appendix

[1]Registered Trade Mark of EEsof Inc., West Lake Village, CA

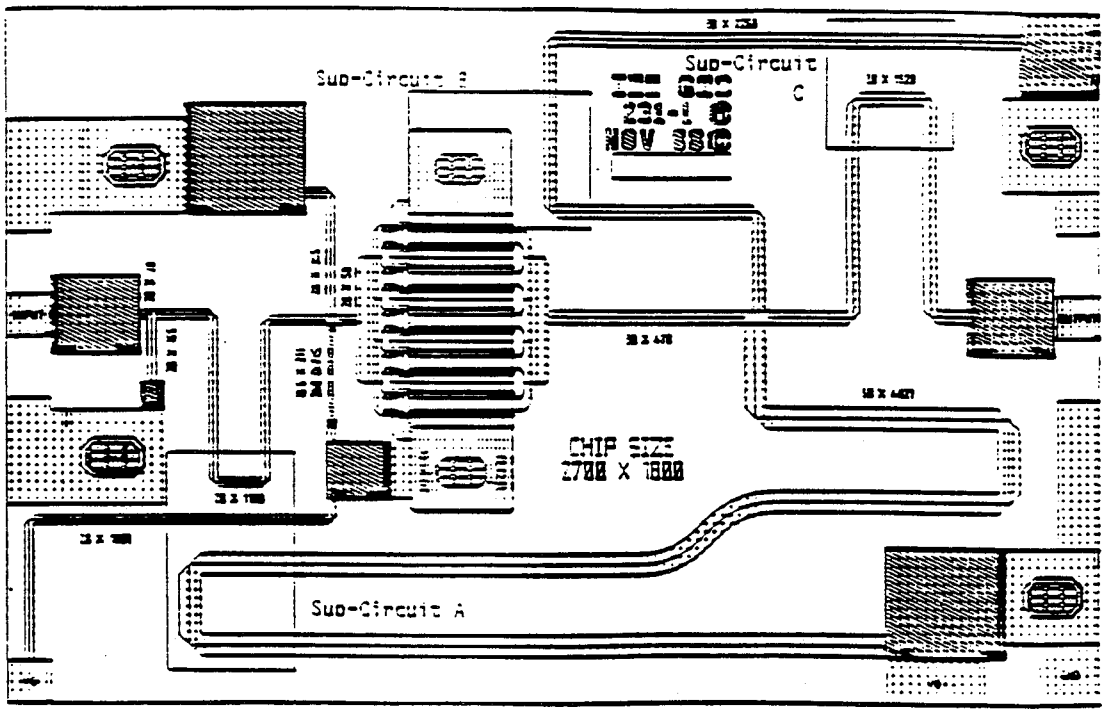

Courtesy of ITT

Figure 3.14. Single-Stage Amplifier Illustrating Implementation of the Parasitic Coupling Calculations

A) is used to recombine the two networks. By using the Subnetwork Growth Method mentioned in Chapter 2, very large and complex circuits may be handled. The only requirement is that, once an identified sub-circuit is removed, the remaining circuit may be broken into pieces for which the S-parameters can be obtained. Even for sub-circuit networks of four ports or less, the sensitivity analysis discussed in the following chapters requires the S-parameters of the remaining circuit, so it is important to sub-divide the circuit such that the S-parameters are accessible. As an example, consider removing sub-circuit *A* in Figure 3.14. The line providing the gate bias (which is at rf ground potential) has not been considered part of the microwave sub-circuit in this analysis, so sub-circuit A is a four-port network. Removal of this four-port, termed the Double U-bend configuration, leaves a six-port network for the remaining amplifier. The S-parameters for this six-port are not available from *Touchstone* as a single file, but by breaking it between the input and output stages, two four-ports are obtained and their S-parameters written out directly in a file. These may be recombined using the segmentation method to recover the desired six-port. The procedure just described is illustrated in Figure 3.15, and the main steps are itemized in the following list.

- Identify and Remove the Sub-Circuit
- Determine the Sub-Circuit Layout
- Obtain S-parameters for Remaining Circuit
- Analyze Sub-Circuit to Include Coupling
- Recombine Resulting Sub-Circuit Analysis to Obtain Circuit Analysis Including Coupling

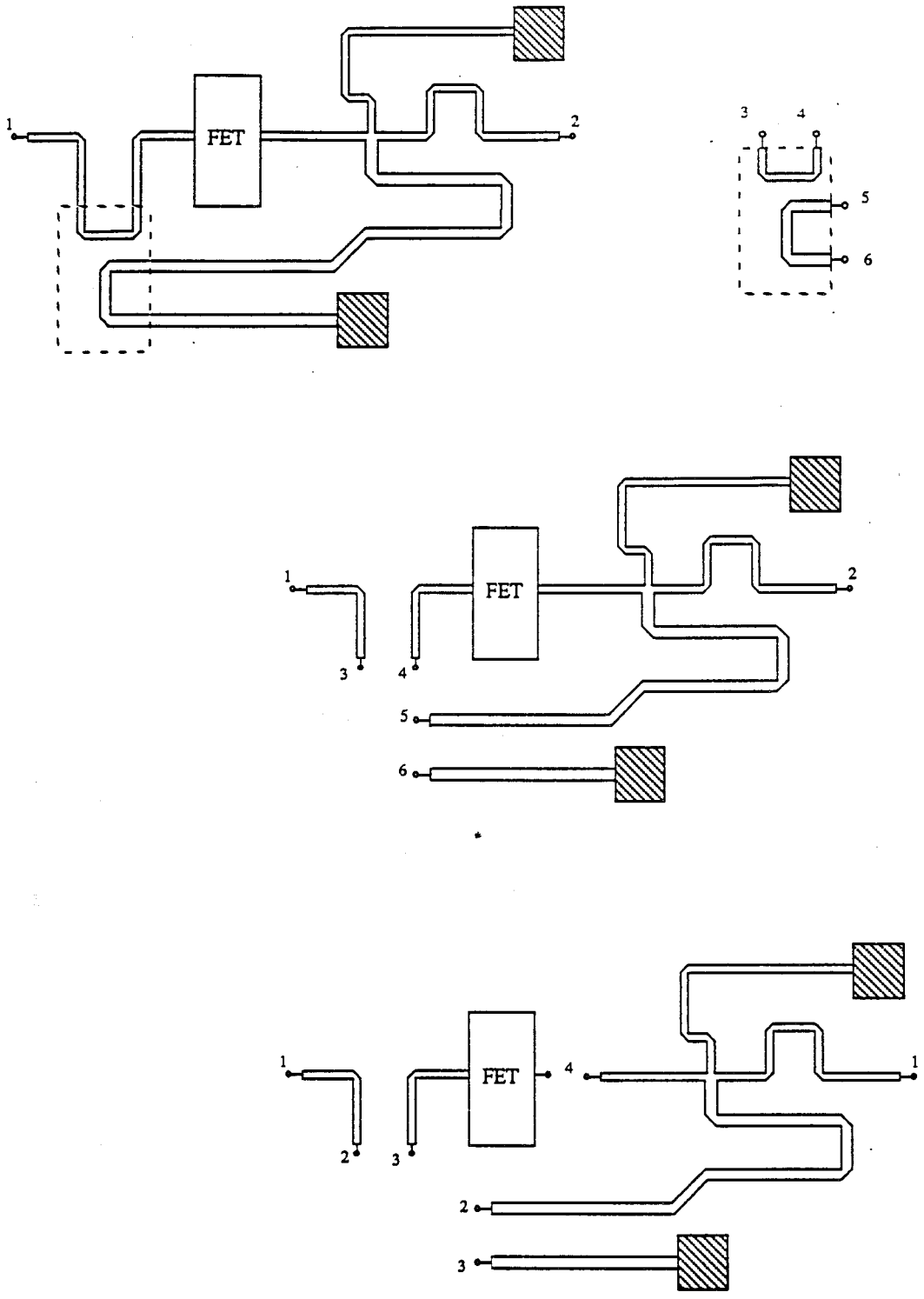

Figure 3.15: Procedure for Planar Analysis of Sub-circuit in a MMIC; (a) Removing Sub-circuit; (b) Sub-circuit Layout; (c) Remaining Circuit; (d) Breaking Remaining Circuit to Obtain S-parameters (two four-ports)

The procedure outlined above has been applied to sub-circuits A and B. The Double U-bend is a particularly interesting example because coupling between the bends introduces feedback from the output to input stage of the amplifier. In principle, if coupling was significant enough the amplifier might oscillate. This amplifier was designed to operate in the 5-6 GHz range and is a medium-gain amplifier. Hence, low levels of coupling are not expected to produce oscillation. Our analysis has, then, been carried out only for this frequency band. Figure 3.16 shows the sub-circuit layout for the Double U-bend, where the dis-

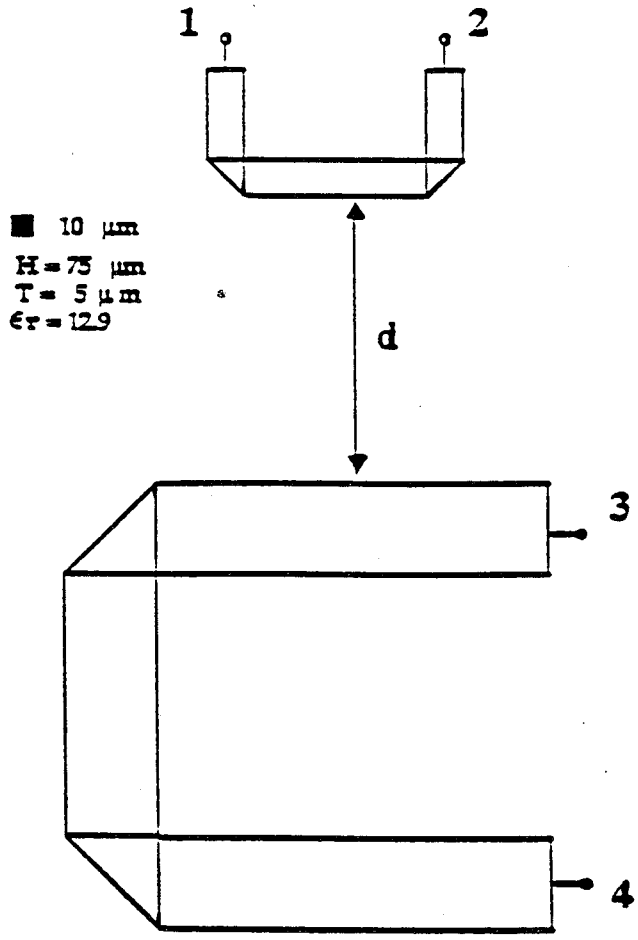

Figure 3.16: Layout for Sub-Circuit A, the Double U-bend

tance, d, gives the spacing between the bends. In the analysis of a sub-circuit comprised of separate components, obtaining the S-parameters for different sub-circuit layouts is accomplished very readily. Considering the two bends as an example, the largest part of the computational effort goes into obtaining the multiport Z-matrix representation for each of the bends individually. Further, because planar analysis is carried out for effective dimensions which are frequency dependent, a different model must be used for each frequency point to obtain the full accuracy of the model. Once the bends are characterized individually, however, only the Mutual Admittance Matrix (MAM) will depend on their relative locations. By establishing a local coordinate system for each component, the port locations can be described in this local system and then individual components may be easily moved around relative to each other in a global coordinate system. Thus, the effort required to obtain an analysis for the Double U-bend for several different distances, d, is just slightly more than that needed for a single separation distance. This is a nice feature for the designer who may quickly obtain a measure of the relative coupling for different sub-circuit layouts. Table 3.2 gives the four-port S-parameters of the Double U-bend evaluated at 5.5 GHz. The values without coupling are reported along with those obtained with coupling for physical separation $d = 160\mu m$ and for a separation of one substrate height ($d = 75\mu m$). The line-source current model was used, and the analysis repeated for each of the eleven frequency points, 5.0, 5.1, ... , 6.0 GHz, and the planar model for the sub-circuit introduced back into the amplifier analysis. Figure 3.17 shows the resulting amplifier performance. It can be seen that over this frequency band, the coupling between the bends results in a positive feedback leading to a slightly higher gain.

Table 3.2: S-parameters for Double U-bend at 5.5 GHz:

ROW#	REALPART	IMAGINARY PT	MAGNITUDE	DEG.
S11	-.2925480071E-03	.2289201989E-01	.2289388912E-01	90.73
S21	.9988236120E+00	-.4414726042E-01	.9997987740E+00	-2.53
S31	-.0000000000E+00	-.0000000000E+00	.0000000000E+00	********
S41	-.0000000000E+00	-.0000000000E+00	.0000000000E+00	********
S12	.9988236120E+00	-.4414726042E-01	.9997987740E+00	-2.53
S22	-.2925480071E-03	.2289201989E-01	.2289388912E-01	90.73
S32	-.0000000000E+00	-.0000000000E+00	.0000000000E+00	********
S42	-.0000000000E+00	-.0000000000E+00	.0000000000E+00	********
S13	-.0000000000E+00	-.0000000000E+00	.0000000000E+00	********
S23	-.0000000000E+00	-.0000000000E+00	.0000000000E+00	********
S33	.5799780397E-02	.1414841688E-01	.1529101543E-01	67.71
S43	.9843296720E+00	-.1678960139E+00	.9985459301E+00	-9.68
S14	-.0000000000E+00	-.0000000000E+00	.0000000000E+00	********
S24	-.0000000000E+00	-.0000000000E+00	.0000000000E+00	********
S34	.9843296720E+00	-.1678960139E+00	.9985459301E+00	-9.68
S44	.5799780397E-02	.1414841689E-01	.1529101544E-01	67.71

(a) Coupling Not Included

ROW#	REALPART	IMAGINARY PT	MAGNITUDE	DEG.
S11	-.3811675141E-03	.2273122173E-01	.2273441730E-01	90.96
S21	.9987378101E+00	-.4430096768E-01	.9997198553E+00	-2.54
S31	.2332876569E-03	-.9153603605E-02	.9156575893E-02	-88.54
S41	-.1082730167E-02	-.8953414261E-02	.9018643553E-02	-96.90
S21	.9987378101E+00	-.4430096768E-01	.9997198553E+00	-2.54
S22	-.3748354805E-03	.2274616116E-01	.2274924942E-01	90.94
S32	-.5929314667E-03	-.9088112595E-02	.9107434230E-02	-93.73
S42	-.1909238513E-02	-.8906275362E-02	.9108618585E-02	-102.10
S13	.2332876569E-03	-.9153603605E-02	.9156575893E-02	-88.54
S23	-.5929314667E-03	-.9088112595E-02	.9107434230E-02	-93.73
S33	.5633118110E-02	.1286502012E-01	.1404424303E-01	66.35
S43	.9840486275E+00	-.1691486113E+00	.9984803223E+00	-9.75
S14	-.1082730167E-02	-.8953414261E-02	.9018643553E-02	-96.90
S24	-.1909238513E-02	-.8906275362E-02	.9108618585E-02	-102.10
S34	.9840486275E+00	-.1691486113E+00	.9984803223E+00	-9.75
S44	.5410376008E-02	.1294137180E-01	.1402680551E-01	67.31

(b) Coupling Included (d=160)

ROW#	REALPART	IMAGINARY PT	MAGNITUDE	DEG.
S11	-.1090572450E-02	.2191182206E-01	.2193894469E-01	92.85
S21	.9980459118E+00	-.4509660980E-01	.9990642353E+00	-2.59
S31	-.1237657858E-03	-.2752153910E-01	.2752181739E-01	-90.26
S41	-.4054188205E-02	-.2678698734E-01	.2709204925E-01	-98.61
S12	.9980459118E+00	-.4509660980E-01	.9990642353E+00	-2.59
S22	-.1047665790E-02	.2198812920E-01	.2201307406E-01	92.73
S32	-.1513528247E-02	-.2727490832E-01	.2731687010E-01	-93.18
S42	-.5470399285E-02	-.2684865482E-01	.2740028347E-01	-101.52
S13	-.1237657858E-03	-.2752153910E-01	.2752181739E-01	-90.26
S23	-.1513528247E-02	-.2727490832E-01	.2731687010E-01	-93.18
S33	.4055511347E-02	.1890641736E-02	.4474561259E-02	24.99
S43	.9814471172E+00	-.1798381953E+00	.9977876630E+00	-10.38
S14	-.4054188205E-02	-.2678698734E-01	.2709204925E-01	-98.61
S24	-.5470399285E-02	-.2684865482E-01	.2740028347E-01	-101.52
S34	.9814471172E+00	-.1798381953E+00	.9977876630E+00	-10.38
S44	.1841442459E-02	.2680791884E-02	.3252315399E-02	55.51

(c) Coupling Included (d=75)

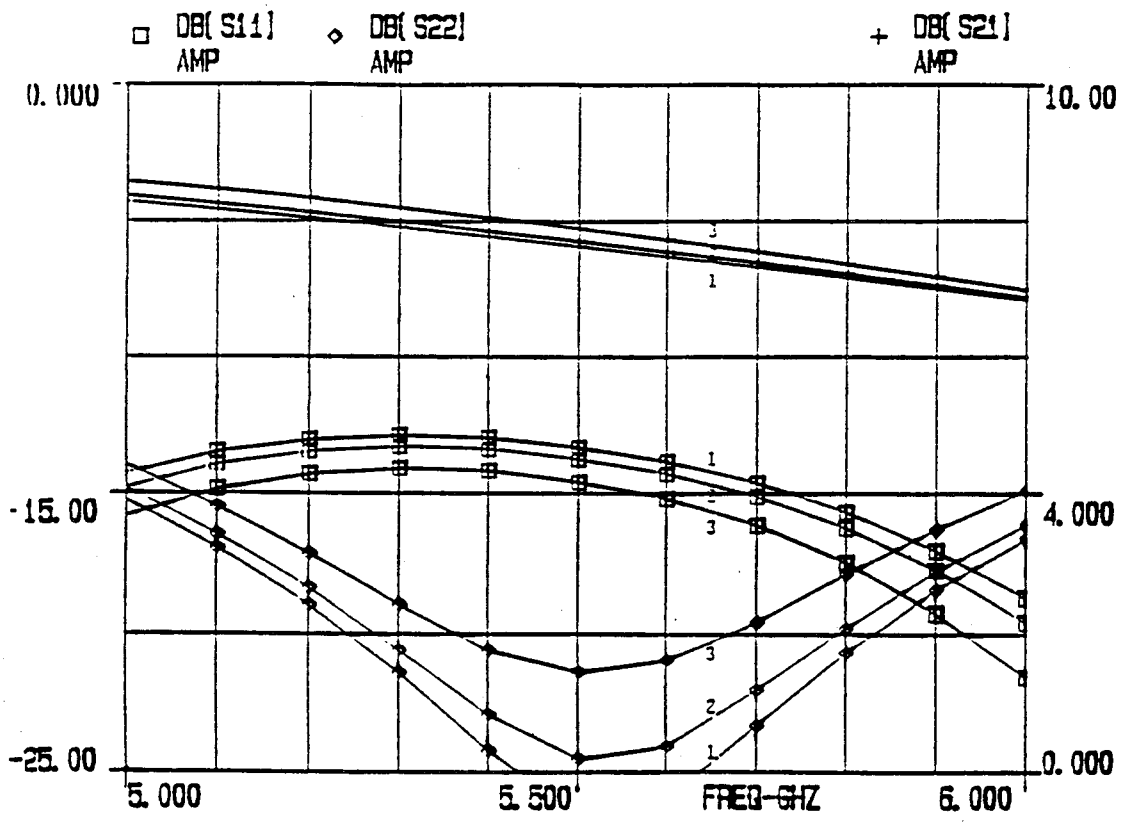

Trace 1 - without coupling

Trace 2 - includes coupling with d = 160 micron

Trace 3 - includes coupling with d = 75 micron

Figure 3.17: Single-Stage Amplifier Performance

CHAPTER 4

SUB-CIRCUIT SENSITIVITY TO CHANGES IN LAYOUT

Chapter 3 described the MNM approach as a means to characterize the couplings between planar circuit components. For larger circuits, a method was introduced to permit one to analyze selected portions of a circuit for coupling effects, while leaving the analysis of the remainder of the larger circuit unchanged. This provides the circuit designer a tool for evaluating coupling effects. Having a measure, not only of coupling, but of its effect on circuit performance can also be a help to the circuit designer. In this chapter, a procedure for obtaining the sensitivity of a selected sub-circuit to changes in its layout is developed. Sensitivity analysis based on the adjoint network method is discussed first. Then the differential mutual admittance for two magnetic line sources is found for changes in the relative position and orientation of their respective ports. This, taken together with geometrical considerations provides the basis for obtaining the sub-circuit sensitivity.

4.1 Sensitivity Equation from Adjoint Network Method

The adjoint network method for carrying out sensitivity calculations is based on Tellegen's theorem. To provide some background for the following discussion, consider the connected network graph shown in Figure 4.1. The letters a, b, ...j represent the various branches, while the numbers 1, 2, ...6 denote the nodes. For the graph to correctly describe a given network, three

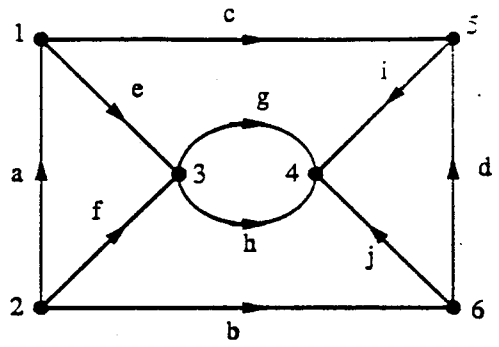

Figure 4.1: A Network Graph Example

things are needed. We must know how the branches are connected, the reference directions for branch currents and voltages (denoted by the arrows in fig. 4.1), and the branch characteristics which relate the current to voltage for each branch. An incidence matrix, A, is used to concisely describe the node connections and reference directions for a given graph. For a directed graph, G_d with n nodes and b branches, the incidence matrix is defined by an $n \times b$ matrix [27]

$$A = [a_{ij}]$$

where,

$a_{ij} = 1$ if branch j is incident at node i, and the arrow is pointing away from node i

$a_{ij} = -1$ if branch j is incident at node i, and the arrow is pointing toward node i

$a_{ij} = 0$ if branch j is not incident at node i

Although the incidence matrix contains no information about the branch characteristics, it completely describes the topology of a given network, N. Kirchhoff's voltage law and current law place constraints on branch voltages and

currents independent of the branch characteristics. Using the incidence matrix, A, Kirchhoff's voltage law may be expressed as

$$V = A^t V_n \tag{4.1}$$

where V represents the branch voltages and V_n the node voltages. Kirchhoff's current law may be expressed concisely as,

$$AI = 0 \tag{4.2}$$

with I being the branch currents. From this we obtain,

$$V^t I = (A^t V_n)^t I = V_n^t A I = 0 \tag{4.3}$$

For any network, say $\hat{N}$, having the same topology as N, we have $\hat{A} = A$, and therefore,

$$V^t \hat{I} = \hat{I}^t V = \hat{V}^t I = I^t \hat{V} = 0 \tag{4.4}$$

which is Tellegen's theorem [28]. It should be noted that in equation 4.3 the variables V and I represent the branch voltages and currents of the same network and hence $V^t I = 0$ implies that the power delivered to all branches is equal to zero, while equation 4.4 is a mixed expression with variables of two different networks and has no such physical interpretation. Two linear time-invariant networks, N, and $\hat{N}$ are said to be adjoint networks provided three conditions are met. First, they must have the same topology $\hat{A} = A$. Secondly, if the non-independent source brances, b, can be described by an admittance matrix, then $Y_b^t = \hat{Y}_b$. Finally, the corresponding independent sources of the two networks must be of the same kind, either voltage or current. From Tellegen's theorem and this definition of the adjoint network, the sensitivity

equation can be derived as follows. Tellegen's theorem will be applied to three different networks; the original network N, for which,

$$I = [Y][V] \tag{4.5}$$

the adjoint network $\hat{N}$,

$$\hat{I} = [\hat{Y}][\hat{V}] \tag{4.6}$$

and a perturbed network $\acute{N}$, whose branch currents are given by

$$\acute{I} = [\acute{Y}][\acute{V}] \tag{4.7}$$

where $\acute{I} = I + \Delta I$, and $\acute{V} = V + \Delta V$. Applying Tellegen's theorem to $\acute{N}$ and $\hat{N}$ gives

$$\hat{I}^t\acute{V} = \hat{V}^t\acute{I} = 0 \tag{4.8}$$

or,

$$\hat{I}^t(V + \Delta V) = \hat{V}^t(I + \Delta I) = 0 \tag{4.9}$$

Next, applying equation 4.4 to N and $\hat{N}$, we obtain

$$\hat{I}^t V = \hat{V}^t I = 0 \tag{4.10}$$

so equation 4.9 becomes

$$\hat{I}^t\Delta V = \hat{V}^t\Delta I = 0 \tag{4.11}$$

or equivalently,

$$\hat{I}^t\Delta V - \hat{V}^t\Delta I = 0 \tag{4.12}$$

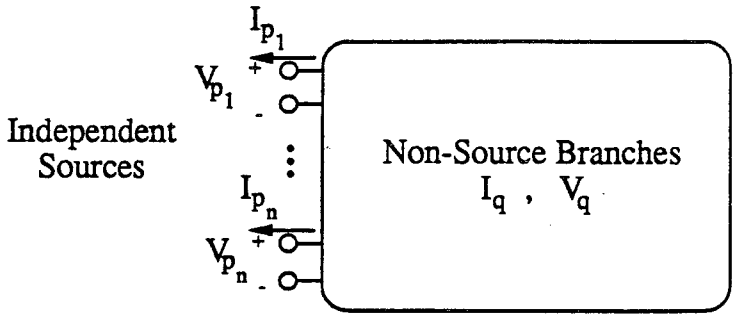

Figure 4.2: Network with Source Branches Extracted

By extracting the independent source branches as shown in Figure 4.2, branch currents for N and $\hat{N}$ become

$$I_q = [Y_q][V_q]; \quad I_p = -[Y_{sc}][V_p] \tag{4.13}$$

and

$$\hat{I}_q = [\hat{Y}_q][\hat{V}_q]; \quad \hat{I}_p = -[\hat{Y}_{sc}][\hat{V}_p] \tag{4.14}$$

where

$$\hat{Y}_{sc} = Y_{sc}^t \tag{4.15}$$

and

$$\hat{Y}_q = Y_q^t. \tag{4.16}$$

For this notation, equation 4.12 becomes

$$(\hat{I}_p^t \Delta V_p + \hat{I}_q^t \Delta V_q) - (\hat{V}_p^t \Delta I_p + \hat{V}_q^t \Delta I_q) = 0 \tag{4.17}$$

or equivalently,

$$(\hat{V}_p^t \Delta I_p - \hat{I}_p^t \Delta V_p) = (\hat{V}_q^t \Delta I_q - \hat{I}_q^t \Delta V_q) \tag{4.18}$$

Now, taking the perturbations in $\acute{N}$ to be small, we write,

$$\Delta I_q = \Delta(Y_q V_q) = \Delta Y_q V_q + Y_q \Delta V_q \tag{4.19}$$

so the right side of equation 4.18 becomes

$$\hat{V}_q^t(\Delta Y_q V_q + Y_q \Delta V_q) - \hat{I}_q^t \Delta V_q = \hat{V}_q^t \Delta Y_q V_q + V_q^{\hat{t}} Y_q \Delta V_q - \hat{I}_q^t \Delta V_q \tag{4.20}$$

but,

$$\hat{I}_q^t = \hat{V}_q^t \hat{Y}_q^t \tag{4.21}$$

giving on the left hand side of equation 4.20,

$$\hat{V}_q^t \Delta Y_q V_q + \hat{V}_q^t Y_q \Delta V_q - \hat{V}_q^t \hat{Y}_q^t \Delta V_q \tag{4.22}$$

which, for

$$\hat{Y}_q = Y_q^t \tag{4.23}$$

yields only

$$(\hat{V}_q^t \Delta I_q - \hat{I}_q^t \Delta V_q) = \hat{V}_q^t \Delta Y_q V_q \tag{4.24}$$

Similarly for external currents (Figure 4.2),

$$\Delta I_p = -\Delta(Y_{sc} V_p) = -\Delta Y_{sc} V_p - Y_{sc} \Delta V_p \tag{4.25}$$

the left-hand side of equation 4.18 reduces to the single term

$$-(\hat{V}_p^t \Delta I_p - \hat{I}_p^t \Delta V_p) = \hat{V}_p^t \Delta Y_{sc} V_p \tag{4.26}$$

The result is the sensitivity equation

$$\hat{V}_p^t \Delta Y_{sc} V_p = \hat{V}_q^t \Delta Y_q V_q. \tag{4.27}$$

In this equation, V_p and $\hat{V}_p$ represent the source voltages applied at the external ports of the original and adjoint networks, respectively. The voltages V_p and $\hat{V}_p$ are for the non-source branches of N and $\hat{N}$ under the excitations V_p and $\hat{V}_p$. The matrix ΔY_q is the differential matrix obtained from the non-source branches of the perturbed network, and ΔY_{sc} is the desired sensitivity at the external ports. For the sensitivity analysis of parasitic couplings from MNM, ΔY_{sc} represents the sensitivity at the external ports as found from ΔY_q, which we will call the differential mutual admittance matrix. The next section discusses how this differential mutual admittance matrix (DMAM) is obtained for changes in the sub-circuit layout.

4.2 The Differential Mutual Admittance Matrix

Consider a simple circuit having two components as in Figure 4.3. By

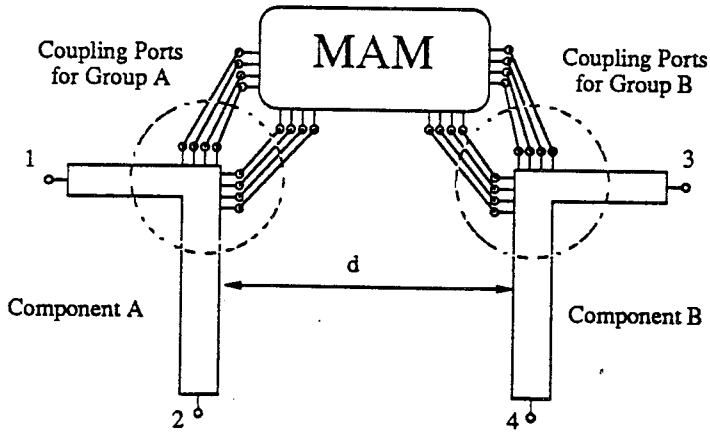

Figure 4.3: Two Right-Angle Bends Example for Sensitivity Analysis

introducing a number of coupling ports at the corners of each of the right-angle bends, the coupling between the bends is included using MNM. The sensitivity analysis seeks to determine the changes in the external port S-parameters

resulting from a given change in the layout. As an example, consider changing the distance, d, between the bends. In this case the sensitivity analysis would give the change in the four-port S-parameters, ΔS, for a given change in distance, Δd. Thus for Δd taken to be an incremental change, the sensitivity analysis yields $\partial S/\partial d$. Equation 4.27 may be used, but ΔY_q must be found in order to apply this equation. Finding the DMAM can be done one term at a time by finding ΔY_{ij} for each of the coupled ports. Since ports within the same component don't move relative to each other, the portion of the DMAM representing ports of the same component will be null. Finding the other terms requires two things. First, we must know how the value of Y_{ij} for any two ports i and j varies as port j is shifted relative to port i. Second, we must determine how every coupling port of one component gets shifted relative to every coupling port of other components when the components themselves are shifted relative to one another.

4.2.1 Differentiation of the Expression for Y_{ij}. The first requirement for obtaining the DMAM may be accomplished by a straightforward, albeit somewhat lengthy, differentiation of Y_{ij}. Consider Y_{ij} to be defined by equation 3.22. We consider one of the ports to be held fixed, but permit the other port to move. Thus the values needed to obtain ΔY_{ij} for a change in the layout are

$$\frac{\partial Y_{ij}}{\partial x_j}, \quad \frac{\partial Y_{ij}}{\partial y_j}, \quad \text{and} \quad \frac{\partial Y_{ij}}{\partial \alpha_j}$$

Differentiation of Y_{ij} with respect to these varaibles has been carried out, and the results are included in Appendix D. It is worth noting that were Y_{IJ} defined by equation 3.61, ΔY_{IJ} would represent the change in Y_{IJ} as surface S_J is shifted relative to surface S_I. Leaving S_I fixed, this shift represents a change

in the limits of the integral over S_J. And if this integration is not carried out analytically, obtaining an expression for ΔY_{IJ} becomes difficult. For Y_{IJ} defined by equation 3.62, however, we may write directly,

$$\Delta Y_{IJ} = \sum_{i=1}^{N} \sum_{j=1}^{N} A_i \, A_j \, \Delta Y_{ij} \tag{4.28}$$

where A_i and A_j are defined by equation 3.58. So, whether Y_{ij} is given by equation 3.22 or 3.62, expressions for ΔY_{ij} have been obtained which, when combined with the necessary geometrical information will yield the differential mutual admittance matrix.

4.2.2 Geometrical Considerations. In the general case, the DMAM must be determined when groups of coupling ports will be moved relative to each other. Typically, this would correspond to a movement of individual components, and the coupling ports of each component would form their own groups. If sensitivity to coupling within a single component is desired, then the ports of one component could be divided into more than one group. However, this discussion will assume that each component has a single group of coupling ports associated with it. For example, consider Figure 4.3. One of the bends, component A, has coupling ports at the corner which will be treated as a group and therefore will not move relative to each other. The same is true of the coupling ports of bend B. To define the port movement, a local coordinate system is assigned to each of the components, or groups of ports. Then every port in each group is defined by its position in its local coordinate system. In this way, changes in the layout are defined in terms of the movement of the local coordinate systems. To facilitate this, a global system is established and each system is positioned within it. By determining the transformation from the local to global coordinates, the movement of an individual coupling port

may be determined from the corresponding movement of its local system. This is shown in Figure 4.4. The local system is positioned within the global system

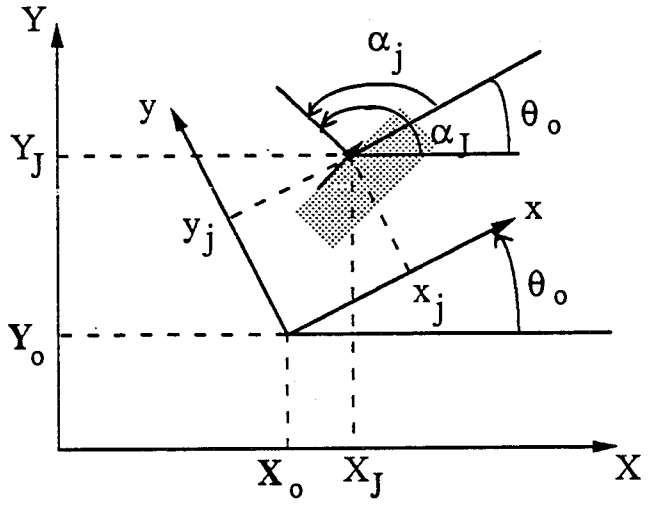

Figure 4.4: Transformation from Local (x_j, y_j) to Global (X, Y) Coordinates

by the coordinates (X_0, Y_0) and oriented at an angle Θ_0. The individual port j is positioned within its local system according to (x_j, y_j, θ_j). We can obtain the position of port j in the global system by the coordinate transformation

$$X_J = X_0 + x_j \cos\Theta_0 \tag{4.29}$$

$$Y_J = Y_0 + y_j \cos\Theta_0 \tag{4.30}$$

$$\alpha_J = \alpha_j + \Theta_0 \tag{4.31}$$

so, for translational movements, we obtain

$$\frac{\partial X_J}{\partial X_0} = 1 \quad \text{and} \quad \frac{\partial Y_J}{\partial Y_0} = 1 \tag{4.32}$$

and for a rotation of the local axis, we have

$$\frac{\partial \alpha_J}{\partial \Theta_0} = 1, \quad \frac{\partial X_J}{\partial \Theta_0} = -x_j \sin\Theta_0, \quad \text{and} \quad \frac{\partial Y_J}{\partial \Theta_0} = -y_j \sin\Theta_0 \tag{4.33}$$

Referring to Figure 4.5(a), we take the local system A to be shifted at an angle Θ_{mv} relative to system B. And, from Figure 4.5(b), we obtain

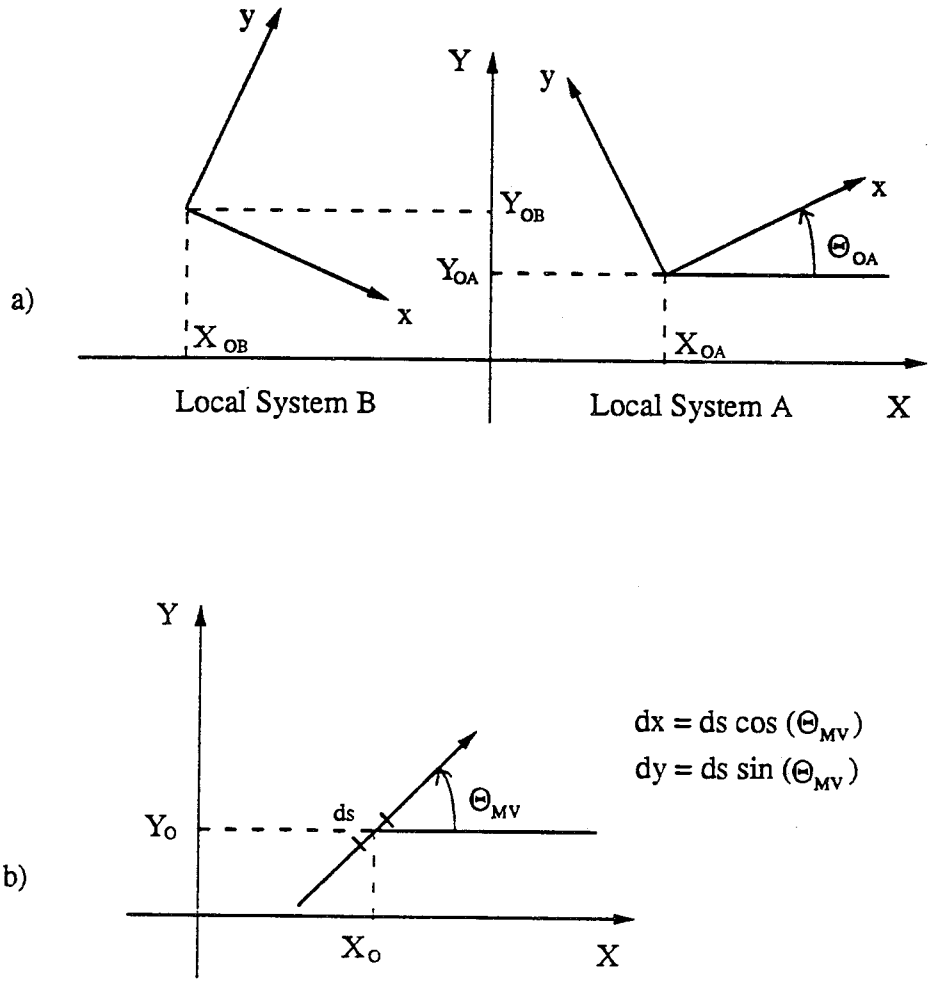

Figure 4.5: Translational Movement of Local Systems

$$\frac{\partial Y_{ij}}{\partial S} = \frac{\partial Y_{ij}}{\partial X_0}\cos\Theta_{mv} + \frac{\partial Y_{ij}}{\partial Y_0}\sin\Theta_{mv} \tag{4.34}$$

If both system A and B are to be shifted at the angles Θ_{mv_a} and Θ_{mv_b}, respectively, then their relative motion may be determined from

$$\Theta_{mv} = \arctan\left(\frac{\sin\Theta_{mv_a} - \sin\Theta_{mv_b}}{\cos\Theta_{mv_a} - \cos\Theta_{mv_b}}\right) \tag{4.35}$$

This approach has been applied to obtain the relative motion for any number of components, each moving at an angle Θ_{mv_i}. When considering the rotation of a local axis, however, it has been assumed that only one component will be rotated at a time. Thus we may write,

$$\frac{\partial Y_{ij}}{\partial \Theta_0} = \frac{\partial Y_{ij}}{\partial X_J} \cdot \frac{\partial X_J}{\partial \Theta_0} + \frac{\partial Y_{ij}}{\partial Y_J} \cdot \frac{\partial Y_J}{\partial \Theta_0} + \frac{\partial Y_{ij}}{\partial \alpha_J} \cdot \frac{\partial \alpha_J}{\partial \Theta_0} \tag{4.36}$$

So from equations 4.34 and 4.36 it is possible to obtain the relative motion between any two coupling ports of the various components. To do this, the expressions for $\partial Y_{ij}/\partial x_j$, $\partial Y_{ij}/\partial y_j$, and $\partial Y_{ij}/\partial \alpha_j$ given in Appendix D are used. Applying this procedure yields the diffferential mutual admittance matrix of the form

$$[\Delta Y_q] = \begin{bmatrix} \mathbf{0} & [\Delta Y]_{IJ} & \cdots & [\Delta Y]_{IN} \\ [\Delta Y]_{JI} & \mathbf{0} & & \vdots \\ \vdots & & \ddots & \vdots \\ [\Delta Y]_{NI} & \cdots & \cdots & \mathbf{0} \end{bmatrix} \begin{matrix} \} \text{ Component I} \\ \} \text{ Component J} \\ \vdots \\ \} \text{ Component N} \end{matrix} \tag{4.37}$$

4.3 Sub-Circuit Sensitivity

From the results obtained in sections 4.1 and 4.2, all the information needed to obtain the sensitivity of the external port parameters to a specified change in the layout is available. The method can be illustrated by considering the networks shown in Figure 4.6. The first network, (a), is for the uncoupled circuit where ports p_1 and p_2 are external ports and ports q_1 – q_3 are the coupling ports to be connected to the MAM, (b). From the segmentation procedure, the voltages at the interconnection ports, V_q, may be obtained for the excitations V_p (see equation A.16). For sensitivity analysis, the voltages $\hat{V}_q$ are also needed for the adjoint network, $\hat{N}$, in terms of the excitations $\hat{V}_p$. Recall that $\hat{Y} = Y^t$ for the adjoint network, so for a reciprocal network

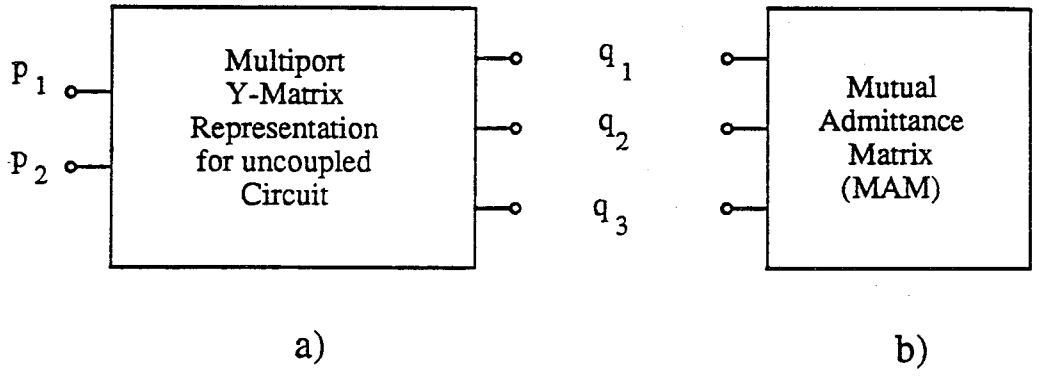

Figure 4.6: Obtaining External Port Parameters with Coupling Included

the adjoint network and original network are identical, and $\hat{V}_q$ has the same relationship to $\hat{V}_p$ as V_q to V_p. If the network is not reciprocal, the segmentaton procedure must be carried out for the adjoint network as well. In either case we have determined V_q and $\hat{V}_q$ in terms of the voltages at the external ports. For the example shown in Fig. 4.6, the senstivity equation 4.27 may be expanded as

$$\left[\hat{V}_{p_1}, \hat{V}_{p_2}\right]\begin{bmatrix} \Delta Y_{11} & \Delta Y_{12} \\ \Delta Y_{21} & \Delta Y_{22} \end{bmatrix}\begin{bmatrix} V_{p_1} \\ V_{p_2} \end{bmatrix}=\left[\hat{V}_{q_1}, \hat{V}_{q_2}, \hat{V}_{q_3}\right]\begin{bmatrix} \Delta Y_{ij} \\ DMAM \end{bmatrix}\begin{bmatrix} V_{q_1} \\ V_{q_2} \\ V_{q_3} \end{bmatrix} \quad (4.38)$$

To obtain ΔY_{11}, then, we set $V_{p_1} = \hat{V}_{p_1} = 1$ and $V_{p_2} = \hat{V}_{p_2} = 0$, and from the corresponding values of V_q and $\hat{V}_q$ for these excitations together with the DMAM evaluate the right hand side of equation 4.38. The other sensitivities are likewise obtained by selecting the appropriate excitations for the original and adjoint networks. If the interconnection voltages are determined from, $V_q = [T_v]\, V_p$ and $\hat{V}_q = [\hat{T}_v]\, \hat{V}_p$ then evaluating the right hand side of equation 4.38 is a matter of selecting the appropriate column of $[T_v]$ and row

of $[\hat{T}_v]^t$. In this way, we get a general expression for the sensitivities. The sensitivity $\Delta Y_{sc_{ij}}$ in 4.38 is evaluated as

$$\Delta Y_{sc_{ij}} = (i^{th} \text{ row of } [\hat{T}_v]^t) \cdot [DMAM] \cdot (j^{th} \text{ column of } [T_v]) \qquad (4.39)$$

Thus from the DMAM and the matrices $[T_v]$ and $[\hat{T}_v]$, ΔY_{sc} may be found from equation 4.39.

It is more common to express circuit characteristics in terms of S-parameters, and it will also be necessary to have the sub-circuit described in terms of S-parameters in order to implement this procedure for large circuits (see Section 3.3). So it is desirable to obtain the sub-circuit sensitivity in terms of S-parameters as well. This can be done by differentiation of the expression for S-parameters in terms of Y-parameters, which may be written as

$$S = \sqrt{Z_0}(Y_0 - Y)(Y_0 + Y)^{-1}\sqrt{Y_0} \qquad (4.40)$$

From which we obtain,

$$\Delta S = -\sqrt{Z_0}\{I - (Y_0 - Y)(Y_0 + Y)^{-1}\}\Delta Y(Y_0 + Y)^{-1}\sqrt{Y_0} \qquad (4.41)$$

where I is the identity matrix, Z_0 and Y_0 give the reference impedances for the external ports, and ΔY is the sensitivity matrix obtained from applying equation 4.39.

This procedure has been implemented and applied to the Double U-bend configuration discussed in section 3.3. In that section, the S-parameters for the Double U-bend were reported without coupling and for two different separation distances. By calculating the S-parameters for two distances which are close together, it is possible to obtain a value for sensitivity using the finite difference approach,

$$\frac{\Delta S_{ij}}{\Delta d} = \left(\frac{S_{ij}(d + \Delta d) - S_{ij}(d - \Delta d)}{2\Delta d}\right) \qquad (4.42)$$

The finite difference approach requires some discussion. In principle, it is possible to obtain sensitivities by this method by taking the difference Δd to be very small. Indeed, as Δd approaches zero, the left hand side of equation 4.42 becomes the differential, $\partial S_{ij}/\partial d$. Yet the evaluation of equation 4.42 requires subtracting the two nearly equal function values $S_{ij}(d+\Delta d)$ and $S_{ij}(d-\Delta d)$. These two constraints would, therefore, influence the choice of Δd in opposite directions. In order to obtain a good approximation to $\partial S_{ij}/\partial d$, Δd must be small enough, yet to evaluate $S_{ij}(d+\Delta d)-S_{ij}(d-\Delta d)$ meaningfully, Δd must be large enough. Now if we consider S_{ij} to vary slowly with the distance, d, then this will relax the first condition somewhat. And, if we may consider many digits in the evaluation of S_{ij} to be significant, then we may meaningfully evaluate $S_{ij}(d+\Delta d)-S_{ij}(d-\Delta d)$ even for small values of Δd. But it is this latter constraint which makes it difficult to use finite difference approach to find sensitivity for parasitic coupling. Parasitic couplings are often a second order effect on circuit performance, so for reasonably small changes, Δd, it may be very difficult to accurately determine the resulting change in external port parameters. In essence, this is the computational equivalent of trying to measure a signal which is below the noise level of the measuring instrument. Thus any evaluation of sensitivity based on a finite-difference approach must carefully determine a proper choice for the perturbation (in this case Δd) and may only be carried out with confidence if the resulting function evaluations (in this case $S_{ij}(d+\Delta d)-S_{ij}(d-\Delta d)$) differ meaningfully. For this reason, an analytical approach to sensitivity analysis is preferred. Even so, application of the finite difference method may serve as a check when it can be used.

Such verification is reported in Tables 4.1 and 4.2. S-parameters for the Double U-bend were obtained for separation distances of 160.5 μm and 159.5 μm. Comparison was then made between the sensitivity determined using the finite difference approach and the value determined from the analytical method for $d = 160$ μm. Values are reported only for the first column of the four-port scattering matrix in Table 4.1. The sensitivities obtained by both methods are quite close — an indication that the sensitivity algorithms have been implemented correctly. This same procedure was carried out for the parallel coupled lines discussed in section 3.2.4. In this case, values are given for the discrete magnetic current distribution, and the data of Table 4.2 serves to validate the implementation of equation 4.28.

Table 4.1: Comparison of Sensitivities for Double U-bend Configuration

Type of Analysis	d	Real Part	Imaginary Part	Magnitude	Angle (deg)
S11	160.5	-.3801825956E-03	.2273271223E-01		
	159.5	-.3821649169E-03	.2272971522E-01		
Finite Difference		.0019823213E-03	.0000299701E-01	.35933E-05	56.52
Adjoint Network		.1982262779E-05	.2996949342E-05	.35932E-05	56.52
S21	160.5	.9987387666E+00	-.4429954068E-01		
	159.5	.9987368415E+00	-.4430241008E-01		
Finite Difference		.0000019251E+00	.0000286940E-01	.34554E-05	56.14
Adjoint Network		.1925020071E-05	.2869335456E-05	.34553E-05	56.14
S31	160.5	.2331270491E-03	-.9102425556E-02		
	159.5	.2334410332E-03	-.9205140809E-02		
Finite Difference		-.0003139841E-03	.0103715253E-02	.10372E-03	90.17
Adjoint Network		-.3140296762E-06	.1027142303E-03	.10271E-03	90.18
S41	160.5	-.1075592871E-02	-.8903516087E-02		
	159.5	-.1089925755E-02	-.9003661083E-02		
Finite Difference		.0014332884E-02	.0100144996E-02	.10117E-03	81.86
Adjoint Network		.1433269429E-04	.1001440076E-03	.10116E-03	81.86

Table 4.2: Comparison of Sensitivities for Parallel Coupled Lines

Type of Analysis	d	Real Part	Imaginary Part	Magnitude	Angle (deg)
S11	2100.5	.4161081756E-04	.2534585563E-02		
	2099.5	.4174274870E-04	.2534624366E-02		
Finite Difference		-.0013193114E-04	-.0000038803E-02	.13752E-06	-163.61
Adjoint Network		-.1319310875E-06	-.3880261845E-07	.13752E-06	-163.61
S21	2100.5	-.4384813008E-04	-.9960353308E+00		
	2099.5	-.4394140347E-04	-.9960352020E+00		
Finite Difference		.0009327339E-04	-.0000001288E+00	.15903E-06	-54.09
Adjoint Network		.9327336205E-07	-.1288000515E-06	.15903E-06	-54.09
S31	2100.5	-.1982069613E-02	.8414268831E-04		
	2099.5	-.1983608611E-02	.8411534615E-04		
Finite Difference		.0001538998E-02	.0002734226E-04	.15392E-05	1.02
Adjoint Network		.1538997408E-05	.2734215221E-07	.15392E-05	1.02
S41	2100.5	-.1013891143E-01	.1012875444E-03		
	2099.5	-.1015139701E-01	.1012837577E-03		
Finite Difference		.0001248558E-01	.0000037867E-03	.12486E-04	0.02
Adjoint Network		.1248558214E-04	.3786734432E-08	.12486E-04	0.02

CHAPTER 5

SENSITIVITY OF CIRCUIT PERFORMANCE TO PARASITIC COUPLING

In this chapter, the sub-circuit sensitivity developed in Chaper 4 is extended for complete circuit parameters. This is accomplished by deriving the sensitivity equation in terms of S-parameters and then implementing the same procedure for the case of a complete circuit. A few examples are included.

5.1 Sensitivity Equation in terms of S-parameters

In Section 4.1, the sensitivity equation was obtained in terms of voltages and currents by applying Tellegen's Theorem to three different networks. A corresponding form of Tellegen's Theorem may be written in terms of S-parameters provided corresponding ports of the original and adjoint networks are similarly normalized. Let

$$b = [S]\, a \tag{5.1}$$

and

$$\hat{b} = [\hat{S}]\, \hat{a} \tag{5.2}$$

for the networks N and $\hat{N}$ respectively. Then for any two networks, N and $\hat{N}$, having the same topology and similar port normalizations [19]

$$b^t \hat{a} - a^t \hat{b} = 0 \tag{5.3}$$

This form of Tellegen's Theorem may be used to obtain a sensitivity equation which is analogous to equation 4.27. In terms of S-parameters, we have

$$\hat{a}_p^t \, \Delta S_{ext} \, a_p = \hat{a}_q^t \, \Delta \, S_q a_q \tag{5.4}$$

In this expression, a_p and $\hat{a}_p$ are the incident wave variables at the external ports and ΔS_{ext} the desired external port sensitivities. The incident wave variables at the interconnection ports, a_q and $\hat{a}_q$, may be found from the excitations a_p and $\hat{a}_p$. This information is retained from the implementation of the segmentation procedure for S-parameters as described in Appendix A. We write,

$$a_q = [T_a] \, a_p \;\text{ and }\; \hat{a}_q = [\hat{T}_a] \, \hat{a}_p \tag{5.5}$$

In these expressions it should again be noted that $[T_a]$ and $[\hat{T}_a]$ need not be the same, and for a non-reciprocal network such as an ampifier, the two matrices must be obtained separately by applying the segmentation method to form both the original and adjoint networks. Once these are obtained, the complete circuit sensitivity may be found from the sub-circuit sensitivity in a manner completely analogous to equation 4.39. We get

$$\Delta S_{ext_{ij}} = (i^{th} \text{ row of } [\hat{T}_a]^t) \cdot [\Delta \, S_q] \cdot (j^{th} \text{ column of } [T_a]) \tag{5.6}$$

where ΔS_q is the sub-circuit sensitivity given in equation 4.41

5.2 Implementation

In equation 5.6 we have an expression for obtaining the desired circuit sensitivity. It has been formulated to provide the sensitivity to changes in parasitic coupling associated with a specified change in the layout of a selected sub-circuit. The analysis procedure for carrying out the sensitivity evaluation

is illustrated in Figure 5.1. The procedure assumes that several of the necessary precalculations have already been carried out. They are:

(a) the Z-matrices for individual components have been found

(b) Coupling port locations have been specified in terms of local coordinates for each component

(c) the S-parameters of the remaining network have been determined.

Each of these intermediate results is stored in a file which will be read by the sensitivity algorithm. Once these three items are in place, it is possible to perform the sensitivity analysis interactively. The algorithm reads in the Z-matrix for each component and from these forms the two matrices. One of these, Y_r, is a reduced matrix which retains only the external ports. It is used to find the S-parameters of the sub-circuit without coupling. The other matrix, Y, is the complete matrix formed for the combination of all components. It must be numbered such that external ports are at the top and coupling ports at the bottom of the matrix as required by the segmentation algorithm. Next, the coupling port positions for each component are read from a file, and the location and orientation of each local system specified. With this information the mutual admittance matrix is formed. From here, the segmentation method is used to combine matrix Y and the mutual admittance matrix yielding the Y-parameters of the sub-circuit with coupling. Matrix T_v, giving the interconnection voltages, is retained. To convert from Y-parameters to S-parameters, the port terminations are taken to be fifty ohms (unless specified otherwise). At this point the S-parameters for the sub-circuit both with and without coupling are available and are written to a file. If sub-circuit sensitivity is desired,

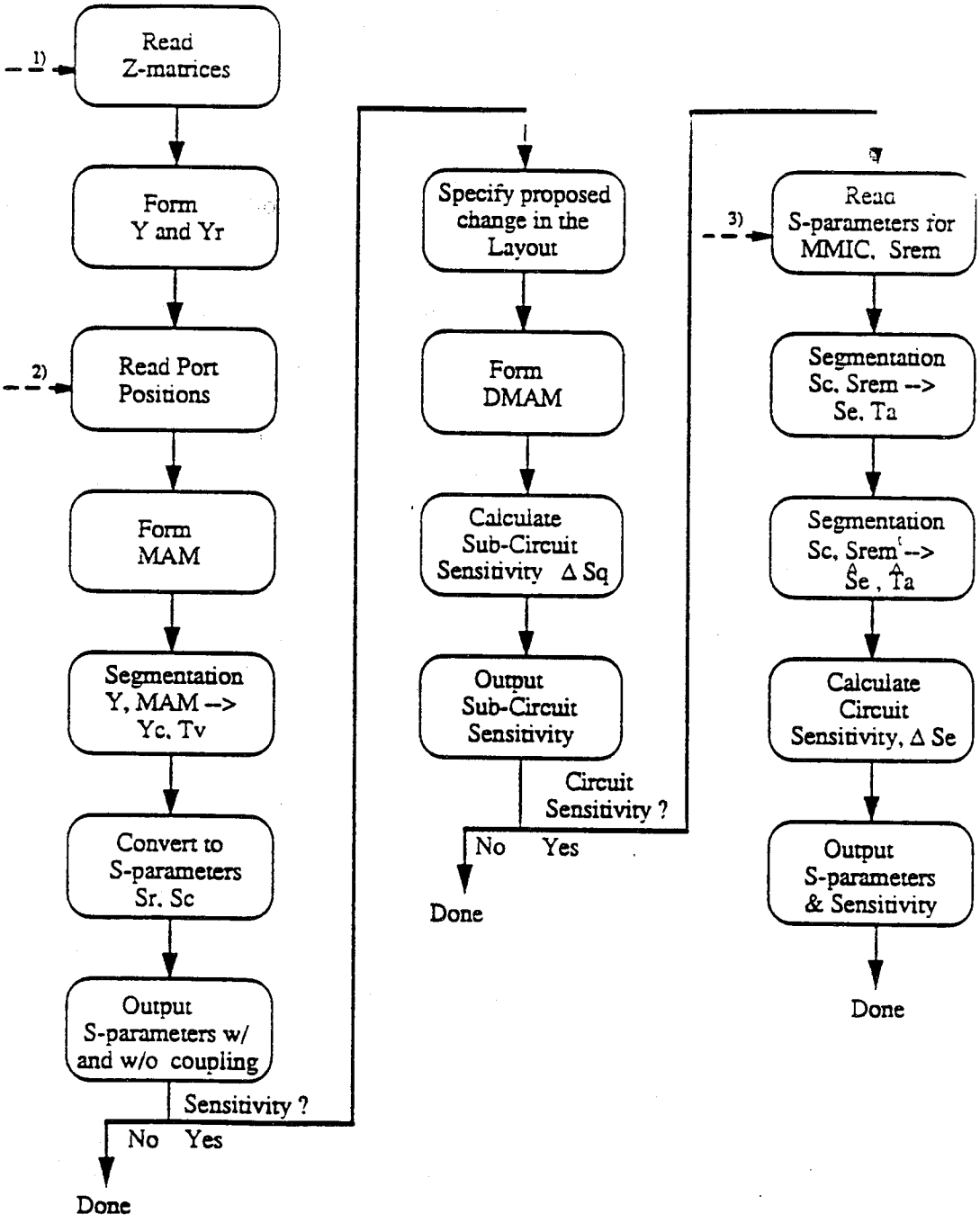

Figure 5.1: Numerical Implementation of Sensitivity Analysis

the program continues. By specifying a proposed change in the layout, the differential mutual admittance matrix can be formed; and from T_v and DMAM the sub-circuit sensitivity, ΔS_q, is found. If the sub-circuit is part of a larger network for which the S-parameters are known, then the overall circuit performance and sensitivity can be evaluated. The program reads in the S-parameters of the remaining circuit, S_{rem}, and by applying the segmentation method, S_{rem} and the sub-circuit S-parameters, S_c, are combined to yield the S-parameters of the complete circuit, S_e. Matrix T_a is retained for the sensitivity evaluation. The MMIC's S-parameters, S_{rem}, are not assumed to be reciprocal, hence the adjoint network is also formed. This is done by using segmentation to combine S_c and the transpose matrix S^t_{rem}. The reason for doing this is to obtain the matrix $\hat{T}_a$ needed for sensitivity calculations. The desired sensitivity matrix, ΔS_e, is then formed and written to the output file.

5.3 Full Circuit Sensitivities

The algorithm discussed in the previous section has been used to analyze several structures. Consider again the Double U-bend configuration discussed in sections 3.3 and 4.3. The finite difference approach has been used to find the circuit sensitivities for a change in the separation distance d. Table 5.1 summarizes the result. As before, this check serves to verify the implementation of the algorithms used to obtain circuit sensitivities. The values reported for the amplifier's S-parameters also correspond to those obtained by re-introducing the sub-circuit into the *Touchstone* analysis. This gives further confirmation of the segmentation procedure developed in terms of S-parameters. By repeating the sensitivity analysis for a number of frequencies from 5 to 6 GHz, a plot of the amplifier sensitivities is obtained. The

Table 5.1: Comparison of Sensitivities Found for the Single-Stage Amplifier

Type of Analysis	Real Part	Imaginary Part	Magnitude	Angle (deg)
S11				
Finite Difference	-.6938500000E-04	.6795200000E-04	.97117E-04	135.60
Adjoint Network	-.6938407623E-04	.6795102086E-04	.97116E-04	135.60
S21				
Finite Difference	-.2621900000E-03	.7970000000E-05	.26231E-03	178.26
Adjoint Network	-.2621874296E-03	.7973356434E-05	.26231E-03	178.26
S12				
Finite Difference	.2720080000E-04	.2835230000E-04	.39290E-04	46.19
Adjoint Network	.2720053459E-04	.2835198131E-04	.39290E-04	46.19
S22				
Finite Difference	-.7038700000E-05	.1263357000E-03	.12653E-03	93.19
Adjoint Network	-.7038799011E-05	.1263343795E-03	.12653E-03	93.19

results are shown in Figure 5.2, where the values are reported as $|\Delta S_{ij}|$ in dB. Plotting the results in this way provides a measure of the relative significance of certain couplings, and, although it is not intuitive what a sensitivity of, say -70 dB, means, it is clear from the plot that S_{21} is more sensitive to couplings between the two U-bends than S_{22}, for example. This reasoning applies to comparison of the circuit sensitivity to couplings in different sub-circuits as well. Consider the line-to-viahole coupling of region B in Figure 3.14. A sensitivity evaluation has been carried out for this sub-circuit and results are given in Figure 5.3. By comparison, it is evident that circuit parameters are much less sensitive to couplings within sub-circuit B than sub-circuit A.

A second amplifier was also studied, and sensitivity analysis performed for a selected sub-circuit. The distributed MESFET amplifier of this example is shown in Figure 5.4. In this example, there are many parallel coupled line sections for which couplings have been included. To get an idea how significant these couplings might be to circuit performance, all these couplings have been excluded and the amplifier performance analysis conducted without these couplings. This is shown in Figure 5.5, trace number 1. The analysis with these couplings included is given by trace number 2. To tell which of the coupled-line sections contributes most significantly to the change in amplifier performance, different sections could be selected for sensitivity analysis. For closely coupled lines which may be accurately modeled using quasi-static methods, it is possible to use the finite difference method to obtain the sub-circuit sensitivity for coupled line sections. To illustrate, the enclosed three-coupled-line section in Figure 5.4 was chosen. The sub-circuit sensitivity for this region was obtained using the finite difference approach with the *Touchstone* analysis

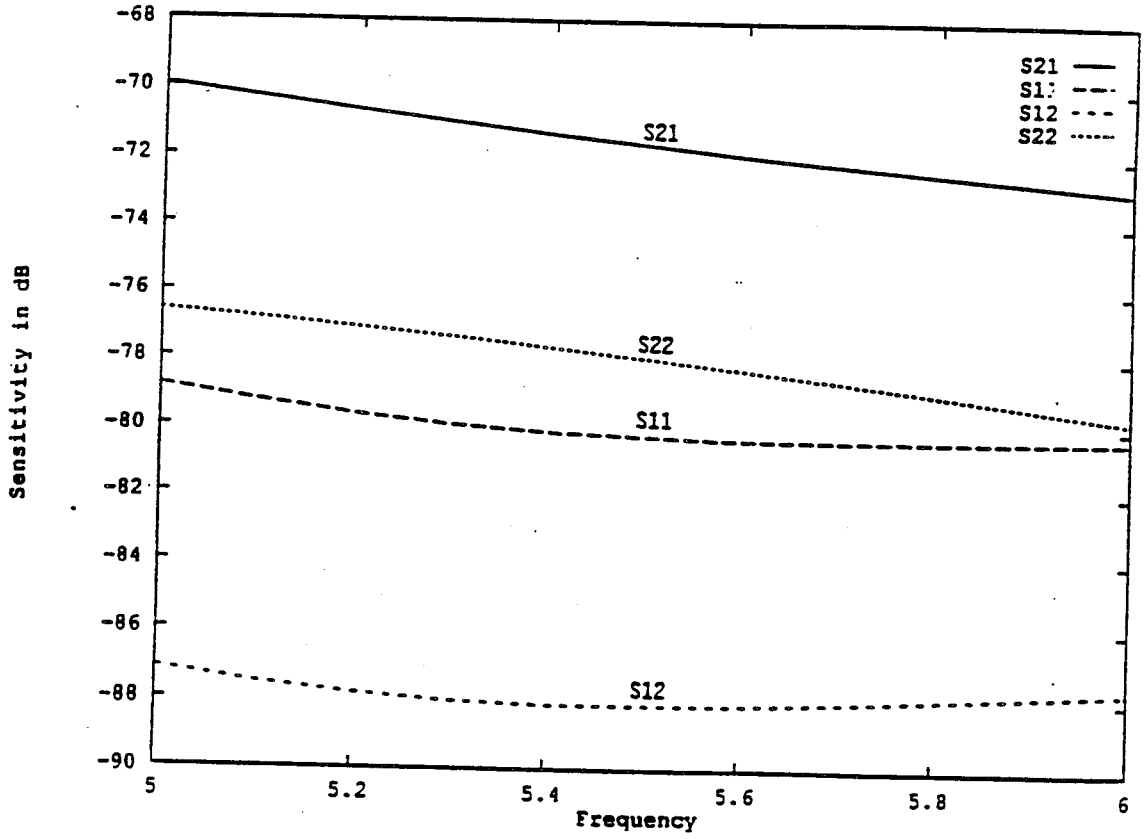

Figure 5.2: Amplifier Sensitivity Analysis for Double U-bend Configuration

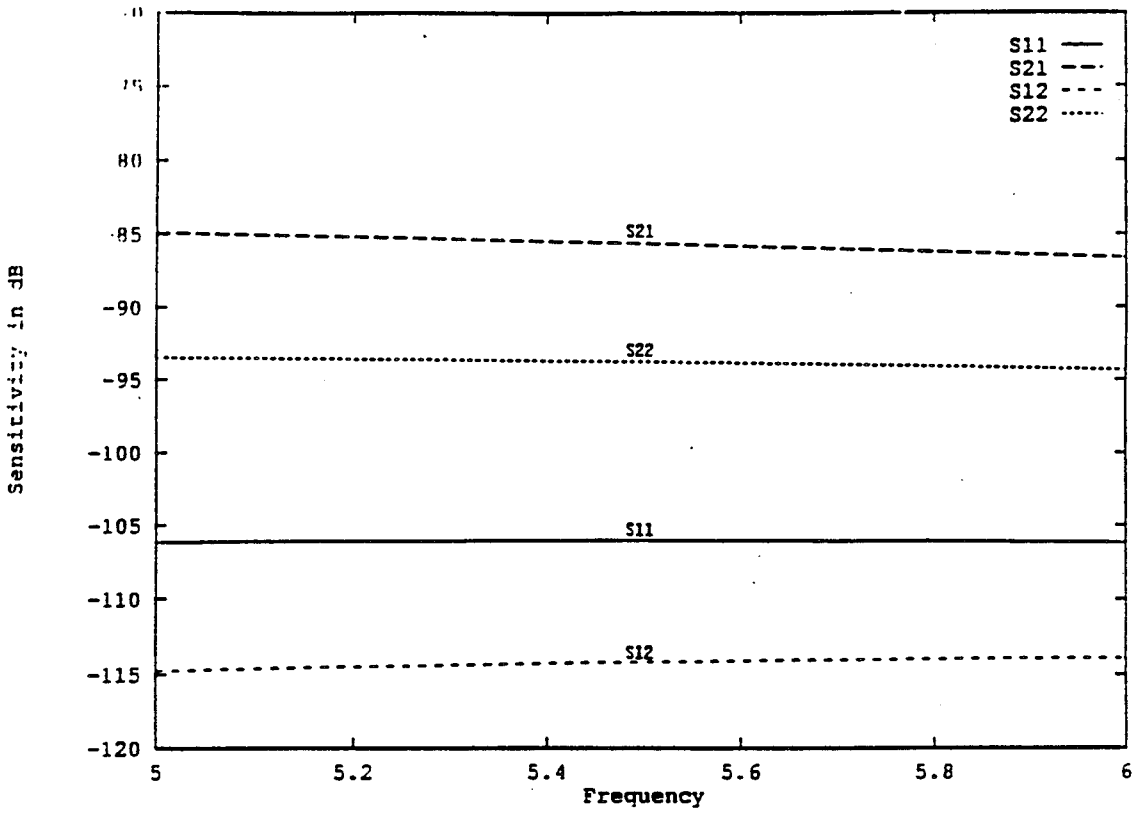

Figure 5.3: Amplifier Sensitivity Analysis for Line-to-Viahole Coupling

for an asymmetric three-coupled-line section. By introducing this sensitivity into the final steps of the algorithm developed in this research, sensitivity for the complete amplifier of Figure 5.6 was obtained. This serves to show that the adjoint network method may be employed for circuit sensitivities even when other methods are used to obtain sensitivities for a selected sub-circuit. By repeating this type of analysis for different regions of the distributed amplifier it would be possible to determine the relative effect the parasitic couplings of these different regions have on amplifier performance.

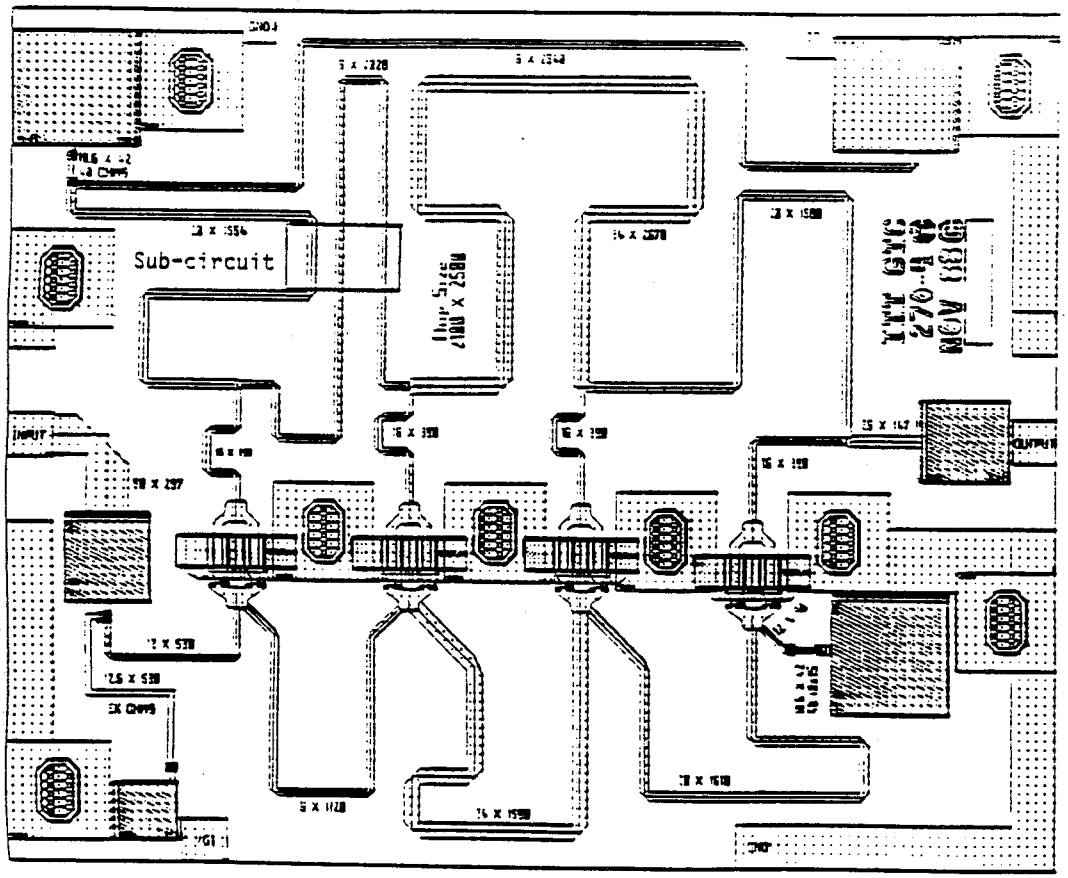

(Courtesy of ITT)

Figure 5.4: Parasitic Couplings in a MESFET Amplifier

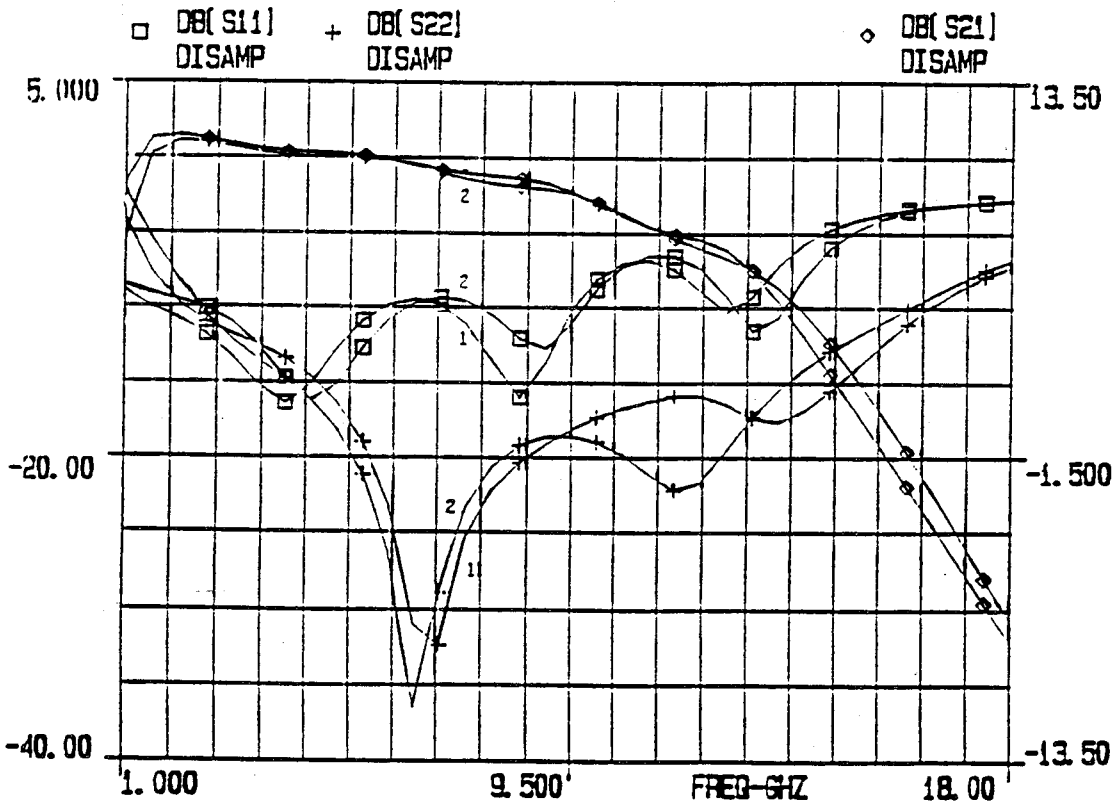

Figure 5.5: Amplifier Performance with and without Couplings Included

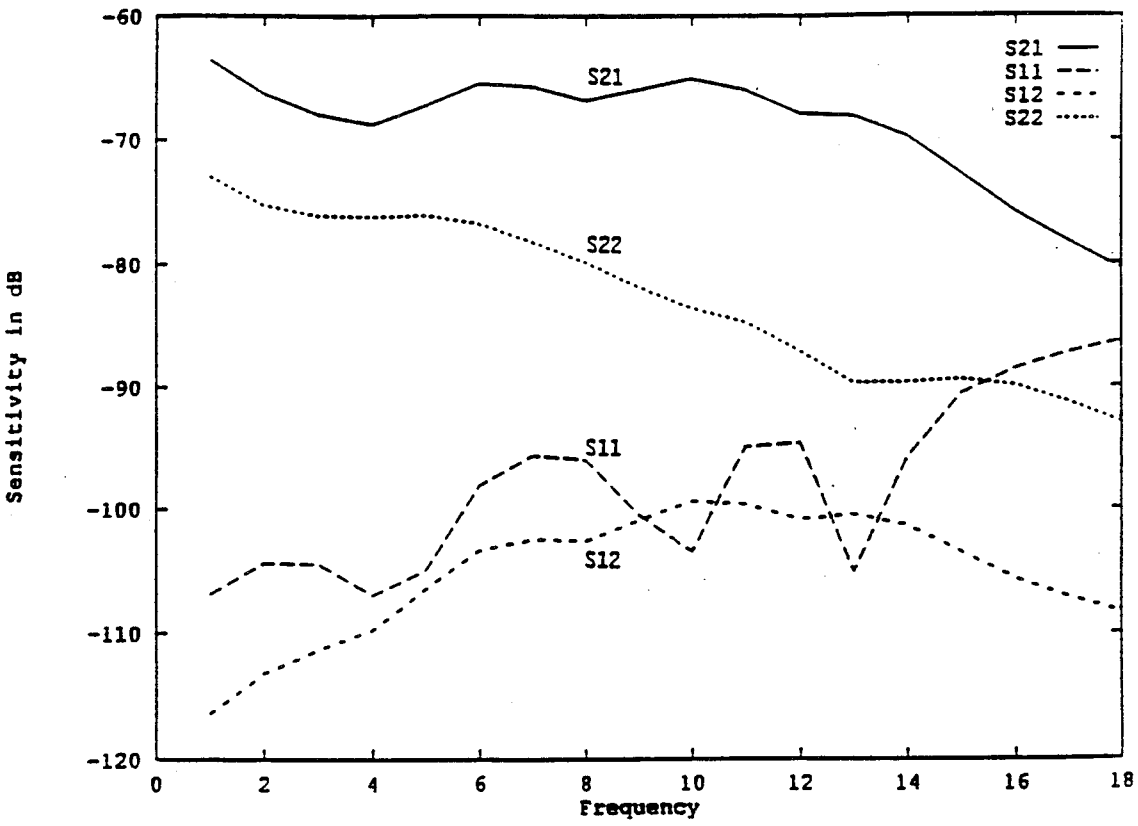

Figure 5.6: Amplifier Sensitivity Analysis for Three-Coupled-Lines

CHAPTER 6

CONCLUDING REMARKS

The planar waveguide model and MNM approach have been used to develop an algorithm for incorporating parasitic couplings in microstrip circuit analysis. The adjoint network method has also been used with this model to provide sensitivity analysis for parasitic coupling. The methods proposed have been generalized to make them applicable to a complete MMIC layout.

6.1 Sensitivity Equation in terms of S-parameters

Planar analysis is appropriate for microstrip structures when the substrate is electrically thin. For regular segments analytical series expressions are available which correctly describe the field configuration within the planar waveguide. Numerical evaluation of the impedance characterization for these segments introduces some inaccuracy because infinite series expressions are truncated. By taking a sufficiently large number of terms, this numerical error can be minimized. Circuit components which can be subdivided into regular segments may be analyzed using the segmentation method. The segmentation procedure matches the fields at a number of ports along the common edge of two planar segments. This can cause some discretization error, but a proper choice for the number of interconnection ports keeps this error small. An analogous method known as desegmentation may be applied to components which can be formed by removing one regular segment from another. Since the numerical and discretization error in these methods can be kept small, the

accuracy of the planar model depends primarily on a proper determination of the effictive dimensions. In this report, a planar model for microstrip viahole grounds is presented. Difficulty in finding the proper effective dimensions for large viahole pads (relative to the substrate height) and for large post diameters (relative to the pad width) limits the use of the present model to cases where the post diameter is close to one third of the pad width.

6.2 Parasitic Coupling

To account for radiation loss and parasitic couplings, the planar modeling approach must be enhanced to permit power flow into and out of the otherwise closed waveguide. A multiport network approach (MNM) was developed for this purpose. It calls for placement of a number of coupling ports along the edges of a planar component. A multiport network is then added to model the external field effects. In order to account for the fields external to the planar waveguide, Shelkunoff's equivalence theorem is applied to the microstrip structure and equivalent magnetic currents found which are then used to determine the field configuration above the microstrip structure. The magnetic current distribution given by the equivalence theorem is determined from the electric field tangential to the air-dielectric interface. The total magnetic current is determined by the edge voltage. Because the tangential electric field for a planar component decays rapidly away from the edge, a single magnetic current element may be used to approximate the continuous distribution. It is also possible to truncate the magnetic current distribution, in which case the currents should be normalized to give the same total current. This report includes a procedure for representing a continuous current distribution by a finite number of discrete elements. For the current distribution chosen it is

possible to develop a network model representing the interaction between the coupling ports of two components. Radiation loss coupling among sections of the same component may be accounted for by the generalized self-admittance network. From these models the mutual admittance matrix representing the multiport network as required by the MNM approach is obtained.

6.3 Sensitivity Analysis

Because the MNM approach uses a network model, it is possible to perform sensitivity analysis using network methods. By using the adjoint network method it is possible to obtain a sensitivity equation which expresses the sensitivity of a network's external port parameters to changes in a connected sub-network. Application of this procedure to parasitic coupling and the MNM approach requires the determination of the differential mutual admittance matrix. This, in turn, requires knowledge of how the mutual admittance of two ports is affected by changes in their relative location, as well as how each coupling port will move relative to the other coupling ports. By differentiation of the expression for the two-port mutual admittance and from geometrical considerations it is possible to determine each term of the differential mutual admittance matrix. By introducing the DMAM into the sensitivity equation, sensitivities are obtained for the selected sub-circuit. This procedure is repeated in terms of scattering parameters to the sensitivities for a larger network.

6.4 Analysis of MMIC's

Most often, it is not necessary or appropriate to apply electromagnetic simulation to a complete MMIC layout. Usually, only portions of the circuit

require this effort. This report describes a methodology for incorporating parasitic coupling effects into circuit analysis and performing the corresponding sensitivity analysis. The algorithms have been tailored to specifically address the need for modeling of spurious radiation and parasitic coupling in MMIC's. In particular, sensitivity analysis may be used to determine which couplings create problems for the designer. It is recommended that in such regions a more careful analysis be performed. If coupling poses a significant problem in a given sub-circuit it may be necessary to alter the design. This might be done either by compensating for the coupling effects or changing the layout to reduce the impact coupling has on the circuit performance. In the latter case the analysis presented could be particularly helpful. Since it is possible to quickly analyze a subcircuit whose components have been reconfigured the designer can quickly determine if certain changes in a selected sub-circuit will significantly reduce couplings or not.

In short, algorithms have been developed using these methods and testing of the procedures carried out for several examples. In the future, an effort could be made to extend these methods for microstrip circuits enclosed by packaging, and more testing done in order to determine the coupling predicted by these methods for a wide range of microstrip structures.

BIBLIOGRAPHY

[1] L. Lewin, "Radiation from Discontinuities in Stripline", **Proc. Inst. Elec. Eng.** , Vol. 117,pt. C, pp. 103-170, Sept. 1960.

[2] L. Lewin,"Spurious Radiation from a Microstrip Y-Junction", **IEEE Trans.**, Vol. **MTT**-26, Nov. 1978

[3] M.D. Abouzahra,"On the Radiation from Microstrip Discontinuities",**IEEE Trans.**, Vol. **MTT**-29, July 1981

[4] D.C. Chang, J.X. Zheng,"Electromagnetic Modeling of Passive Circuit Elements in MMIC. Part I: The P-mesh algorithm. Part II: Effect of Circuit Discontinuities and Mutual Coupling in Microstrip Circuits", submitted to **IEEE Trans. Microwave Theory and Techniques**, June 1990, to be published

[5] A. Benalla, K.C. Gupta, "Multiport Network Model and Transmission Characteristics of Two-Port Rectangular Microstrip Patch Antennas", **IEEE Trans.**, Vol. **AP**-36, No. 10, Oct. 1988

[6] A. Benalla, K.C. Gupta, "Multiport Network Approach for Modeling the Mutual Coupling Effects in Microstrip Patch Antennas and Arrays", **IEEE Trans.**, Vol. **AP**-37, No. 2, Feb. 1989

[7] A. Sabban," Multiport Network Model for Evaluating Radiation Loss and Spurious Coupling among Discontinuities in Microstrip Circuits", **MIM-ICAD Technical Report No. 6**, based on Ph.D. thesis, Jan. 1991.

[8] A. Sabban, K.C. Gupta, "Characterization of Radiation Loss from Microstrip Discontinuities Using a Multiport Network Modeling Approach", **IEEE Trans.**, Vol. **MTT**-39, No. 4, April 1991

[9] H.A. Wheeler, "Transmission-line properties of parallel strips separated by a dielectric sheet," **IEEE Trans.**, Vol. **MTT**-24, pp. 195-200, 1976.

[10] E.O. Hammerstad, O. Jensen, "Accurate Models for Microstrip Computer Aided Design", **IEEE MTT-S International Microwave Symposium Digest**, 1980, pp. 407-409

[11] M.V. Schneider, "Microstrip lines for microwave integrated circuits," **Bell System Technical Journal**, Vol. 48 May-June 1969, pp. 1421-1444.

[12] W.J. Getsinger, "Microstrip dispersion model," **IEEE Trans.**, Vol. **MTT**-21, No. 1,1973, pp. 34-39

[13] T. Okoshi, "Planar Circuits for Microwaves and lightwaves," **Springer–Verlag**, New York, 1985

[14] H. Maramis, "Planar Model Characterization of Compensated Microstrip Bends," **M.S. Thesis**, Dept. of Electrical and Computer Engineering, Univ. of Colorado, Dec. 1988.

[15] G. Kompa, R. Mehran, "Planar Waveguide Model for Calculating Microstrip Components," **Electronics Letters**, Vol. 11, Sept. 1975, pp. 459–460.

[16] I. Wolff, G. Kompa, R. Mehran, "Calculation Method for Microstrip Discontinuities and T-Junctions," **Electronics Letters**, Vol. 8, No. 7, April 1972, pp. 177–179.

[17] W. Menzel, I. Wolff, "A Method for Calculating the Frequency-Dependent Properties of Microstrip Discontinuities", **IEEE Trans.**, Vol. **MTT**-25, No. 2, Feb. 1977

[18] T. Chu, T. Itoh, "Analysis of Microstrip Step Discontinuity by the Modified Residue Calculus Technique", **IEEE Trans.**, Vol. **MTT**-33, No. 10, Oct. 1985

[19] K.C. Gupta, R Garg, R. Chadha, **Computer-Aided Design of Microwave Circuits**, Artech House Inc., 1981

[20] P.C. Sharma, K.C. Gupta, "Desegmentation Method for Analysis of Two-Dimensional Microwave Circuits", **IEEE Trans.**, Vol. **MTT**-29, No. 10, Oct. 1981

[21] A. Benalla, K.C. Gupta, "Faster Computation of Z-Matrices for Rectangular Segments in Planar Microstrip Circuits", **IEEE Trans.**, Vol. **MTT**-34, No. 6, June 1986

[22] M.E. Goldfarb, R.A. Pucel, "Modeling Via Hole Grounds in Microstrip", **IEEE Microwave and Guided Wave Letters**, Vol. 1, No. 6, June 1991

[23] K.L. Finch, N.G. Alexopoulos, "Shunt Posts in Microstrip Transmission

Lines", **IEEE Trans.**, Vol. **MTT**-38, No. 11, Nov. 1990

[24] Carl T.A. Johnk, **Engineering Electromagnetic Fields and Waves**, Second Edition, John Wiley and Sons, 1988, Ch. 7, pp. 399-403.

[25] J.R. James, P.S. Hall, C. Wood, **Microstrip Antenna Theory and Design**, Peter Peregrinus Ltd., UK, 1981, Ch. 4, pp. 87-93.

[26] T.M. Martinson,"Edge Field Analysis of Arbitrarily Shaped Microstrip Patch Antennas", Ph.D. Thesis, Dept. of Electrical and Computer Engineering, University of Colorado, 1988.

[27] L.O. Chua, P. Lin, **Computer-Aided Analysis of Electronic Circuits: Algorithms and Computational Techniques**, Prentice-Hall, Inc., New Jersey, Ch. 3, pp. 134-135.

[28] L.O. Chua, P. Lin, **Computer-Aided Analysis of Electronic Circuits: Algorithms and Computational Techniques**, Prentice-Hall, Inc., New Jersey, Ch. 15, pp. 579-604.

[29] I.S. Gradshteyn, I.M. Ryzhik, **Table of Integrals, Series, and Products**, Academic Press, New York, 1980, pp. 40-41.

APPENDIX A

SEGMENTATION METHODS FOR ADMITTANCE AND SCATTERING PARAMETERS

A.1 Segmentation Procedure in terms of Admittance Matrices

Consider the components of Figure A.1 below. The segmentation method seeks to combine the network characterizations of components A and B to obtain the network characteriztion for the component C. In terms of the Y-parameter characterization, we have:

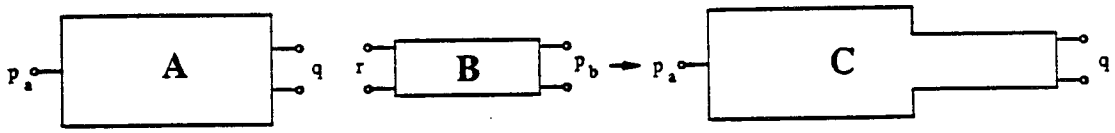

Figure A.1: Network Representation Used in Segmentation Method

$$I_A = Y_A V_A \qquad I_B = Y_B V_B \tag{A.1}$$

where

$$I_A = \begin{bmatrix} I_{p_a} \\ I_q \end{bmatrix}, \quad V_A = \begin{bmatrix} V_{p_a} \\ V_q \end{bmatrix}, \quad I_B = \begin{bmatrix} I_{p_b} \\ I_r \end{bmatrix}, \quad \text{and} \quad V_B = \begin{bmatrix} V_{p_b} \\ V_r \end{bmatrix} \tag{A.2}$$

So,

$$\begin{bmatrix} I_{p_a} \\ I_q \end{bmatrix} = \begin{bmatrix} Y_{p_a} & Y_{p_aq} \\ Y_{qp_a} & Y_{qp} \end{bmatrix} \begin{bmatrix} V_{p_a} \\ V_q \end{bmatrix} \quad \text{and} \quad \begin{bmatrix} I_{p_b} \\ I_r \end{bmatrix} = \begin{bmatrix} Y_{p_b} & Y_{p_br} \\ Y_{rp_b} & Y_{rr} \end{bmatrix} \begin{bmatrix} V_{p_b} \\ V_r \end{bmatrix} \tag{A.3}$$

Taking

$$I_p = \begin{bmatrix} I_{p_a} \\ I_{p_b} \end{bmatrix} \quad \text{and} \quad V_p = \begin{bmatrix} V_{p_a} \\ V_{p_b} \end{bmatrix} \tag{A.4}$$

we write equation A.3 as

$$\begin{bmatrix} I_p \\ I_q \\ I_r \end{bmatrix} = \begin{bmatrix} Y_{pp} & Y_{pq} & Y_{pr} \\ Y_{qp} & Y_{qq} & \mathbf{0} \\ Y_{rp} & \mathbf{0} & Y_{rr} \end{bmatrix} \begin{bmatrix} V_p \\ V_q \\ V_r \end{bmatrix} \tag{A.5}$$

where

$$Y_{pp} = \begin{bmatrix} Y_{p_a} & 0 \\ 0 & Y_{p_b} \end{bmatrix}, \quad Y_{pq} = \begin{bmatrix} Y_{p_aq} \\ 0 \end{bmatrix}, \quad Y_{pr} = \begin{bmatrix} 0 \\ Y_{p_br} \end{bmatrix} \tag{A.6}$$

and

$$Y_{qp} = Y_{pq}^t = [Y_{qp_a}\,,\, 0] \text{ and } Y_{rp} = Y_{rp}^t = [0\,,\, Y_{rp_b}]. \tag{A.7}$$

From equation A.5, we may write

$$I_p = Y_{pp}V_p + Y_{pq}V_q + Y_{pr}V_r \tag{A.8}$$

$$I_q = Y_{qp}V_p + Y_{qq}V_q \tag{A.9}$$

$$I_r = Y_{rp}V_p + Y_{rr}V_r \tag{A.10}$$

To obtain the external port currents, I_p, in terms of the excitation V_p, and the interconnection voltages V_r in terms of V_p, the conditions

$$I_r = -I_q \tag{A.11}$$

and

$$V_r = V_q \tag{A.12}$$

are applied to equations A.8 - A.10 as follows. Introducing equation A.11 into equations A.9 and A.10 gives

$$(Y_{qp}V_p + Y_{qq}V_q) = -(Y_{rp}V_p + Y_{rr}V_r) \tag{A.13}$$

or

$$(Y_{qp} - Y_{rp})V_p = -Y_{rr}V_r - Y_{qq}V_q \tag{A.14}$$

which with equation A.12 may be written as

$$(Y_{qq} + Y_{rr})V_q = (Y_{rp} - Y_{qp})V_p \tag{A.15}$$

so,

$$V_q = (Y_{qq} + Y_{rr})^{-1}(Y_{rp} - Y_{qp})V_p \tag{A.16}$$

which is one of the desired results. We go on to consider equation A.8 making use of equation A.12 and A.16, giving

$$I_p = Y_{pp}V_p + (Y_{pq} + Y_{pr})(Y_{qq} + Y_{rr})^{-1}(Y_{rp} - Y_{qp})V_p \tag{A.17}$$

or,

$$I_p = [Y_{pp} + (Y_{pq} + Y_{pr})(Y_{qq} + Y_{rr})^{-1}(Y_{rp} - Y_{qp})]V_p \tag{A.18}$$

So, the resultant matrix for component C is given by

$$Y_c = Y_{pp} + (Y_{pq} + Y_{pr})(Y_{qq} + Y_{rr})^{-1}(Y_{rp} - Y_{qp}) \tag{A.19}$$

A.2 Segmentation Procedure in terms of Scattering Parameters

Consider the components of Figure A.1 once again. In this case, the components will be characterized by their S-parameters rather than admittance matrix and consequently the derivation will involve wave variables rather than currents and voltages. For this characterization, we have

$$b_A = [S_A]a_A \quad \text{and} \quad b_B = [S_B]a_B \tag{A.20}$$

where

$$b_A = \begin{bmatrix} b_{p_a} \\ b_q \end{bmatrix}, \quad a_A = \begin{bmatrix} a_{p_b} \\ a_q \end{bmatrix}, \quad b_B = \begin{bmatrix} b_{p_b} \\ b_r \end{bmatrix}, \quad \text{and} \quad a_B = \begin{bmatrix} a_{p_b} \\ a_r \end{bmatrix} \tag{A.21}$$

So,

$$\begin{bmatrix} b_{p_a} \\ b_q \end{bmatrix} = \begin{bmatrix} S_{p_a} & S_{p_aq} \\ S_{qp_a} & S_{qq} \end{bmatrix} \begin{bmatrix} a_{p_a} \\ a_q \end{bmatrix} \quad \text{and} \quad \begin{bmatrix} b_{p_b} \\ b_r \end{bmatrix} = \begin{bmatrix} S_{p_b} & S_{p_br} \\ S_{rp_b} & S_{rr} \end{bmatrix} \begin{bmatrix} a_{p_b} \\ a_r \end{bmatrix} \tag{A.22}$$

Taking

$$b_p = \begin{bmatrix} b_{p_a} \\ b_{p_b} \end{bmatrix} \quad \text{and} \quad a_p = \begin{bmatrix} a_{p_a} \\ a_{p_b} \end{bmatrix} \tag{A.23}$$

we write equation A.22 as

$$\begin{bmatrix} b_p \\ b_q \\ b_r \end{bmatrix} = \begin{bmatrix} S_{pp} & S_{pq} & S_{pr} \\ S_{qp} & S_{qq} & \mathbf{0} \\ S_{rp} & \mathbf{0} & S_{rr} \end{bmatrix} \begin{bmatrix} a_p \\ a_q \\ a_r \end{bmatrix} \tag{A.24}$$

where

$$S_{pp} = \begin{bmatrix} S_{p_a} & 0 \\ 0 & S_{p_b} \end{bmatrix}, \quad S_{pq} = \begin{bmatrix} S_{p_aq} \\ 0 \end{bmatrix}, \quad S_{pr} = \begin{bmatrix} 0 \\ S_{p_br} \end{bmatrix} \tag{A.25}$$

and

$$S_{qp} = S^t_{pq} = [S_{qp_a}\,,\,0], \quad S_{rp} = S^t_{rp} = [0\,,\,S_{rp_b}]. \tag{A.26}$$

From equation A.24, we may write

$$b_p = S_{pp}a_p + S_{pq}a_q + S_{pr}a_r \tag{A.27}$$

$$b_q = S_{qp}a_p + S_{qq}a_q \tag{A.28}$$

$$b_r = S_{rp}a_p + S_{rr}a_r \tag{A.29}$$

In this case, the excitation will be the incident wave at the external ports, or a_p. Thus we desire to obtain the outgoing wave variable b_p in terms of a_p. The interconnection conditions in the case of S-parameters differ in form from the previous example. It is assumed that connected ports have been referenced to the same impedance such that

$$a_r = b_q \tag{A.30}$$

and

$$b_r = a_q \tag{A.31}$$

Introducing equations A.30 and A.28 into equation A.29 gives

$$b_r = S_{rp}a_p + S_{rr}(S_{qp}a_q + S_{qq}a_q) \tag{A.32}$$

or,

$$b_r = (S_{rp} + S_{rr}S_{qp})a_p + S_{rr}S_{qq}a_q \tag{A.33}$$

which, with equation A.31 may be written as

$$(I - S_{rr}S_{qq})a_q = (S_{rp} + S_{rr}S_{qp})a_p \tag{A.34}$$

so,

$$a_q = (I - S_{rr}S_{qq})^{-1}(S_{rp} + S_{rr}S_{qp})a_p \tag{A.35}$$

where $[I]$ is the identity matrix. Introducing equations A.31 and A.29 into equation A.28 gives

$$b_q = S_{qp}a_p + S_{qq}(S_{rp}a_p + S_{rr}a_r) \tag{A.36}$$

or,

$$b_q = (S_{qp} + S_{qq}S_{rp})a_p + S_{qq}S_{rr}a_r \tag{A.37}$$

which with equation A.30 may be written as

$$(I - S_{qq}S_{rr})a_r = (S_{qp} + S_{qq}S_{rp})a_p \tag{A.38}$$

so,

$$a_r = (I - S_{qq}S_{rr})^{-1}(S_{qp} + S_{qq}S_{rp})a_p \tag{A.39}$$

Now, using equations A.35 and A.39 in equation A.27, we write

$$\begin{aligned} b_p = S_{pp}a_p + S_{pq}(I - S_{rr}S_{qq})^{-1}(S_{rp} + S_{rr}S_{qp})a_p \\ +S_{pr}(I - S_{qq}S_{rr})^{-1}(S_{qp} + S_{qq}S_{rp})a_p \end{aligned} \tag{A.40}$$

So, the resultant matrix for component C is given by

$$\begin{aligned} S_C = S_{pp} + S_{pq}(I - S_{rr}S_{qq})^{-1}(S_{rp} + S_{rr}S_{qp}) \\ +S_{pr}(I - S_{qq}S_{rr})^{-1}(S_{qp} + S_{qq}S_{rp}) \end{aligned} \tag{A.41}$$

APPENDIX B

EXTENSION OF THE SINGLE-SERIES EXPRESSION FOR RECTANGULAR SEGMENTS

Formerly the available formulation of Z-matrices for rectangular segments in planar microstrip circuits required numerical summation of the doubly infinite series in the corresponding Green's function. Faster computation of the Z-matrices has been made available using a formulation based on analytical treatment of one of the summations [21]. This formulation is, however, limited to the special cases of vertical and horizontal port orientations. In the following treatment, the same approach used for these special cases will be applied to obtain expressions for arbitrary port positions.

To begin, consider the Green's function for a rectangular planar segment. It may be written [19],

$$\begin{aligned} G(x_i, y_i | x_j, y_j) &= \frac{j\omega\mu h}{ab} \sum_{n=0}^{\infty} \sum_{m=0}^{\infty} \left(\frac{\sigma_n \sigma_m}{k_x^2 + k_y^2 - k^2} \right) \\ &\quad \cdot \cos(k_x x_i) \cos(k_x x_j) \cos(k_y y_i) \cos(k_y y_j) \end{aligned} \tag{B.1}$$

where $k^2 = \omega\mu\epsilon$,

$$k_x = \frac{m\pi}{a}, \quad k_y = \frac{n\pi}{b}, \quad \text{and} \quad \sigma_{m,n} = \begin{cases} 1 & m, n = 0 \\ 2 & m, n \neq 0 \end{cases}$$

Here, a, b, h, μ, and ϵ refer to the microstrip segment shown in Figure B.1, so a is the length, b the width, h the substrate height, μ is taken as μ_o, and ϵ is the complex permitivity ϵ_c defined in equation 2.3. The elements of the

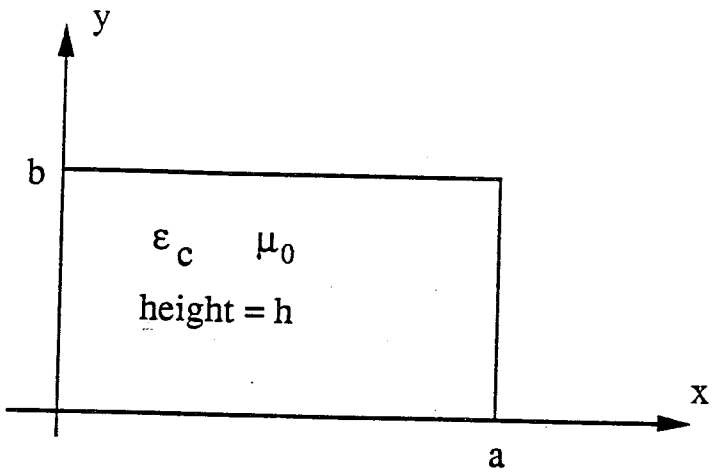

Figure B.1: Rectangular Planar Segment

Z-matrix are obtained from equation B.1 for two linear ports p and q and may be expressed as

$$Z_{pq} = \frac{1}{w_p w_q} \int_{w_q} \int_{w_p} G(x_i, y_i | x_j, y_j)\, dr_p\, dr_q \tag{B.2}$$

where dr_p and dr_q are the incremental distances along the port widths w_p and w_q.

The basic technique used to reduce equation B.2 to a SS form is to carry out one of the summations in equation B.1 analytically to obtain a SS form for the Green's function, reverse the order of the summation and integration in equation B.2, and then carry out the integration across ports p and q to obtain the desired expression for Z_{pq}. The crux of the matter is separating the variables of integration making it possible to complete this final step. For the DS form of the Green's function there is no difficulty in separating the variables and performing the integration by treating the double integral as the product of two integrations. Transforming the Green's function to a SS form requires us to treat special cases differently with respect to separating the variables of integration, however.

It is also possible to carry out the summation over either m or n analytically which introduces additional cases which must be considered. Taking the length a to be at least as large as the width b, convergence will be as fast or faster if we choose to sum over m analytically rather than n. In any case, should it be necessary to sum over n, we may do so without re-deriving all the expressions obtained from analytical summation over m. It suffices to transform the variables in a manner corresponding to a re-orientation of the rectangular segment as shown in Figure B.2. Thus we consider only those cases necessary for complete treatment with analytical summation over m.

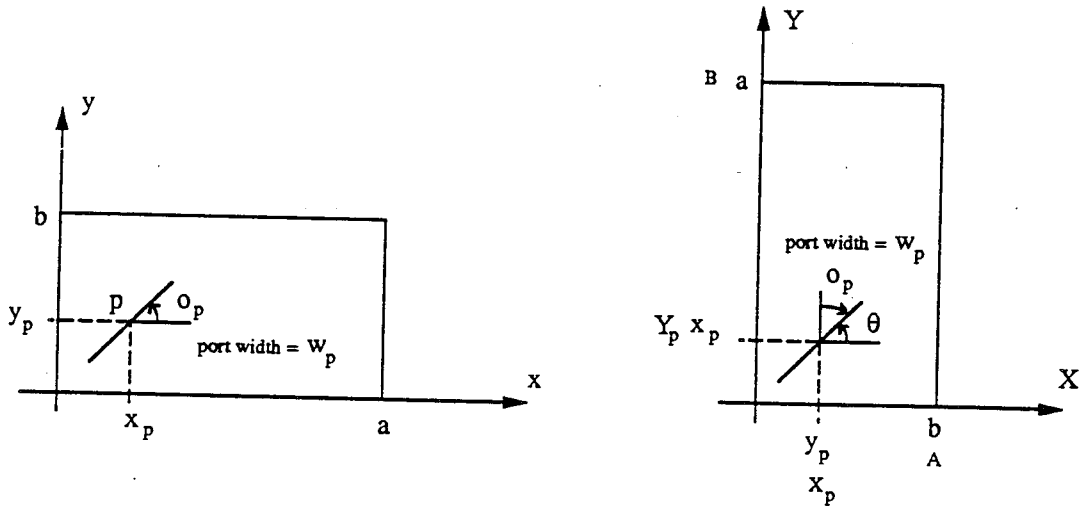

Figure B.2: Re-Orientation for Summation over n

B.1 Double Series Expression for Arbitrary Port Positions

Before going on, let's consider the DS form for any arbitrary port position. We have for the variables defined in Figure B.3,

$$Z_{pq} = \frac{j\omega\mu h}{ab}\sum_{n=0}^{\infty}\sum_{m=0}^{\infty}\left(\frac{\sigma_n\sigma_m}{k_x^2+k_y^2-k^2}\right) \cdot \left[\frac{1}{w_p}\int_{w_p}\cos(k_x x_i)\cos(k_y y_i)\,dr_p\right]\cdot\left[\frac{1}{w_q}\int_{w_q}\cos(k_x x_j)\cos(k_y y_j)\,dr_q\right] \tag{B.3}$$

By parameterizing the path for ports p and q, we may evaluate the integrals

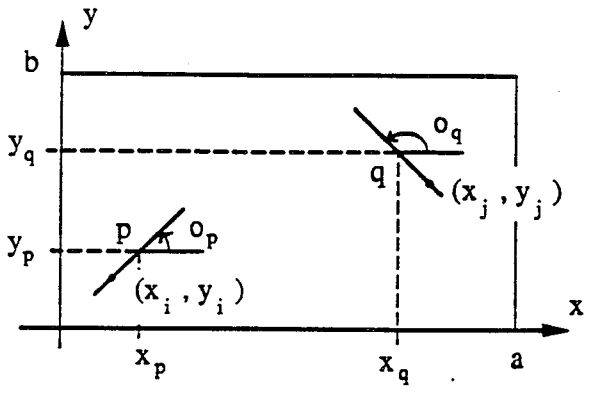

Figure B.3: Variable Definitions for Location of Ports p and q

in equation B.3 with the result,

$$Z_{pq} = \frac{j\omega\mu h}{ab}\sum_{n=0}^{\infty}\sum_{m=0}^{\infty}\left(\frac{\sigma_n\sigma_m}{k_x^2+k_y^2-k^2}\right)$$
$$\cdot\frac{1}{2}\left\{\cos[k_x x_p + k_y y_p]\,\mathrm{sinc}[k_x\tfrac{w_{px}}{2} + k_y\tfrac{w_{py}}{2}] + \cos[k_x x_p - k_y y_p]\,\mathrm{sinc}[k_x\tfrac{w_{px}}{2} - k_y\tfrac{w_{py}}{2}]\right\}$$
$$\cdot\frac{1}{2}\left\{\cos[k_x x_q + k_y y_q]\,\mathrm{sinc}[k_x\tfrac{w_{qx}}{2} + k_y\tfrac{w_{qy}}{2}] + \cos[k_x x_q - k_y y_q]\,\mathrm{sinc}[k_x\tfrac{w_{qx}}{2} - k_y\tfrac{w_{qy}}{2}]\right\}$$

where $\mathrm{sinc}(z)=\sin(z)/z$, and $w_{px}=w_p\cos(o_p)$, $w_{py}=w_p\sin(o_p)$, $w_{qx}=w_q\cos(o_q)$, and $w_{qy}=w_q\cos(o_q)$.

B.2 Single Series Formulation

To convert the Green's function of equation B.1 to a SS form, we write (separating m=0 term) [21],

$$G(x_i,y_i|x_j,y_j) = C\left\{\sum_{n=0}^{\infty}\sigma_n\frac{\cos(k_y y_i)\cos(k_y y_j)}{k_y^2-k^2} + \sum_{n=0}^{\infty}\sigma_n\cos(k_y y_i)\cos(k_y y_j)S(n)\right\}$$

where, $C = \frac{j\omega\mu h}{ab}$ and, $S(n) = 2\sum_{m=1}^{\infty}\frac{\cos(k_x x_i)\cos(k_x x_j)}{k_x^2+k_y^2-k^2}$

The summation S(n) may be carried out analytically using trigonometric Fourier series [29] as

$$S(n) = -\frac{a^2}{\pi^2\alpha_n^2} + \frac{a^2}{2\pi\alpha_n}\frac{\mathrm{ch}\alpha_n(\pi-x_1)+\mathrm{ch}\alpha_n(\pi-x_2)}{\mathrm{sh}(\alpha_n\pi)} \qquad \text{(B.4)}$$

where,

$$\alpha_n = \frac{a}{\pi}\sqrt{k_y^2 - k^2},$$
$$x_1 = \frac{\pi(x_> + x_<)}{a}, \quad \frac{\pi(x_> - x_<)}{a},$$
$$x_> = \max(x_i, x_j), \quad \text{and} \quad x_< = \max(x_i, x_j)$$

Using equation B.4 we can rewrite the Green's function as,

$$G(x_i, y_i | x_j, y_j) = -aC\sum_{n=0}^{\infty}\sigma_n \cos(k_y y_i)\cos(k_y y_j)\cdot\left\{\frac{\cos[\gamma_n(x_> - a)]\cos[\gamma_n x_<]}{\gamma_n \sin(\gamma_n a)}\right\} \quad \text{(B.5)}$$

where $\gamma_n = \pm\sqrt{k^2 - k_y^2}$ is complex. This form of the Green's function is introduced into equation B.2 to solve for Z_{pq}. Because $x_<$ and $x_>$ may be either x_i or x_j depending on the relative positions of x_i and x_j it is not possible to immediatly separate these variables and integrate across ports p and q separately. Instead, we consider several different cases. Recognizing that since $Z_{pq} = Z_{qp}$ we may swap the two ports if so desired; and this permits us to consider only three distinctly different situations. For the case shown in Figure B.4(a), there is no overlap of ports p and q in the x-direction, and consequently $x_> = x_j$ and $x_< = x_i$ for all x_i and x_j on their respective ports p and q. It is also possible to include in this case the situation when ports p and q share a common endpoint along x since $(x_>, x_<)$ may be defined as either (x_i, x_j) or (x_j, x_i) if $x_i = x_j$. In Figure B.4(b), port q is completely overlayed by port p. In this case, every position x_j on port q also lies somewhere along port p. One admissable parameterization of path p (traveling left to right) has the variable x_i starting at the left end of port p, moving up to the point x_j, and then continuing on to the right endpoint of port p. By dividing this path at the position x_j, the journey is cut in two. During the first part, $x_i < x_j$, but during the second leg of the journey $x_i > x_j$. This suggests a procedure for evaluating equation B.2 in this case. The same concept holds for the situation shown in Figure B.4(c), only in

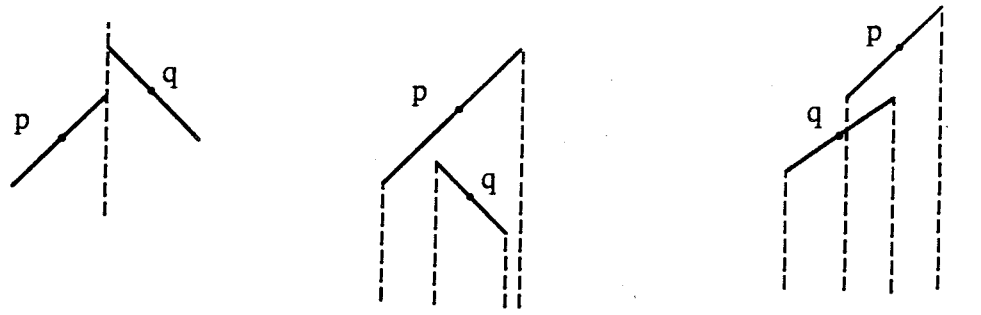

Figure B.4: Distinct Cases for Port Positions;

this case both paths p and q are divided into two ports. Now we consider each of these cases in turn.

B.2.1 No Overlap of Ports p and q Along the x-direction

Since $x_j \geq x_i$ it is possible from equations B.2 and B.5 to write,

$$\begin{aligned} Z_{pq} &= -aC\sum_{n=0}^{\infty}\left(\tfrac{\sigma_n}{\gamma_n \sin(\gamma_n a)}\right) \\ &\cdot \left[\tfrac{1}{w_p}\int_{w_p}\cos(\gamma_n x_i)\cos(k_y y_i)\,dr_p\right]\cdot\left[\tfrac{1}{w_q}\int_{w_q}\cos[\gamma_n(x_j-a)]\cos(k_y y_j)\,dr_q\right] \end{aligned}$$

From this, we obtain

$$\begin{aligned} Z_{pq} = \; & -aC\sum_{n=0}^{\infty}\left(\tfrac{\sigma_n}{\gamma_n \sin(\gamma_n a)}\right) \\ & \cdot \tfrac{1}{2}\left\{\cos[\gamma_n x_p + k_y y_p]\,\mathrm{sinc}[\gamma_n \tfrac{w_{px}}{2} + k_y \tfrac{w_{py}}{2}]\right. \\ & + \left.\cos[\gamma_n x_p - k_y y_p]\,\mathrm{sinc}[\gamma_n \tfrac{w_{px}}{2} - k_y \tfrac{w_{py}}{2}]\right] \\ & \cdot \tfrac{1}{2}\left\{\cos[\gamma_n x_q + k_y y_q]\,\mathrm{sinc}[\gamma_n \tfrac{w_{qx}}{2} + k_y \tfrac{w_{qy}}{2}]\right. \\ & + \left.\cos[\gamma_n x_q - k_y y_q]\,\mathrm{sinc}[\gamma_n \tfrac{w_{qx}}{2} - k_y \tfrac{w_{qy}}{2}]\right] \end{aligned} \tag{B.6}$$

For large values of n, $\Im m\{\gamma_n\}$ becomes large, and this creates numerical problems when evaluating equation B.6. Since each of the functions (sine, cosine, and sinc) in this expression grow exponentially, we cannot evaluate them individually for large n. It is their combination which converges, so it is necessary to re-write equation B.6 in a form which can be evaluated numerically for large arguments. To do so, we begin by selecting γ_n in equation B.5 such that $\Im m\{\gamma_n\} < 0$, and further constrain the angles o_p, $o_q \in [\frac{-\pi}{2}, \frac{\pi}{2}]$ such that w_{p_x} and w_{q_x} are positive. Under these conditions, we have $\gamma_n = \alpha - j\beta;\ \beta > 0$ and therefore these functions grow exponentially,

$$
\begin{array}{ll}
|\sin(\gamma_n a)| & \text{grows as } e^{\beta a} \\
|\cos[\gamma_n x_p \pm k_y y_p]| & \text{grows as } e^{\beta x_p} \\
|\cos[\gamma_n (x_q - a) \pm k_y y_q]| & \text{grows as } e^{\beta (a - x_q)} \\
|\sin[\gamma_n \frac{w_{p_x}}{2} \pm k_y \frac{w_{p_y}}{2}]| & \text{grows as } e^{\beta |\frac{w_{p_x}}{2}|} \\
|\sin[\gamma_n \frac{w_{q_x}}{2} \pm k_y \frac{w_{q_y}}{2}]| & \text{grows as } e^{\beta |\frac{w_{q_x}}{2}|}
\end{array}
$$

The result is that provided

$$a - |x_p| - |a - x_q| - |\frac{w_{p_x}}{2}| - |\frac{w_{q_x}}{2}| > 0$$

then

$$e^{-\beta[a - x_p - (a - x_q) - |\frac{w_{p_x}}{2}| - |\frac{w_{q_x}}{2}|]}$$

will decay and we can evaluate these five terms collectively without numerical problems. This corresponds to our original assumption that there is no overlap in x, and this is illustrated in Figure B.5 below. Thus to handle the numerical

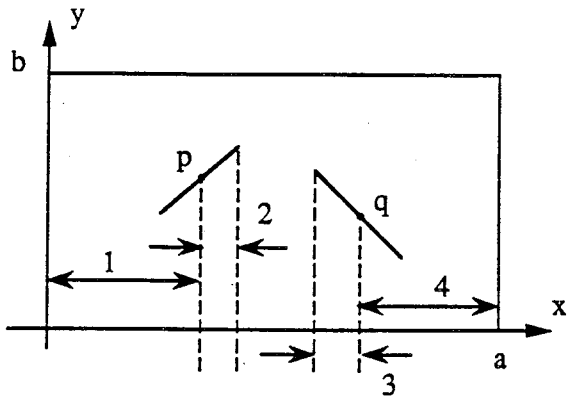

Figure B.5: Convergence Requirements for No Overlap Along the x-direction

problems encountered when evaluating equation B.6, we define the function,

$$f_1(\gamma,\, k,\, a,\, x_p,\, y_p,\, w_{p_x},\, w_{p_y},\, x_q,\, y_q,\, w_{q_x},\, w_{q_y})$$

$$= \frac{1}{\gamma \sin(\gamma a)} \cos[\gamma x_p + k y_p] \cos[\gamma(x_q - a) + k y_q] \operatorname{sinc}[\gamma w_{p_x} + k w_{p_y}] \operatorname{sinc}[\gamma w_{q_x} + k w_{q_y}]$$

and for suitably large values of n, we replace these functions with their large argument expansions, namely,

$$\sin(\gamma a) \approx \frac{1}{2j} e^{j(\gamma a)}$$

$$\cos[\gamma x_p + k y_p] \approx \frac{1}{2} e^{j(\gamma x_p + k y_p)}$$

$$\cos[\gamma(x_q - a) + k y_q] \approx \frac{1}{2} e^{-j[\gamma(x_q - a) + k y_q]}$$

$$\operatorname{sinc}[\gamma w_{p_x} + k w_{p_y}] \approx \frac{1}{2j(\gamma w_{p_x} + k w_{p_y})} e^{j[\gamma w_{p_x} + k w_{p_y}]}$$

$$\operatorname{sinc}[\gamma w_{q_x} + k w_{q_y}] \approx \frac{1}{2j(\gamma w_{q_x} + k w_{q_y})} e^{j[\gamma w_{q_x} + k w_{q_y}]}$$

From this expression for f_1, we may write

$$Z_{pq} = -aC \sum_{n=0}^{\infty} \sigma_n F_n$$

where,

$$\begin{aligned} F_n &= \{ f_1(\gamma_n, k_y, a, x_p, y_p, \tfrac{w_{p_x}}{2}, \tfrac{w_{p_y}}{2}, x_q, y_q, \tfrac{w_{q_x}}{2}, \tfrac{w_{q_y}}{2}) \\ &+ f_1(\gamma_n, k_y, a, x_p, y_p, \tfrac{w_{p_x}}{2}, \tfrac{w_{p_y}}{2}, x_q, -y_q, \tfrac{w_{q_x}}{2}, -\tfrac{w_{q_y}}{2}) \\ &+ f_1(\gamma_n, k_y, a, x_p, -y_p, \tfrac{w_{p_x}}{2}, -\tfrac{w_{p_y}}{2}, x_q, y_q, \tfrac{w_{q_x}}{2}, \tfrac{w_{q_y}}{2}) \\ &+ f_1(\gamma_n, k_y, a, x_p, -y_p, \tfrac{w_{p_x}}{2}, -\tfrac{w_{p_y}}{2}, x_q, -y_q, \tfrac{w_{q_x}}{2}, -\tfrac{w_{q_y}}{2})\} \end{aligned}$$

B.2.2 Complete Overlap Since x_i and x_j are not separable, we write

$$\begin{aligned} Z_{pq} &= -aC\sum_{n=0}^{\infty}\left(\tfrac{\sigma_n}{\gamma_n \sin(\gamma_n a)}\right) \\ &\cdot\left[\tfrac{1}{w_p w_q}\int_{w_q}\int_{w_p} \cos(k_y y_i)\,\cos(k_y y_j)\,\cos(\gamma_n x_<)\,\cos[\gamma_n(x_> - a)]\,dr_p\,dr_q\right] \end{aligned} \tag{B.7}$$

To evaluate the expression B.7 we integrate along port p first and then integrate the result along port q. To set up this approach, we write,

$$Z_{pq} = -aC\sum_{n=0}^{\infty}\left(\tfrac{\sigma_n}{\gamma_n \sin(\gamma_n a)}\right)\left\{\tfrac{1}{w_q}\int_{w_q} I(x_j, y_j)dr_q\right\}$$

where

$$I(x_j, y_j) = \tfrac{1}{w_p}\int_{w_p} \cos(k_y y_i)\,\cos(k_y y_j)\,\cos(\gamma_n x_<)\,\cos[\gamma_n(x_> - a)]\,dr_p$$

We next parameterize the path p according to

$$x_i(t) = x_p + w_{p_x} t \qquad -\tfrac{1}{2} \le t \le \tfrac{1}{2}$$

$$y_i(t) = y_p + w_{p_y} t \qquad -\tfrac{1}{2} \le t \le \tfrac{1}{2}$$

and, by insisting that $o_p \in [\frac{-\pi}{2}, \frac{\pi}{2}]$, w_{p_x} is guaranteed to be positive so $x_i(t)$ runs left to right. At some time, t_o, $x_i(t_o) = x_p + w_{p_x} t_o = x_j$, which serves as the crossover for $x_>$ and $x_<$. Thus

$$\begin{cases} x_i < x_j & \text{if } t \le t_o \\ x_i > x_j & \text{if } t \le t_o \end{cases}$$

$$\text{where} \quad t_o = \left(\frac{x_j - x_p}{w_{p_x}}\right)$$

So, we may write

$$I(x_j,y_j) = \cos(k_y y_j)\cdot\left\{\cos[\gamma_n(x_j-a)]\int_{-\frac{1}{2}}^{t_o}\cos[k_y(y_p+w_{p_y}t)]\,\cos[\gamma_n(x_p+w_{p_x}t)]\,dt + \cos[\gamma_n x_j]\int_{t_o}^{\frac{1}{2}}\cos[k_y(y_p+w_{p_y}t)]\,\cos[\gamma_n(x_p+w_{p_x}t-a)]\,dt\right\}$$

This can be solved to yield a three-term expression for $I(x_j,y_j)$, or

$$I(x_j,y_j) = I_1 + I_2 + I_3$$

Thus Z_{pq} also has three terms. We write,

$$Z_{pq} = -aC\sum_{n=0}^{\infty}\sigma_n F_n$$

$$\text{where} \quad F_n = f_1 + f_2 + f_3$$

Expressions for f_1, f_2, and f_3 are have been obtained by performing the necessary integrations to yield,

$$f_1 = \left(\frac{1}{\gamma_n\sin(\gamma_n a)}\right)\left\{\frac{\sin\{k_y[y_p+\frac{w_{p_y}}{2}]+\gamma_n[x_p+\frac{w_{p_x}}{2}-a]\}}{4(k_y\frac{w_{p_y}}{2}+\gamma_n\frac{w_{p_x}}{2})} + \frac{\sin\{k_y[y_p+\frac{w_{p_y}}{2}]-\gamma_n[x_p+\frac{w_{p_x}}{2}-a]\}}{4(k_y\frac{w_{p_y}}{2}-\gamma_n\frac{w_{p_x}}{2})}\right\}$$
$$\cdot\ \tfrac{1}{2}\left\{\cos[\gamma_n x_q + k_y y_q]\,\mathrm{sinc}[\gamma_n\tfrac{w_{q_x}}{2} + k_y\tfrac{w_{q_y}}{2}] + \cos[\gamma_n x_q - k_y y_q]\,\mathrm{sinc}[\gamma_n\tfrac{w_{q_x}}{2} - k_y\tfrac{w_{q_y}}{2}]\right\}$$

$$f_2 = \left(\frac{-1}{\gamma_n\sin(\gamma_n a)}\right)\left\{\frac{\sin\{k_y[y_p-\frac{w_{p_y}}{2}]+\gamma_n[x_p-\frac{w_{p_x}}{2}]\}}{4(k_y\frac{w_{p_y}}{2}+\gamma_n\frac{w_{p_x}}{2})} + \frac{\sin\{k_y[y_p-\frac{w_{p_y}}{2}]-\gamma_n[x_p-\frac{w_{p_x}}{2}]\}}{4(k_y\frac{w_{p_y}}{2}-\gamma_n\frac{w_{p_x}}{2})}\right\}$$
$$\cdot\ \tfrac{1}{2}\left\{\cos[\gamma_n(x_q-a)+k_y y_q]\,\mathrm{sinc}[\gamma_n\tfrac{w_{q_x}}{2} + k_y\tfrac{w_{q_y}}{2}]\right.$$
$$\left.+\ \cos[\gamma_n(x_q-a)-k_y y_q]\,\mathrm{sinc}[\gamma_n\tfrac{w_{q_x}}{2} - k_y\tfrac{w_{q_y}}{2}]\right\}$$

$$f_3 = \left(\frac{-\frac{1}{4}\frac{w_{p_x}}{2}}{(k_y\frac{w_{p_y}}{2})^2-(\gamma_n\frac{w_{p_x}}{2})^2}\right)\Big[\cos\{k_y[\mathrm{mp}(x_q-x_p)+y_p+y_q]\}\,\mathrm{sinc}[k_y(\mathrm{mp}\tfrac{w_{q_x}}{2}+\tfrac{w_{q_y}}{2})]$$
$$+\ \cos\{k_y[\mathrm{mp}(x_q-x_p)+y_p-y_q]\}\,\mathrm{sinc}[k_y(\mathrm{mp}\tfrac{w_{q_x}}{2}-\tfrac{w_{q_y}}{2})]\Big]$$

$$\text{where} \quad \mathrm{mp} = \left(\tfrac{w_{p_y}}{2}/\tfrac{w_{p_x}}{2}\right)$$

Evaluating f_3 numerically does not cause difficulties, and the various terms of f_1 and f_2 may be computed making use of the function,

$$\begin{aligned} & f_{z_1}(\gamma,\, k,\, a,\, A,\, B,\, C,\, D,\, E,\, F) \\ & = \tfrac{1}{\gamma \sin(\gamma a)} \sin[\gamma A + kB]\, \cos[\gamma C + kD]\, \mathrm{sinc}[\gamma E + kF] \end{aligned} \tag{B.8}$$

where f_{z_1} is evaluated using large argument expansions when n is suitable large. Z_{pq} has been shown to converge, provided the conditions for this case are properly satisfied.

B.2.3 Incomplete Overlap Here again, we write

$$Z_{pq} = -aC \sum_{n=0}^{\infty} \left(\tfrac{\sigma_n}{\gamma_n \sin(\gamma_n a)} \right) \left\{ \tfrac{1}{w_q} \int_{w_q} I(x_j, y_j) dr_q \right\}$$

Consider the regions identified in Figure B.6. For x_j in region I, $x_j \leq x_i$ for all x_i on port p. Thus in this region we have,

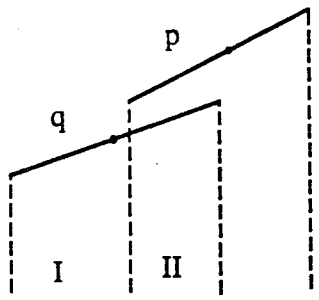

Figure B.6: Port Configuration for Incomplete Overlap

$$I_I(x_j, y_j) = \frac{1}{w_p} \int_{w_p} \cos(k_y y_i) \cos(k_y y_j) \cos(\gamma_n x_j) \cos[\gamma_n (x_i - a)]\, dr_p$$

If x_j is in region II, however, the position of x_j lies somewhere along the width of path p, so for x_j in this region we must parameterize path p as we did for the previous case, or

$$I_{II}(x_j,y_j) = \cos(k_y y_j)\cdot\left\{\cos[\gamma_n(x_j-a)]\int_{-\frac{1}{2}}^{t_o}\cos[k_y(y_p+w_{p_y}t)]\,\cos[\gamma_n(x_p+w_{p_x}t)]\,dt \right.$$
$$\left. +\cos[\gamma_n x_j]\int_{t_o}^{\frac{1}{2}}\cos[k_y(y_p+w_{p_y}t)]\,\cos[\gamma_n(x_p+w_{p_x}t-a)]\,dt\right\}$$

where $t_o = \left(\frac{x_j-x_p}{w_{p_x}}\right)$ as before. So, we have, $I(x_j,y_j) = I_I + I_{II}$. Since we have split the integration along port q into two portions, in this case we write

$$\frac{1}{w_q}\int_{w_q} I(x_j,y_j) = \int_{-\frac{1}{2}}^{t_{oq}} I_I[x_j(t),y_j(t)]\,dt \;+\; \int_{-\frac{1}{2}}^{t_{oq}} I_{II}[x_j(t),y_j(t)]\,dt$$

where $t_{o_q} = \left(\frac{x_p-\frac{w_{p_x}}{2}-x_q}{w_{q_x}}\right)$

By carrying out the necessary integrations, we obtain four terms; three terms correspond to I_{II} as before, and an additional term comes from I_I. Thus we write,

$$Z_{pq} = -aC\sum_{n=0}^{\infty}\sigma_n F_n$$

$$\text{where}\quad F_n = f_1+f_2+f_3+f_4$$

Expressions for these functions have been obtained and are given here.

$$f_1 = \left(\frac{1}{\gamma_n\sin(\gamma_n a)}\right)\left\{\frac{\sin\{k_y[y_q+\mathrm{mq}(x_p-\frac{w_{p_x}}{2}-x_q)]+\gamma_n[x_p-\frac{w_{p_x}}{2}]\}}{4(k_y\frac{w_{q_y}}{2}+\gamma_n\frac{w_{q_x}}{2})}\right.$$
$$+\;\frac{\sin\{k_y[y_q+\mathrm{mq}(x_p-\frac{w_{p_x}}{2}-x_q)]-\gamma_n[x_p-\frac{w_{p_x}}{2}]\}}{4(k_y\frac{w_{q_y}}{2}-\gamma_n\frac{w_{q_x}}{2})} - \frac{\sin\{k_y[y_q-\frac{w_{q_y}}{2}]+\gamma_n[x_q-\frac{w_{q_x}}{2}]\}}{4(k_y\frac{w_{q_y}}{2}+\gamma_n\frac{w_{q_x}}{2})}$$
$$\left. -\;\frac{\sin\{k_y[y_q-\frac{w_{q_y}}{2}]-\gamma_n[x_q-\frac{w_{q_x}}{2}]\}}{4(k_y\frac{w_{q_y}}{2}-\gamma_n\frac{w_{q_x}}{2})}\right\}\cdot\frac{1}{2}\left\{\cos[\gamma_n(x_p-a)+k_y y_p]\,\mathrm{sinc}[\gamma_n\frac{w_{p_x}}{2}+k_y\frac{w_{p_y}}{2}]\right.$$
$$\left.+\;\cos[\gamma_n(x_p-a)-k_y y_p]\,\mathrm{sinc}[\gamma_n\frac{w_{p_x}}{2}-k_y\frac{w_{p_y}}{2}]\right\}$$

$$\text{where}\quad \mathrm{mq} = \left(\frac{w_{q_y}}{2}/\frac{w_{q_x}}{2}\right)$$

$$f_2 = \left(\frac{1}{\gamma_n \sin(\gamma_n a)}\right)\left\{\frac{\sin\{k_y[y_p+\frac{w_{py}}{2}]+\gamma_n[x_p-a+\frac{w_{px}}{2}]\}}{4(k_y\frac{w_{py}}{2}+\gamma_n\frac{w_{px}}{2})}\right.$$
$$\left. + \frac{\sin\{k_y[y_p+\frac{w_{py}}{2}]-\gamma_n[x_p-a+\frac{w_{px}}{2}]\}}{4(k_y\frac{w_{py}}{2}-\gamma_n\frac{w_{px}}{2})}\right\}\cdot\left[-\frac{\sin\{k_y[y_q+\mathrm{mq}(x_p-\frac{w_{px}}{2}-x_q)]+\gamma_n[x_p-\frac{w_{px}}{2}]\}}{4(k_y\frac{w_{qy}}{2}+\gamma_n\frac{w_{qx}}{2})}\right.$$
$$- \frac{\sin\{k_y[y_q+\mathrm{mq}(x_p-\frac{w_{px}}{2}-x_q)]-\gamma_n[x_p-\frac{w_{px}}{2}]\}}{4(k_y\frac{w_{qy}}{2}-\gamma_n\frac{w_{qx}}{2})} + \frac{\sin\{k_y[y_q+\frac{w_{qy}}{2}]+\gamma_n[x_q+\frac{w_{qx}}{2}]\}}{4(k_y\frac{w_{qy}}{2}+\gamma_n\frac{w_{qx}}{2})}$$
$$\left. + \frac{\sin\{k_y[y_q+\frac{w_{qy}}{2}]-\gamma_n[x_q+\frac{w_{qx}}{2}]\}}{4(k_y\frac{w_{qy}}{2}-\gamma_n\frac{w_{qx}}{2})}\right]$$

$$f_3 = \left(\frac{1}{\gamma_n \sin(\gamma_n a)}\right)\left\{\frac{\sin\{k_y[y_p-\frac{w_{py}}{2}]+\gamma_n[x_p-\frac{w_{px}}{2}]\}}{4(k_y\frac{w_{py}}{2}+\gamma_n\frac{w_{px}}{2})}\right.$$
$$\left. + \frac{\sin\{k_y[y_p-\frac{w_{py}}{2}]-\gamma_n[x_p-\frac{w_{px}}{2}]\}}{4(k_y\frac{w_{py}}{2}-\gamma_n\frac{w_{px}}{2})}\right\}\cdot\left[\frac{\sin\{k_y[y_q+\mathrm{mq}(x_p-\frac{w_{px}}{2}-x_q)]+\gamma_n[x_p-\frac{w_{px}}{2}-a]\}}{4(k_y\frac{w_{qy}}{2}+\gamma_n\frac{w_{qx}}{2})}\right.$$
$$+ \frac{\sin\{k_y[y_q+\mathrm{mq}(x_p-\frac{w_{px}}{2}-x_q)]-\gamma_n[x_p-\frac{w_{px}}{2}-a]\}}{4(k_y\frac{w_{qy}}{2}-\gamma_n\frac{w_{qx}}{2})} - \frac{\sin\{k_y[y_q+\frac{w_{qy}}{2}]+\gamma_n[x_q+\frac{w_{qx}}{2}-a]\}}{4(k_y\frac{w_{qy}}{2}+\gamma_n\frac{w_{qx}}{2})}$$
$$\left. - \frac{\sin\{k_y[y_q+\frac{w_{qy}}{2}]-\gamma_n[x_q+\frac{w_{qx}}{2}-a]\}}{4(k_y\frac{w_{qy}}{2}-\gamma_n\frac{w_{qx}}{2})}\right]$$

Evaluating function f_4 requires us to consider two different situations. If mp $\neq \pm$ mq, then

$$f_4 = \left[\frac{-\frac{1}{8}\frac{w_{px}}{2}}{(k_y\frac{w_{py}}{2})^2-(\gamma_n\frac{w_{px}}{2})^2}\right]$$
$$\cdot\left\{\left(\frac{\{[y_q+\frac{w_{qy}}{2}]+[y_p+\mathrm{mp}(x_q-x_p+\frac{w_{qx}}{2})]\}}{[\frac{w_{qy}}{2}+\mathrm{mp}\frac{w_{qx}}{2}]}\right)\mathrm{sinc}\{k_y[y_q+\frac{w_{qy}}{2}+y_p+mp(x_q-x_p+\frac{w_{qx}}{2})]\}\right.$$
$$+\left(\frac{\{[y_q+\frac{w_{qy}}{2}]-[y_p+\mathrm{mp}(x_q-x_p+\frac{w_{qx}}{2})]\}}{[\frac{w_{qy}}{2}-\mathrm{mp}\frac{w_{qx}}{2}]}\right)\mathrm{sinc}\{k_y[y_q+\frac{w_{qy}}{2}-y_p-\mathrm{mp}(x_q-x_p+\frac{w_{qx}}{2})]\}$$
$$-\left(\frac{\{[y_q+\mathrm{mq}(x_p-x_q-\frac{w_{px}}{2}]+[y_p-\frac{w_{py}}{2}]\}}{[\frac{w_{qy}}{2}+\mathrm{mp}\frac{w_{qx}}{2}]}\right)\mathrm{sinc}\{k_y[y_q+\mathrm{mq}(x_p-x_q-\frac{w_{px}}{2})+y_p-\frac{w_{py}}{2})]\}$$
$$\left.-\left(\frac{\{[y_q+\mathrm{mq}(x_p-x_q-\frac{w_{px}}{2}]-[y_p-\frac{w_{py}}{2}]\}}{[\frac{w_{qy}}{2}-\mathrm{mp}\frac{w_{qx}}{2}]}\right)\mathrm{sinc}\{k_y[y_q+\mathrm{mq}(x_p-x_q-\frac{w_{px}}{2})-y_p+\frac{w_{py}}{2})]\}\right\}$$

On the other hand, if mp = $\pm$ mq, then

$$
\begin{aligned}
f_4 \;=\; & \left[\frac{-\frac{1}{8}\frac{w_{px}}{2}}{(k_y\frac{w_{py}}{2})^2-(\gamma_n\frac{w_{px}}{2})^2}\right] \\
& \cdot \left\{\left(1-\frac{x_p-x_q-\frac{w_{px}}{2}}{\frac{w_{qx}}{2}}\right)\cos\{k_y[y_q \mp (\mathrm{mp}\,x_q-\mathrm{mp}\,x_p+y_p)]\}\right. \\
& + \left(\frac{2\frac{w_{qy}}{2}+y_q\pm(\mathrm{mp}\,x_q-\mathrm{mp}\,x_p+y_p)}{2\frac{w_{qy}}{2}}\right)\mathrm{sinc}\{k_y[2\tfrac{w_{qy}}{2}+y_q\pm(\mathrm{mp}\,x_q-\mathrm{mp}\,x_p+y_p)]\} \\
& + \left(\frac{2\mathrm{mq}(x_p-x_q-\frac{w_{px}}{2})+y_q\pm(\mathrm{mp}\,x_q-\mathrm{mp}\,x_p+y_p)}{2\frac{w_{qy}}{2}}\right) \\
& \left.\cdot\ \mathrm{sinc}\{k_y[2\mathrm{mq}\,(x_p-x_q-\tfrac{w_{px}}{2})+y_q\pm(\mathrm{mp}\,x_q-\mathrm{mp}\,x_p+y_p)]\}\right\}
\end{aligned}
$$

To evaluate f_1 for large n, we make use of function f_{z_1} given in equation B.8. Function f_4 does not cause numerical problems but the various terms of functions f_2 and f_3 must be evaluated using the function, where f_{z_2} is evaluated using large argument expansions when n is suitably large. Z_{pq} has again been shown to converge, provided the conditions for this case are properly satisfied.

Because the computations become increasingly involved for each of these cases, an heirarchy has been established to place each port configuration into on of the classifications shown in Figure B.7. An algorithm has been written to make this determination, and consequently any arbitrary port configuration may be handled by calling this single subroutine.

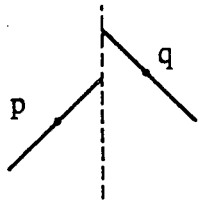

1) No Overlap in X

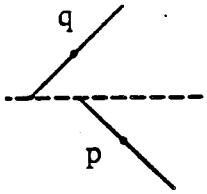

2) No Overlap in X

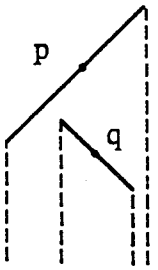

3) Complete Overlap in X

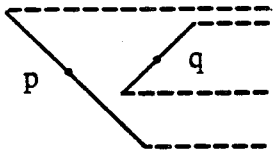

4) Complete Overlap in Y

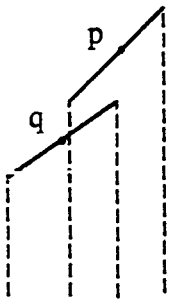

5) Incomplete Overlap in X

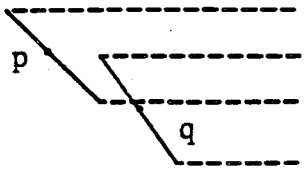

5) Incomplete Overlap in X

Figure B.7: Heirarchy for Port Classifications

APPENDIX C

EXPANSION OF POYNTING'S THEOREM APPLIED TO THE INTERACTION BETWEEN TWO MAGNETIC SOURCES

To obtain the time-average power radiated by an antenna into a lossless medium, the complex Poynting Theorem may be reduced to [24]

$$-\frac{1}{2}\int_V Re(\mathbf{J}_g^* \cdot \mathbf{E})\, dV = \frac{1}{2}\oint_S Re(\mathbf{E} \times \mathbf{H}^*) \cdot d\bar{s} \tag{C.1}$$

where the left hand side represents the power driving the antenna terminals and the right hand side is the time-average power flux leaving a closed surface, S, enclosing the antenna, or,

$$P_{rad} = \frac{1}{2}\oint_S Re(\mathbf{E} \times \mathbf{H}^*) \cdot d\bar{s} \tag{C.2}$$

Consider two magnetic current elements as shown in Figure (3.7). The source $\mathbf{M}_1$ gives rise to the fields $\mathbf{E}_1$ and $\mathbf{H}_1$, while $\mathbf{M}_2$ produces $\mathbf{E}_2$ and $\mathbf{H}_2$. Thus the total fields are given by $\mathbf{E} = \mathbf{E}_1 + \mathbf{E}_2$ and $\mathbf{H} = \mathbf{H}_1 + \mathbf{H}_2$. To evaluate equation C.2, we write,

$$\begin{aligned} (\mathbf{E} \times \mathbf{H}^*) &= (\mathbf{E}_1 + \mathbf{E}_2) \times (\mathbf{H}_1^* + \mathbf{H}_2^*) \\ &= \mathbf{E}_1 \times \mathbf{H}_1^* + \mathbf{E}_2 \times \mathbf{H}_2^* + \mathbf{E}_1 \times \mathbf{H}_2^* + \mathbf{E}_2 \times \mathbf{H}_1^* \end{aligned} \tag{C.3}$$

So we have,

$$\begin{aligned} &\tfrac{1}{2}\oint_S Re(\mathbf{E} \times \mathbf{H}^*) \cdot d\bar{s} = \tfrac{1}{2}\oint_S Re(\mathbf{E}_1 \times \mathbf{H}_1^*) \cdot d\bar{s} \\ &+\tfrac{1}{2}\oint_S Re(\mathbf{E}_2 \times \mathbf{H}_2^*) \cdot d\bar{s} + \tfrac{1}{2}\oint_S Re[\mathbf{E}_1 \times \mathbf{H}_2^* + \mathbf{E}_2 \times \mathbf{H}_1^*] \cdot d\bar{s} \end{aligned} \tag{C.4}$$

Now, the first two terms we recognize from equation C.2 as the power radiated by the sources $\mathbf{M}_1$ and $\mathbf{M}_2$, respectively, or

$$P_{rad_1} = \frac{1}{2}\oint_S Re(\mathbf{E}_1 \times \mathbf{H}_1^*) \cdot d\bar{s} \tag{C.5}$$

$$P_{rad_2} = \frac{1}{2}\oint_S Re(\mathbf{E}_2 \times \mathbf{H}_2^*) \cdot d\bar{s} \tag{C.6}$$

Now, we make use of the divergence theorem to write the third integral on the right hand side of equation C.4 as

$$\tfrac{1}{2}\oint_S Re[\mathbf{E}_1 \times \mathbf{H}_2^* + \mathbf{E}_2 \times \mathbf{H}_1^*] \cdot d\bar{s} = \iiint_V \tfrac{1}{2} Re\{\nabla \cdot [\mathbf{E}_1 \times \mathbf{H}_2^* + \mathbf{E}_2 \times \mathbf{H}_1^*]\}\, dV \tag{C.7}$$

Next we expand the integrand as follows.

$$\nabla \cdot [\mathbf{E}_1 \times \mathbf{H}_2^* + \mathbf{E}_2 \times \mathbf{H}_1^*] = \nabla \cdot (\mathbf{E}_1 \times \mathbf{H}_2^*) + \nabla \cdot (\mathbf{E}_2 \times \mathbf{H}_1^*) \tag{C.8}$$

and

$$\begin{aligned} \nabla \cdot (\mathbf{E}_1 \times \mathbf{H}_2^*) &= \mathbf{H}_2^* \cdot (\nabla \times \mathbf{E}_1) - \mathbf{E}_1 \cdot (\nabla \times \mathbf{H}_2^*) \\ \nabla \cdot (\mathbf{E}_2 \times \mathbf{H}_1^*) &= \mathbf{H}_1^* \cdot (\nabla \times \mathbf{E}_2) - \mathbf{E}_2 \cdot (\nabla \times \mathbf{H}_1^*) \end{aligned} \tag{C.9}$$

where,

$$\begin{aligned} \nabla \cdot \mathbf{E}_1 &= -j\omega\mu\mathbf{H}_1 - \mathbf{M}_1 \\ \nabla \cdot \mathbf{H}_2^* &= (j\omega\epsilon\mathbf{E}_2)^* + \mathbf{J}_2 = -j\omega\epsilon\mathbf{E}_2^* \\ \nabla \cdot \mathbf{E}_2 &= -j\omega\mu\mathbf{H}_2 - \mathbf{M}_2 \\ \nabla \cdot \mathbf{H}_1^* &= (j\omega\epsilon\mathbf{E}_1)^* + \mathbf{J}_1 = -j\omega\epsilon\mathbf{E}_1^* \end{aligned} \tag{C.10}$$

So, we have

$$\begin{aligned} \nabla \cdot [\mathbf{E}_1 \times \mathbf{H}_2^* + \mathbf{E}_2 \times \mathbf{H}_1^*] &= \mathbf{H}_2^* \cdot [-j\omega\mu\mathbf{H}_1 - \mathbf{M}_1] - \mathbf{E}_1 \cdot [-j\omega\epsilon\mathbf{E}_2^*] \\ &+ \mathbf{H}_1^* \cdot [-j\omega\mu\mathbf{H}_2 - \mathbf{M}_2] - \mathbf{E}_2 \cdot [-j\omega\epsilon\mathbf{E}_1^*] \\ &= j\omega\{-\mu[\mathbf{H}_1 \cdot \mathbf{H}_2^* + \mathbf{H}_1^* \cdot \mathbf{H}_2] + \epsilon[\mathbf{E}_1 \cdot \mathbf{E}_2^* + \mathbf{E}_1^* \cdot \mathbf{E}_2]\} \\ &- [\mathbf{H}_2^* \cdot \mathbf{M}_1 + \mathbf{H}_1^* \cdot \mathbf{M}_2] \end{aligned} \tag{C.11}$$

Next, recognizing that (for z complex) since $z_1 z_2^* + z_1^* z_2$ is real, we have,

$$\frac{1}{2} Re\{\nabla \cdot [\mathbf{E}_1 \times \mathbf{H}_2^* + \mathbf{E}_2 \times \mathbf{H}_1^*]\} = \frac{1}{2} Re[\mathbf{H}_2^* \cdot \mathbf{M}_1 + \mathbf{H}_1^* \cdot \mathbf{M}_2] \qquad \text{(C.12)}$$

Thus equation C.7 becomes

$$\begin{aligned} &\iiint_V \tfrac{1}{2}\ Re\{\nabla \cdot [\mathbf{E}_1 \times \mathbf{H}_2^* + \mathbf{E}_2 \times \mathbf{H}_1^*]\}\, dV \\ &\quad = -\tfrac{1}{2} Re\left\{ \iiint_V \mathbf{H}_2^* \cdot \mathbf{M}_1\, dV + \iiint_V \mathbf{H}_1^* \cdot \mathbf{M}_2\, dV \right\} \end{aligned} \qquad \text{(C.13)}$$

and, since the integrand of the first integral is zero whenever $\mathbf{M}_1 = 0$,

$$\iiint_V \mathbf{H}_2^* \cdot \mathbf{M}_1\, dV = \iiint_{V_1} \mathbf{H}_2^* \cdot \mathbf{M}_1\, dV \qquad \text{(C.14)}$$

where V_1 is any surface enclosing $\mathbf{M}_1$. Similarly

$$\iiint_V \mathbf{H}_1^* \cdot \mathbf{M}_2\, dV = \iiint_{V_2} \mathbf{H}_1^* \cdot \mathbf{M}_2\, dV \qquad \text{(C.15)}$$

Now, letting V_1 and V_2 shrink down in size to converge to the surface of the elemental sources $\mathbf{M}_1$ and $\mathbf{M}_2$, we take the field quantities $\mathbf{H}_1^*$ and $\mathbf{H}_2^*$ to be constant over these tiny volumes and thus

$$\iiint_{V_1} \mathbf{H}_2^* \cdot \mathbf{M}_1\, dV = \mathbf{H}_2^* \cdot \mathbf{M}_1\, dl_1 \qquad \text{(C.16)}$$

and,

$$\iiint_{V_2} \mathbf{H}_1^* \cdot \mathbf{M}_2\, dV = \mathbf{H}_1^* \cdot \mathbf{M}_2\, dl_2 \qquad \text{(C.17)}$$

From which we write,

$$\frac{1}{2} \oint_S Re(\mathbf{E} \times \mathbf{H}^*) \cdot d\bar{s} = P_{rad_1} + P_{rad_2} - \frac{1}{2} Re[\mathbf{H}_2^* \cdot \mathbf{M}_1] - \frac{1}{2} Re[\mathbf{H}_1^* \cdot \mathbf{M}_2] \qquad \text{(C.18)}$$

APPENDIX D

DIFFERENTIATION OF EXPRESSION FOR Y_{IJ}

For a collection of sources it is not possible to always have one of the sources located at the origin as in Figure 3.5, so the differentiation of Y_{ij} will be carried out for the geometry of Figure D.1. To begin, the complete expressions for Y_{ij} are needed, and these follow in equations D.1 - D.11

$$Y_{ij} = dl_j J_j \tag{D.1}$$

$$J_j = -H_x \sin(\alpha_j) + H_y \cos(\alpha_j) \tag{D.2}$$

$$H_x = H_\theta \cos(\theta_{ij}) + H_r \sin(\theta_{ij}) \tag{D.3}$$

$$H_y = -H_\theta \sin(\theta_{ij}) + H_r \cos(\theta_{ij}) \tag{D.4}$$

$$H_r = \left(\frac{dl_i}{\pi\eta}\right) \cos(\theta) F_r(r) \tag{D.5}$$

$$H_\theta = \left(\frac{dl_i}{2\pi\eta}\right) \sin(\theta) F_\theta(r) \tag{D.6}$$

$$F_r(r) = \left[\frac{e^{-jk_o r}}{r^2}\left(1 + \frac{1}{jk_o r}\right)\right] \tag{D.7}$$

$$F_\theta(r) = \left[\frac{jk_o e^{-jk_o r}}{r}\left(1 + \frac{1}{jk_o r} - \frac{1}{(k_o r)^2}\right)\right] \tag{D.8}$$

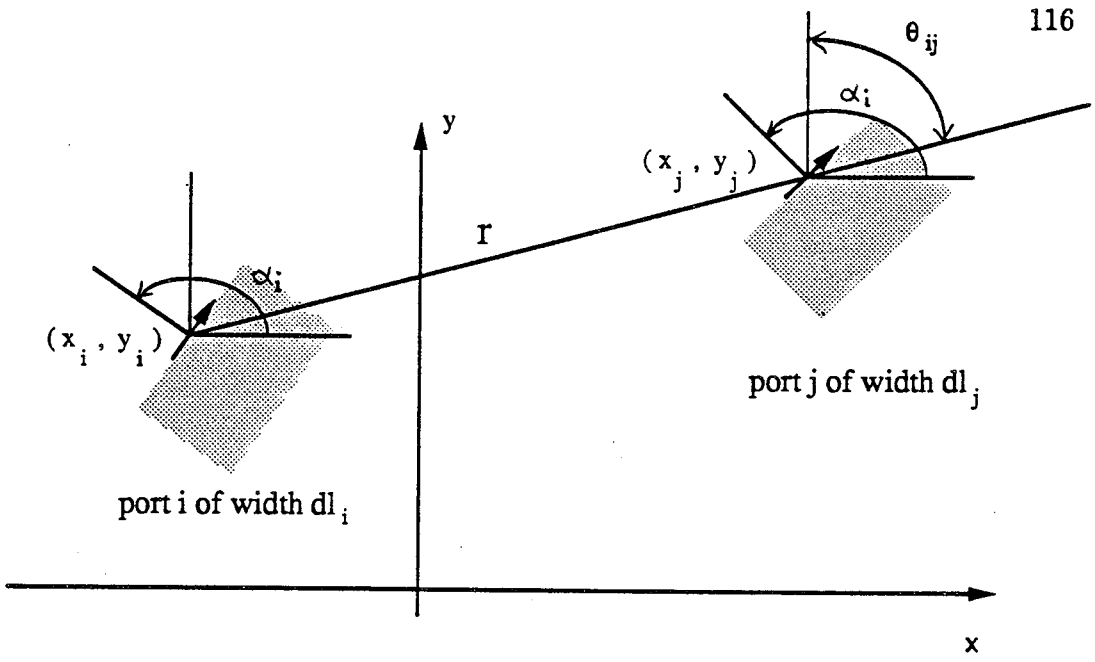

Figure D.1: Geometry of Two Arbitrarily Placed Magnetic Current Elements

$$\theta = \theta_{ij} + \alpha_i - \pi \tag{D.9}$$

$$\theta_{ij} = \tan^{-}1\left(\frac{x_j - x_i}{y_j - y_i}\right) \tag{D.10}$$

$$r = \sqrt{(x_i - x_j)^2 + (y_i - y_j)^2} \tag{D.11}$$

Obtaining the partial derivatives of Y_{ij} will be done one step at a time begining with equation D.11 and moving backward up to equation D.1. By carrying out the calculations this way, it will be straightforward to make use of the intermediate results. Since α_j does not appear in equations D.3 - D.11, $\partial/\partial\alpha$ will not appear until we get to equation D.2.

For equation D.11,

$$\begin{aligned} \frac{\partial r}{\partial x_j} &= \tfrac{1}{2}[(x_i - x_j)^2 + (y_i - y_j)]^{-\frac{1}{2}} \cdot 2(x_i - x_j)(-1) = \tfrac{x_j - x_i}{r} = \sin(\theta_{ij}) \\ \frac{\partial r}{\partial y_j} &= \tfrac{1}{2}[(x_i - x_j)^2 + (y_i - y_j)]^{-\frac{1}{2}} \cdot 2(y_i - y_j)(-1) = \tfrac{y_j - y_i}{r} = \cos(\theta_{ij}) \end{aligned} \tag{D.12}$$

For equation D.10,

$$\begin{aligned}
\theta_{ij} &= \tan^{-1}(u); \qquad u = \tfrac{x_j - x_i}{y_j - y_i} \\
\tfrac{\partial \theta_{ij}}{\partial x_j} &= \tfrac{\partial \theta_{ij}}{\partial u} \cdot \tfrac{\partial u}{\partial x_j} = \tfrac{1}{1+\left(\frac{x_j-x_i}{y_j-y_i}\right)^2} \cdot \tfrac{y_j-y_i}{(y_j-y_i)^2} = \tfrac{y_j-y_i}{r^2} = \tfrac{\cos(\theta_{ij})}{r} \\
\tfrac{\partial \theta_{ij}}{\partial y_j} &= \tfrac{\partial \theta_{ij}}{\partial u} \cdot \tfrac{\partial u}{\partial y_j} = \tfrac{1}{1+\left(\frac{x_j-x_i}{y_j-y_i}\right)^2} \cdot -\tfrac{x_j-x_i}{(y_j-y_i)^2} = -\tfrac{\sin(\theta_{ij})}{r}
\end{aligned} \tag{D.13}$$

For equation D.9,

$$\begin{aligned}
\tfrac{\partial \theta}{\partial x_j} &= \tfrac{\partial \theta}{\partial \theta_{ij}} \cdot \tfrac{\partial \theta_{ij}}{\partial x_j} = \tfrac{\cos(\theta_{ij})}{r} \\
\tfrac{\partial \theta}{\partial y_j} &= \tfrac{\partial \theta}{\partial \theta_{ij}} \cdot \tfrac{\partial \theta_{ij}}{\partial y_j} = -\tfrac{\sin(\theta_{ij})}{r}
\end{aligned} \tag{D.14}$$

For equation D.8,

$$\begin{aligned}
\tfrac{\partial F_\theta(r)}{\partial x_j} &= \tfrac{\partial F_\theta(r)}{\partial r} \cdot \tfrac{\partial r}{\partial x_j} = \left\{\left(\tfrac{jk_o e^{-jk_o r}}{r}\right)\left(-\tfrac{1}{jk_o r^2} + \tfrac{2}{k_o{}^2 r^3}\right)\right. \\
&+ \left.\left(1 + \tfrac{1}{jk_o r} - \tfrac{1}{(k_o r)^2}\right)\left[\tfrac{r(jk_o)(-jk_o)\,e^{-jk_o r} - jk_o\, e^{-jk_o r}}{r^2}\right]\right\} \sin(\theta_{ij}) \\
&= \left(\tfrac{k_o{}^2\, e^{-jk_o r}}{r}\right)\left(1 - \tfrac{2j}{k_o r} - \tfrac{3}{(k_o r)^2} + \tfrac{3j}{(k_o r)^3}\right)\sin(\theta_{ij})
\end{aligned} \tag{D.15}$$

$$\tfrac{\partial F_\theta(r)}{\partial y_j} = \tfrac{\partial F_\theta(r)}{\partial r} \cdot \tfrac{\partial r}{\partial y_j} = \left(\tfrac{k_o{}^2\, e^{-jk_o r}}{r}\right)\left(1 - \tfrac{2j}{k_o r} - \tfrac{3}{(k_o r)^2} + \tfrac{3j}{(k_o r)^3}\right)\cos(\theta_{ij})$$

For equation D.7,

$$\begin{aligned}
\tfrac{\partial F_r(r)}{\partial x_j} &= \tfrac{\partial F_r(r)}{\partial r} \cdot \tfrac{\partial r}{\partial x_j} = \left\{\left(\tfrac{e^{-jk_o r}}{r^2}\right)\left(-\tfrac{1}{jk_o r^2}\right)\right. \\
&+ \left.\left(1 + \tfrac{1}{jk_o r}\right)\left[\tfrac{r^2(-jk_o)\,e^{-jk_o r} - 2re^{-jk_o r}}{r^4}\right]\right\} \sin(\theta_{ij}) \\
&= \left(\tfrac{-jk_o\, e^{-jk_o r}}{r^2}\right)\left(1 + \tfrac{3}{jk_o r} - \tfrac{3}{(k_o r)^2}\right)\sin(\theta_{ij})
\end{aligned} \tag{D.16}$$

$$\tfrac{\partial F_r(r)}{\partial y_j} = \tfrac{\partial F_r(r)}{\partial r} \cdot \tfrac{\partial r}{\partial y_j} = \left(\tfrac{-jk_o\, e^{-jk_o r}}{r^2}\right)\left(1 + \tfrac{3}{jk_o r} - \tfrac{3}{(k_o r)^2}\right)\cos(\theta_{ij})$$

From this point on, the expressions will be left in terms of those already obtained, thus for equation D.6,

$$\begin{aligned}
\tfrac{\partial H_\theta}{\partial x_j} &= \left(\tfrac{dl_i}{2\pi\eta}\right)\left\{\sin(\theta)\tfrac{\partial F_\theta(r)}{\partial x_j} + F_\theta(r)\,\cos(\theta)\cdot\tfrac{\cos(\theta_{ij})}{r}\right\} \\
\tfrac{\partial H_\theta}{\partial y_j} &= \left(\tfrac{dl_i}{2\pi\eta}\right)\left\{\sin(\theta)\tfrac{\partial F_\theta(r)}{\partial y_j} - F_\theta(r)\,\cos(\theta)\cdot\tfrac{\sin(\theta_{ij})}{r}\right\}
\end{aligned} \tag{D.17}$$

For equation D.5,

$$\begin{aligned}\frac{\partial H_r}{\partial x_j} &= \left(\frac{dl_i}{\pi\eta}\right)\left\{\cos(\theta)\frac{\partial F_r(r)}{\partial x_j} - F_r(r)\,\sin(\theta)\cdot\frac{\cos(\theta_{ij})}{r}\right\}\\ \frac{\partial H_r}{\partial y_j} &= \left(\frac{dl_i}{\pi\eta}\right)\left\{\cos(\theta)\frac{\partial F_r(r)}{\partial y_j} + F_r(r)\,\sin(\theta)\cdot\frac{\sin(\theta_{ij})}{r}\right\}\end{aligned} \tag{D.18}$$

For equation D.4,

$$\begin{aligned}\frac{\partial H_y}{\partial x_j} &= \left\{-H_\theta\frac{\partial\sin(\theta_{ij})}{\partial x_j} - \sin(\theta_{ij})\,\frac{\partial H_\theta}{\partial x_j} + H_r\,\frac{\partial\cos(\theta_{ij})}{\partial x_j} + \cos(\theta_{ij})\,\frac{\partial H_r}{\partial x_j}\right\}\\ \frac{\partial H_y}{\partial y_j} &= \left\{-H_\theta\frac{\partial\sin(\theta_{ij})}{\partial y_j} - \sin(\theta_{ij})\,\frac{\partial H_\theta}{\partial y_j} + H_r\,\frac{\partial\cos(\theta_{ij})}{\partial y_j} + \cos(\theta_{ij})\,\frac{\partial H_r}{\partial y_j}\right\}\end{aligned} \tag{D.19}$$

For equation D.3,

$$\begin{aligned}\frac{\partial H_x}{\partial x_j} &= \left\{H_\theta\frac{\partial\cos(\theta_{ij})}{\partial x_j} + \cos(\theta_{ij})\,\frac{\partial H_\theta}{\partial x_j} + H_r\,\frac{\partial\sin(\theta_{ij})}{\partial x_j} + \sin(\theta_{ij})\,\frac{\partial H_r}{\partial x_j}\right\}\\ \frac{\partial H_x}{\partial y_j} &= \left\{H_\theta\frac{\partial\cos(\theta_{ij})}{\partial y_j} + \cos(\theta_{ij})\,\frac{\partial H_\theta}{\partial y_j} + H_r\,\frac{\partial\sin(\theta_{ij})}{\partial y_j} + \sin(\theta_{ij})\,\frac{\partial H_r}{\partial y_j}\right\}\end{aligned} \tag{D.20}$$

For equation D.2,

$$\begin{aligned}\frac{\partial J_j}{\partial x_j} &= \left\{-\sin(\alpha_j)\,\frac{\partial H_x}{\partial x_j} + \cos(\alpha_j)\,\frac{\partial H_y}{\partial x_j}\right\}\\ \frac{\partial J_j}{\partial y_j} &= \left\{-\sin(\alpha_j)\,\frac{\partial H_x}{\partial y_j} + \cos(\alpha_j)\,\frac{\partial H_y}{\partial y_j}\right\}\\ \frac{\partial J_j}{\partial \alpha_j} &= \left\{-H_x\,\cos(\alpha_j) - H_y\,\sin(\alpha_j)\right\}\end{aligned} \tag{D.21}$$

Finally, for equation D.1 we obtain,

$$\begin{aligned}\frac{\partial Y_{ij}}{\partial x_j} &= dl_j\,\frac{\partial J_j}{\partial x_j}\\ \frac{\partial Y_{ij}}{\partial y_j} &= dl_j\,\frac{\partial J_j}{\partial y_j}\\ \frac{\partial Y_{ij}}{\partial \alpha_j} &= dl_j\,\frac{\partial J_j}{\partial \alpha_j}\end{aligned} \tag{D.22}$$